INFORMATION EXTRACTION FROM MESSY DATA, NOISY SPECTRA, INCOMPLETE DATA, AND UNLABELED IMAGES

A Dissertation
Presented to
The Academic Faculty

By

Hongzhen Tian

In Partial Fulfillment
of the Requirements for the Degree
Doctor of Philosophy in the
Georgia Institute of Technology
The H. Milton Stewart School of Industrial & and Systems Engineering

Georgia Institute of Technology

August 2021

INFORMATION EXTRACTION FROM MESSY DATA, NOISY SPECTRA, INCOMPLETE DATA, AND UNLABELED IMAGES

Thesis committee:

Dr. Chuck Zhang, Advisor
The H. Milton Stewart School of Industrial & and Systems Engineering
Georgia Institute of Technology

Dr. Ben Wang
The H. Milton Stewart School of Industrial & and Systems Engineering
Georgia Institute of Technology

Dr. Yajun Mei, Co-advisor
The H. Milton Stewart School of Industrial & and Systems Engineering
Georgia Institute of Technology

Dr. Yan Wang
The George W. Woodruff School of Mechanical Engineering
Georgia Institute of Technology

Dr. Jianjun(Jan) Shi
The H. Milton Stewart School of Industrial & and Systems Engineering
Georgia Institute of Technology

Date approved: May 20, 2021

Whatever happens, happens for the best.

A saying

For my beloved parents, husband Sheng

ACKNOWLEDGMENTS

I was born and grew up in a small village in the countryside, and I'm the fourth girl in a financially stretched farming family. My mother has no chance to receive any school education, but she deeply believes that knowledge alters one's fate. Although she is influenced by patriarchal thought somehow, she never looks down upon me. On the opposite, she supports gender equality and always encourages me to prove girl power, and motivates me to chase my dream, both emotionally and materially. Fortunately, I inherited her bravery and self-confidence, aggressiveness and optimism.

I always took first place, being the shiniest star in school until the end of high school. In the college entrance examination, I got the highest score among candidates from 19 high schools in the county, which is sensational and makes me and my families relatively reputable in the community. Following the unexpected honor, I received a very generous scholarship, about $\$15,000$, from my high school. I really appreciate that amazing scholarship, which broke the shackles and gave wings to my dreams. Since then, economic independence liberated my imagination. Though the distribution of education resources is heavily uneven, the college entrance examination gives us, the vulnerable groups, a life-changing chance. This is one of the fairest things I met and change my life for the first time.

In 2013, I was admitted to the Energy and Power Engineering school in Xi'an Jiaotong University. Studying and living with outstanding peers from all over the country, I realized that I'm nobody but a "small town exam expert". I don't have any well-trained artistic expertise, nor a broad vision from the family education. But fortunately, I met a lot of brilliant people here who lead and encourage me along the way. My friends, like Jiayue Fan in UCSD, Bingyu Wang in TAMU, Xin Shen in Yale, Yu Li in Princeton, Jiandong Wu in PKU, Yuwen Yang in SJTU, and Xiangkun Cao in Cornell, and many other extraordinary friends, helped me recognized my dream, and we rushed to our dream step by step,

helping each other and encouraging each other. In my Junior year, Dr. Erjiang Hu became my advisor. He gave me meticulous and enlightening instructions on doing research, which inspired my love for scientific research and helped me publish my first paper. These experiences together lead me to the decision of pursuing a Ph.D. degree abroad.

In 2017, Dr. Chuck Zhang gave me the chance to join his group at Georgia Tech. Admission to my dream school and dream Ph.D. program is the second life-changing opportunity for me. At Georgia Tech, I got the chance to take courses from the professors that can be seen on classic textbooks, collaborate with the top researchers all over the world, get supervised by the worship professors on yearning topics. During my graduate years at Georgia Tech, I deeply understand what is called "peer pressure" and realize the power of a platform. Also, Dr. Zhang always makes the group a big family, which gives us a sense of belonging and engagement.

Dr. Yajun Mei rebuilds me from a very struggling status. The beginning of my Ph.D. years was a challenging hard mode for me as it came with the overwhelming course and research requirements, as well as a new and lonely living mode. For a long time, I live in anxiety, depression, and self-denial, lost confidence, courage, and motivation. Like a ray of sunshine shining into my Ph.D. life, Dr. Mei keeps on affirming my academic ability and giving me detailed practical instructions, both academically, behaviorally, and mentally. Like a knowledgeable father, he taught me how to think and talk properly, introduced me to some promising projects and excellent collaborators like Dr. Zev, encouraged me to do life plans like obtaining a driver's license and running married family life. Gradually, I was recharged with confidence and cheerfulness, and figure out a clear study and career path.

I would like to thank the members of my thesis committee for their help in the preparation of this work – Dr. Jianjun Shi, who helped to shed new light on many of my ideas, and guides me by his academic achievements and lofty character. Dr. Ben Wang, who always puts up with great questions, provides golden advice and set high standards for us. And Dr. Yan Wang, who drives me to think about the extension of a methodology to broader

application fields.

Special thanks are due to the friends and colleagues who made this work possible. Andi Wang and Jialei Chen were invaluable both as friends and as sounding boards for some of my more outlandish ideas. Dr. Zev Cohen Reuven, introduced by Dr. Mei, was also a major influence, and I'm glad we were able to help each other with our special expertise. With his organization and the help from my husband, our statistical model becomes a mobile App available in Apple Store. Besides, he helps me a lot in my job hunting by providing solid recommendations during the reference check.

Also, I would like to thanks Shancong Mou, Zhaonan Liu, Xuzhou Jiang, Jianfeng Shi, Daniel Cantrell, Jarod Weber, Michael McCracken, Chin-yuan Tseng, Zhen Zhong, Chen Jiang, Chen Feng, Dan Tu, Wan Qin, and Ray Liu, for the smooth collaborations, good companies, and deep friendship.

Also, I would like to show my deep gratitude to the Chinese Scholarship Council (CSC) for the CSC-GT joint scholarship, which covers my living expenses for all 4 years along my pursuing the Ph.D. degree. Besides, I also appreciate the George Fellowship which recognizes my efforts in research in the health systems and analytics area. These financial aids not only covered my living expenses but also improved the living quality of my parents who are far away in the countryside.

In the end, I would like to thank my husband, Sheng Zhang, for the selfless love and endless support to me. We met in Georgia Tech, fell in love, and got married here. Without his company, I cannot imagine how would I survive some terrible moments. He has been teaching me a lot of professional knowledge, giving me a sense of safety and hope. He is the witness of my Ph.D. life and he's going to be the witness of the rest of my life, as we promised to each other at our wedding.

TABLE OF CONTENTS

LIST OF TABLES

LIST OF FIGURES

SUMMARY

Data collected from real-world scenarios are never ideal but often messy because data errors are inevitable and may occur in creative and unexpected ways. And there are always some unexpected tricky troubles between ideal theory and real-world applications. Although with the development of data science, more and more elegant algorithms have been well developed and validated by rigorous proof, data scientists still have to spend 50% to 80% of their work time on cleaning and organizing data, leaving little time for actual data analysis. This dissertation research involves three scenarios of statistical modeling with common data issues: quantifying function effect on noisy functional data, multistage decision-making model over incomplete data, and unsupervised image segmentation over imperfect engineering images. And three methodologies are proposed accordingly to solve them efficiently.

In Chapter 2, a general two-step procedure is proposed to quantify the effects of a certain treatment on the spectral signals subjecting to multiple uncertainties for an engineering application which involves materials treatment for aircraft maintenance. With this procedure, two types of uncertainties in the spectral signals, offset shift and multiplicative error, are carefully addressed. In the two-step procedure, a novel optimization problem is formulated to estimate the representative template spectrum first, and then another optimization problem is formulated to obtain the pattern of modification $\mathbf{g}$ that reveals how the treatment affects the shape of the spectral signal, as well as a vector $\boldsymbol{\delta}$ that describes the degree of change caused by different treatment magnitudes. The effectiveness of the proposed method is validated in a simulation study. Furtherly, in a real case study, the proposed method is used to investigate the effect of plasma exposure on the FTIR spectra. As a result, the proposed method effectively identifies the pattern of modification under uncertainties in the manufacturing environment, which matches the knowledge of the affected chemical components by the plasma treatment. And the recovered magnitude of

modification provides guidance in selecting the control parameter of the plasma treatment.

In Chapter 3, an active learning-based multistage sequential decision-making model is proposed to assist doctors and patients to make cost-effective treatment recommendations when some clinical data are more expensive or time-consuming to collect than other laboratory data. The main idea is to formulate the incomplete clinical data into a multistage decision-making model where the doctors can make diagnostics decisions sequentially in these stages, and actively collect only the necessary examination data from certain patients rather than all. There are two novelties in estimating parameters in the proposed model. First, unlike the existed ordinal logistic regression model which only models a single stage, a multistage model is built by maximizing the joint likelihood function for all samples in all stages. Second, considering that the data in different stages are nested in a cumulative way, it is assumed that the coefficients for common features in different stages are invariant. Compared with the baseline approach that models each stage individually and independently, the proposed multistage model with common coefficients assumption has significant advantages. It reduces the number of variables to estimate significantly, improves the computational efficiency, and makes the doctors feel intuitive by assuming that newly added features will not affect the weights of existed ones. In a simulation study, the relative efficiency of the proposed method with regards to the baseline approach is 162% to 1,938%, proving its efficiency and effectiveness soundly. Then, in a real case study, the proposed method estimates all parameters very efficiently and reasonably.

In Chapter 4, a simple yet very effective unsupervised image segmentation method, called RG-filter, is proposed to segment engineering images with no significant contrast between foreground and background for a material testing application. With the challenge of limited data size, imperfect data quality, unreachable binary true label, we developed the RG-filter which thresholding the pixels according to the relative magnitude of the R channel and G channel of the RGB image. To test the performance of the existed image segmentation and proposed algorithm on our CFRP image data, we conducted a series

of experiments over an example specimen. Comparing all the pixel labeling results, the proposed RG-filter outperforms the others to be the most recommended one. in addition, it is super intuitive and efficient in computation. The proposed RG-filter can help to analyze the failure mode distribution and proportion on the surface of composite material after destructive DCB testing. The result can help engineers better understand the weak link during the bonding of composite materials, which may provide guidance on how to improve the joining of structures during aircraft maintenance. Also, it can be crucial data when modeling together with some downstream data as a whole. And if we can predict it from other variables, the destructive DCB testing can be avoided, a lot of time and money can be saved.

In Chapter 5, we concluded the dissertation and summarized the original contributions. In addition, future research topics associated with the dissertation have also been discussed.

In summary, the dissertation contributes to the area of *System Informatics and Control* (SIAC) to develop systematic methodologies based on messy real-world data in the field of composite materials and healthcare. The fundamental methodologies developed in this thesis have the potential to be applied to other advanced manufacturing systems.

CHAPTER 1
INTRODUCTION

1.1 Motivation

With the development of data science, more and more beautiful algorithms have been well established and validated by rigorous proof. However, there are always some unexpected tricky troubles between ideal theory and real-world application. This is because the data from real-world problems are not always ideal but often messy. Messy data—heterogeneous values, missing entries, and large errors—is a major obstacle to automated modeling. Data cleaning is the first step in any data processing pipeline, and the way it's carried out has serious consequences for the results of any subsequent analysis. Yet this step is generally performed using ad-hoc methods.

Fourier-transform infrared spectroscopy (FTIR) is a widely adopted technique for characterizing the chemical composition in many physical and chemical analyses. However, FTIR spectra are subject to multiple sources of uncertainty, and thus the analysis of them relies on domain experts and only can lead to qualitative conclusions. However, the demand of quantifying the effects of a univariate factor, such as plasma surface treatment, on spectral measurements subjecting to such multiplicative and offset uncertainties arises. With a systematic way of understanding the functional effect on noisy functional data, people can select optimal surface treatment parameters such as plasma distance, gain an understanding of the effect of plasma exposure on the CFRP material, and identify several chemical bonds that are affected by plasma exposure.

Incomplete data are commonly seen in real-world scenarios since data with certain information comes with a price. This is especially true in the healthcare area, where the doctors aim at making diagnoses as accurate as possible and determines the treatment recom-

mendation based on limited examinations. To address the issues caused by incomplete data in clinical modeling, there are many widely used methods developed according to missing patterns, such as simple deletion on feature or record, mean/median/mode/zeros substitution, regression imputation, last observation carried forward, expectation-maximization (EM), etc. [1, 2, 3]. These methods were developed from two basic ideas roughly. One is deleting the records or features with missing values, which will lead to a waste of available data and some modeling problems caused by limited data size. And the other one is "guessing" or "learning" the missing data from the observed data, which of course, is kind of dangerous for clinical modeling since the synthetic data brings extra uncertainties surely.

The engineering images collected from composite materials usually have limited data size, imperfect data quality, unreachable true labels. This makes it challenging to identify the failure modes distribution and proportion over the surface of a large piece of the composite material. The failure mode analysis is critical in the surface characterization of composite materials in aircraft joining and maintenance. After figuring out the distribution and proportion of failure modes, people can better understand the weak link during the bonding of composite material, which may give some clue on how to improve the joining and maintenance of aircraft. More importantly, the segmentation results can be crucial data when modeling together with some downstream data as a whole. Once we can predict the failure mode proportion and distribution directly from some surface characterizing variables, the expensive, time-consuming, and destructive DCB testing can be avoided, and naturally, a huge amount of time and money will be saved.

1.2 Research Objectives

The objective of this proposal is to develop basic, composable modeling tools for robust data inference by exploiting structure in the data set, developing models that accept data with noisy, uncertain, or missing values, and will produce clean and complete data sets. The research involves developing novel algorithms for denoising and tolerancing incomplete

and imperfect data by exploiting spatiotemporal, network, and low dimensional structures.

These methods of preprocessing data will allow researchers to draw power from the data that they do have and to perform any kind of analysis they normally would perform on ideal data. Applications range from social science surveys to medical informatics, from manufacturing analytics to marketing, from finance to hyperspectral imaging, and beyond.

1. develop a general procedure to (i) characterizes the underlying uncertainties of the FTIR spectra, and (ii) describes the nonlinear effect of plasma exposure on the post-exposure FTIR spectra.

2. develop a sequential decision-making model to help doctors making reliable diagnostic decisions and treatment recommendations with enough confidence in a cost-effective and convenient way. This model allows the doctor to actively collect only the necessary data in a sequential way rather than collecting all the data at the beginning.

3. develop an unsupervised image segmentation algorithm for the image data obtained from CFRP specimen after DCB testing and obtain the failure mode distribution and proportion.

1.3 State-of-the-art

As a spectrum, FTIR signal subjects to multiple types of uncertainty, such as sample-generated noise, instrument-generated noise, computationally generated noise, and some externally generated noise [4]. To decrease the level of uncertainty in FTIR measurements, many preprocessing techniques were developed [5, 6, 7, 8]. Cornel et al. [5] reviewed multiple FTIR signal correction techniques before analyzing FTIR signals. However, most of them are ad-hoc methods that do not fully characterize the sources of uncertainty and error patterns involved in the FTIR spectra. For example, in the standard normal variate (SNV)

transformation, people normalize the observed spectrum via its individual mean and individual standard deviation. This makes the SNV sensitive to noisy entries in the spectrum. Also, by centering and scaling the individual spectrum, it will eliminate some quantitative information, such as the magnitude difference on FTIR caused by plasma exposure. The multiplicative scatter correction (MSC) method corrects FTIR signals by regressing the observed spectra over the reference spectrum, usually, the sample means, and solve it via ordinary least square. However, defining an appropriate reference spectrum is the main challenge of MSC [9]. Also, the MSC model fails to consider the magnitude-dependent noise on the FTIR spectra. Based on the MSC, the extended multiplicative scatter correction (EMSC) [10] was developed. It involves higher-order terms of reference spectrum, the pure spectrum of individual chemical components, and the interference effects to reduce or eliminate the pathlength variation [9, 11]. However, the EMSC cannot be wildly used due to the lack of pure spectra of chemical matter, especially for very occasional users. In order to quantify the function treatment effect on FTIR spectra, the challenge is that surface treatments usually have nonlinear effects on the FTIR signals. Although there exist some quantitative analysis with regard to FTIR, such as simple multiple linear regression, neural networks [12], principal component analysis (PCA) [13], principal component regression (PCR) and partial least-squares regression (PLSR) [5], they are mainly developed for predicting other response variables through high-dimensional FTIR spectra. Quite the opposite, we aim to study the functional effect of a certain univariate factor on FTIR. However, due to the nonlinearity, the univariate factor effect on the high-dimensional measurements cannot be characterized through existing methods such as the functional linear models [14].

For most of the popular machine learning models, more features often contain more crucial information, lead to larger variable selection space, higher modeling accuracy, and more stable performance. However, in real-world scenarios, some informative features could be expensive and hard to obtain. This is especially the case in clinical trials. Every clinical data point comes with a price, such as clinical procedures, staff and admin, site

monitoring, site retention, and lab costs. Especially, some clinical examinations could be invasive and painful, or request staying still for a long time, or comes with some side effects like radiation. Therefore, those unwanted examinations are expected to be taken only when necessary, especially for pediatric patients. However, some patients are willing to take these expensive and informative examinations for more accurate diagnoses. These precious data, though observed in a small subset of the patients' population, induce the researchers to take them into consideration. Therefore, a commonly seen challenge of investigating the clinical case is incomplete data. In other words, not all patients have all features observed, but the researchers aim to use the observed data to the maximum without any waste. To address the issues caused by incomplete data in statistical modeling, there are many widely used methods developed according to missing patterns, such as simple deletion on feature or record, mean/median/mode/zeros substitution, regression imputation, last observation carried forward, EM, etc. [1]. These methods were developed from two basic ideas roughly. One is deleting the records or features with missing values, which will lead to a waste of available data and some modeling problems caused by limited data size. And the other one is "guessing" or "learning" the missing data from the observed data, which of course, is kind of dangerous for clinical modeling since the synthetic data brings extra uncertainties surely.

Image segmentation is the process of partitioning a digital image into different regions (sets of pixels, also known as superpixels) based on the characteristics of pixels. The goal of segmentation is to simplify and/or change the representation of an image into something that is more meaningful, easier, and efficient to analyze. Image segmentation is typically used to locate or identify objects and boundaries (lines, curves, etc.) in images. More precisely, image segmentation is the process of assigning a label to every pixel in an image such that pixels with the same label share certain characteristics [15]. Segmentation impacts a number of domains, from the filmmaking industry to the field of medicine [16]. For example, image segmentation can be used to crop out the foreground and place it into

certain backgrounds, track objects in a sequence of images, and identify the injured muscle and measure the bone or tissue in the medical field. The algorithms for image segmentation implementation have been well-developed these years. Three typical methodologies are developed for image segmentation: image segmentation by thresholding, pixel-wise clustering, and deep learning. Experiments show that the image segmentation result highly depends on the data structure, and people should choose the proper algorithm according to the data set case by case. For our CFRP image data, the problem associated with these segmentation methods is the number of label types. Usually, the existing methods segment the image into a lot of different regions with different labels in the mask. In implementations, often the cases, the number of segmentation is equaled to the type or level of labels with a one-to-one unordered relationship. Roughly speaking, the more the regions segmented, the finer the boundary identification. However, in our cases, we expect fine boundaries yet two types of labels only, pink adhesive film, or black CFRP substrate.

1.4 Organization of the Dissertation

This dissertation is organized in a multiple-chapter format. Each of Chapters 2, 3, and 4 are written as a research paper or technical report, some of which have been accepted or submitted for journal publications.

In Chapter 2, a general two-step procedure is proposed to quantify the effects of a certain treatment on the spectral signals subjecting to multiple uncertainties. With this procedure, two types of uncertainties in the spectral signals, offset shift and multiplicative error, are carefully addressed. In the two-step procedure, a novel optimization problem is formulated to estimate the representative template spectrum first, and then another optimization problem is formulated to obtain the pattern of modification g that reveals how the treatment affects the shape of the spectral signal, as well as a vector $\boldsymbol{\delta}$ that describes the degree of change caused by different treatment magnitudes. The effectiveness of the proposed method is validated in a simulation study. Furtherly, in a real case study, the

proposed method is used to investigate the effect of plasma exposure on the FTIR spectra. As a result, the proposed method effectively identifies the pattern of modification under uncertainties in the manufacturing environment, which matches the knowledge of the affected chemical components by the plasma treatment. And the recovered magnitude of modification provides guidance in selecting the control parameter of the plasma treatment.

In Chapter 3, a multistage sequential decision-making model is proposed to help the doctor make predictions and give treatment recommendations. The main idea is to formulate the incomplete clinical data into a multistage decision-making model where the doctors can make diagnostics decisions sequentially in these stages, and actively collect only the necessary examination data from certain patients rather than all. There are two novelties in estimating parameters in the proposed model. Firstly, unlike the existing ordinal logistic regression model which only models a single stage, we write the joint likelihood function for all stages and maximize it for the global optimum. Secondly, considering that the data in different stages are nested in a cumulative way, it is assumed that the coefficients for common features in different stages are invariant. For both simulation study and real case study, the proposed method is proved to effectively estimate the coefficients and cutoff points for all stages in the multistage model. It estimates all parameters simultaneously to reach the global optimum and fully considers the cumulative characteristics between these stages by making common coefficients assumption.

In Chapter 4, a simple yet very effective unsupervised image segmentation method, called RG-filter, is proposed to segment engineering images with no significant contrast between foreground and background. With the challenge of limited data size, imperfect data quality, unreachable binary true label, we developed the RG-filter which thresholding the pixels according to the relative magnitude of the R channel and G channel of the RGB image. To test the performance of the existing image segmentation and proposed algorithm on our CFRP image data, we conducted a series of experiments over a specimen as an example. Comparing all the pixel labeling results, the proposed RG-filter outperforms the

others to be the most recommended one. What's more, it is super intuitive and efficient in computation. The proposed RG-filter can help to analyze the failure mode distribution and proportion on the surface of composite material after destructive testing.

In Chapter 5, we concluded the dissertation and summarized the original contributions. In addition, future research topics associated with the dissertation have also been discussed.

CHAPTER 2

TREATMENT EFFECT MODELING FOR FTIR SIGNALS SUBJECT TO MULTIPLE SOURCES OF UNCERTAINTIES

Fourier-transform infrared spectroscopy (FTIR) is a widely-adopted technique for characterizing the chemical composition in many physical and chemical analysis. However, FTIR spectra are subject to multiple sources of uncertainty, and thus the analysis of them relies on domain experts and only can lead to qualitative conclusions. This study aims to analyze the effect of a certain treatment on FTIR spectra subject to two commonly observed uncertainties, the offset shift and the multiplicative error. Due to these uncertainties, the pre-exposure FTIR spectra are modeled according to the physical understanding of the uncertainty – observed spectra can be viewed as translating and stretchering an underlying *template signal*, and the post-exposure FTIR spectra are modeled as the translated and stretchered template signal plus an extra functional *treatment effect*. To provide engineering interpretation, the treatment effect is modeled as the product of the pattern of modification and its corresponding magnitude. A two-step parameter estimation algorithm is developed to estimate the underlying template signal, the pattern of modification, and the magnitude of modification at various treatment strength. The effectiveness of the proposed method is validated in a simulation study. Furtherly, in a real case study, the proposed method is used to investigate the effect of plasma exposure on the FTIR spectra. As a result, the proposed method effectively identifies the pattern of modification under uncertainties in the manufacturing environment, which matches the knowledge of the affected chemical components by the plasma treatment. And the recovered magnitude of modification provides guidance in selecting the control parameter of the plasma treatment.

2.0.1 Note to Practitioners

FTIR spectrometer is often used to characterize the surface chemical composition of a material. Due to the large uncertainties associated with the nature of spectrometer and the measurement environment, the FTIR signals are usually examined visually by experienced engineers and technicians in industrial applications, which can be both time-consuming and inaccurate. To understand the effect of plasma exposure on the surface property of carbon fiber reinforced polymer material, the elimination of uncertainties associated with FTIR signals is investigated, and a systematic method is proposed to quantify the effect of surface treatments on FTIR signals. A two-step analytic procedure is proposed, which provides the information on how the plasma exposure distorts the FTIR signals, and how the plasma distance relates to the magnitude of the distortion. The methodology in this article can be used to analyze the treatment effect on a variety of spectroscopic measurements that are subject to uncertainties such as offset and scaling errors, which expands the applications of in-situ handheld spectrometer metrology in manufacturing industries.

2.1 Introduction

FTIR measurements provide a sensitive and non-destructive way of understanding the material's chemical composition. Like most structural spectroscopic techniques, it characterizes the chemical composition of the material by capturing the absorbance or reflectance of light in a range of frequencies [17, 18]. Specifically, the FTIR spectrometer irradiates a beam of infrared light that contains a range of spectral components on the sample, and measures the intensity of the absorbed light at every frequency. As each chemical bond in the material only absorbs the infrared radiation at its characteristic frequency, the absorbance intensity of each light component indicates the amount of corresponding chemical bond in the examined sample [18, 10, 17]. The signals measured by an FTIR spectrometer are called the FTIR spectra. It takes the form of a high dimensional vector, representing the

infrared absorption intensities at a range of frequencies.

In recent decades, the application of FTIR on the surface characterization of carbon fiber reinforced polymer (CFRP) composites becomes popular [18, 19, 20, 21, 22]. CFRP materials express significant attention in the aerospace industry for its improved properties such as lightweight and excellent strength. However, safety concerns on its bonding quality are essential due to its low surface free energy [19]. In order to improve CFRP bonding quality, surface modification methods have been developed to improve CFRP surface energy, including thermal treatment, wet chemical or electrochemical oxidation, plasma and laser treatment, gas-phase oxidation, coating treatment, etc [20, 23, 21].

Among these surface modification methods, plasma exposure is an effective, convenient, and non-destructive option that allows for greater control over the number of unwanted reaction pathways [24, 25, 26, 27, 22, 20]. One of the most important operating parameters that control the intensity of the plasma treatment is the gap between the plasma nozzle and the sample surface, known as the plasma distance. Previous research indicated that smaller plasma distance that causes more intense plasma exposure to the sample increases the wettability of the material by modifying the chemical composition and the physical structures of its surface layer [25, 27, 23], which in turn improves the bonding quality between CFRP panels in aerospace applications.

To have a deeper understanding of the mechanism of plasma treatment on the CFRP surface, it is worthwhile to investigate how the plasma distance affects the treatment result, i.e., the change of chemical composition of the CFRP sample. Because the chemical components of the CFRP sample are characterized by FTIR measurements, this study aims at proposing a methodology to model the statistical effect of plasma treatment at different distances on the FTIR signals, also referred to as treatment effect. Specifically, consider the experiment detailed in Figure 2.1, where the pre-exposure FTIR measurements and post-exposure FTIR measurements are taken on a number of CFRP coupons. The strength of treatment, described by the plasma distance, is set to prescribed values from 2mm to

22mm. With the FTIR measurements, it can be investigated that how the plasma distance affects the FTIR signals taken from the samples. The methodology proposed in this study also tackles a general objective of understanding the statistical effect of a certain factor on spectral signal observations.

Modeling the treatment effect from FTIR signals involves two major challenges. First, as a spectrum, FTIR signal subjects to multiple types of uncertainty, such as sample-generated noise, instrument-generated noise, computationally generated noise, and some externally generated noise [4]. Among them, the most widely mentioned noise sources include light scattering, optical path length variations, temperature variations, and readout noise [10, 17, 5, 28]. The uncertainty sources mentioned above result in offset shift and multiplicative error on FTIR measurements, and the latter also influences the magnitude of random noise on FTIR measurements.

To decrease the level of uncertainty in FTIR measurements, many preprocessing techniques were developed [5, 6, 7, 8]. Cornel et al. [5] reviewed multiple FTIR signal correction techniques before analyzing FTIR signals. However, most of them are ad-hoc methods that do not fully characterize the sources of uncertainty and error patterns involved in the FTIR spectra. For example, in the standard normal variate (SNV) transformation, people normalize the observed spectrum via its individual mean and individual standard deviation. This makes the SNV sensitive to noisy entries in the spectrum. Also, by centering and scaling the individual spectrum, it will eliminate some quantitative information, such as the magnitude difference on FTIR caused by plasma exposure. The multiplicative scatter correction (MSC) method corrects FTIR signals by regressing the observed spectra over the reference spectrum, usually the sample mean, and solve it via ordinary least square. However, defining an appropriate reference spectrum is a main challenge of MSC [9]. Also, the MSC model fails to consider the magnitude-dependent noise on the FTIR spectra. Based on the MSC, the extended multiplicative scatter correction (EMSC) [10] was developed. It involves higher-order terms of reference spectrum, the pure spectrum of individual chemi-

cal component, and the interference effects to reduce or eliminate the pathlength variation [9, 11]. However, the EMSC cannot be wildly used due to the lack of the pure spectrum of chemical matter, especially for very occasional users. Therefore, the objective of this study is to develop a simple yet effective spectra correction method specifically for FTIR and corresponding quantitative analysis later.

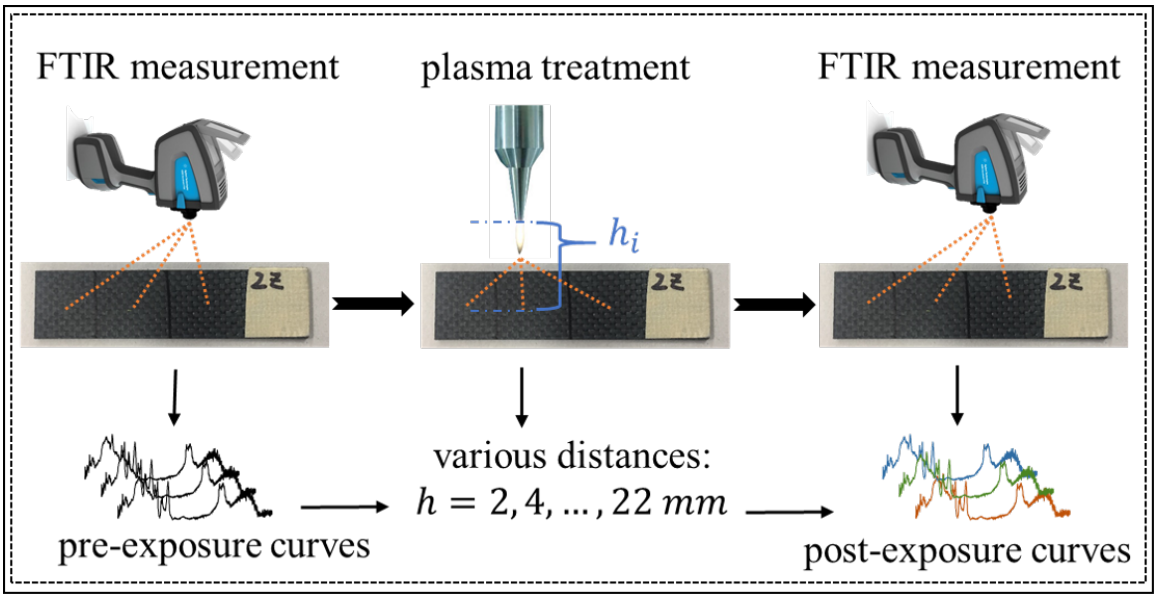

Figure 2.1: The experimental setup. The CFRP coupons were processed by plasma, and the plasma distance is set at $h_1, ..., h_n$. The FTIR measurements were taken before and after the plasma exposure to capture the change of chemical components on the CFRP surface.

The second challenge is that surface treatments usually have nonlinear effects on the FTIR signals. For example, the effect of the plasma exposure is nonlinear in general [26], as when plasma distance is small the effect of adjusting plasma distance for one unit is very significant, whereas when plasma distance is long, changing the plasma distance for one unit will barely affect the FTIR signal. Existing studies reported that FTIR signals can be affected in different forms, e.g., change of peak height, peak wideness, peak shape, joining or separation of peaks [5, 18]. Although there exist some quantitative analysis with regard to FTIR, such as simple multiple linear regression, neural networks [12, 29], principal component analysis (PCA) [13], principal component regression (PCR) and partial least-

squares regression (PLSR) [5], they are mainly developed for predicting other response variables through high-dimensional FTIR spectra. Quite the opposite, we aim to study the functional effect of a certain univariate factor on FTIR. However, due to the nonlinearity, the univariate factor effect on the high-dimensional measurements cannot be characterized through existing methods such as the functional linear models [14].

To tackle these challenges and achieve our objectives, a statistical procedure is developed in this study that (i) characterizes the underlying uncertainties of the FTIR spectra, and (ii) describes the nonlinear effect of plasma exposure on the post-exposure FTIR spectra. Based on the proposed model, a two-step parameter estimation procedure is developed. In the proposed procedure, an optimization problem is formulated to estimate the template FTIR signal that is representative for all measurement spectra first, and then another optimization problem is formulated to represent the effect of plasma exposure. To validate our methodology, experiments are conducted to collect FTIR measurements from CFRP samples before and after plasma exposure, as shown in Figure 2.1. And the measurements are plotted in Figure 2.2.

The contribution of our work is twofold. In terms of statistical analysis, a preprocessing algorithm is proposed to derive a template spectrum from FTIR spectra obtained from repetitive measurements, and a general strategy is developed to quantify the nonlinear treatment effect on spectral measurements. The methodology is applicable to a large variety of studies that involve investigating the effects of a univariate factor on spectral measurements subjecting to similar multiplicative and offset uncertainties. In terms of manufacturing engineering, a strategy is developed to select optimal surface treatment parameters such as plasma distance, gain an understanding of the effect of plasma exposure on the CFRP material, and identify several chemical bonds that are affected by plasma exposure.

In Section 2.2, the data characteristics are examined carefully and the statistical analysis is presented in detail. Our models are then proposed accordingly. In Section 2.3, the performance of the proposed two-step methodology on synthetic data is reported. In sec-

tion 2.4, the analytical result of a real case study is demonstrated. Finally, the article is concluded with further discussion in Section 2.5.

2.2 Uncertainty Analysis and Proposed Solution

In this section, the sources and patterns of variations on the signal data collected from the FTIR metrology are analyzed first, and then a statistical model that describes the uncertainties of these signals is proposed. Based on the statistical model, two optimization problems are formulated to estimate the template signal and capture the effect of the surface treatment on the spectral signals.

2.2.1 Uncertainties in FTIR Metrology and Spectra Modeling

Recall that the measurements of the FTIR spectrum are subject to multiple uncertainties. Among these uncertainties, the offset shift and multiplicative error are dominant. As shown in Figure 2.2 (a), signals obtained from the pre-exposure CFRP surfaces are similar in shapes, as if generated by vertically stretching and moving a template signal randomly. In this article, the variation of the vertical scale is referred to as "multiplicative error", and the variation of the vertical location is referred to as "offset shift". According to the literature [10, 17, 5], the offset shift is mainly caused by light scattering and the multiplicative error is mainly caused by optical path length variations related to the handheld nature of the device.

Besides, it can be seen that the uncertainty is magnitude dependent since the variance of the signal is more significant at the peaks of the signal, as shown in Figure 2.3. This phenomenon is common in light-based spectroscopy. For example, Yue et.al [4] summarized multiple error sources in greater detail for Ramen spectra, a similar metrology in material analysis.

With such observations, it is natural to assume that all the pre-exposure signals come

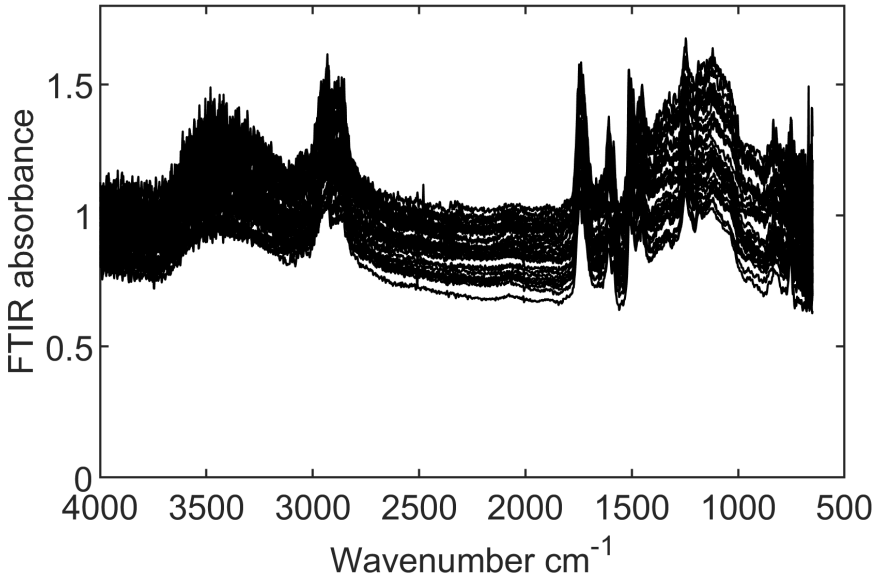

(a) Pre-exposure FTIR signals

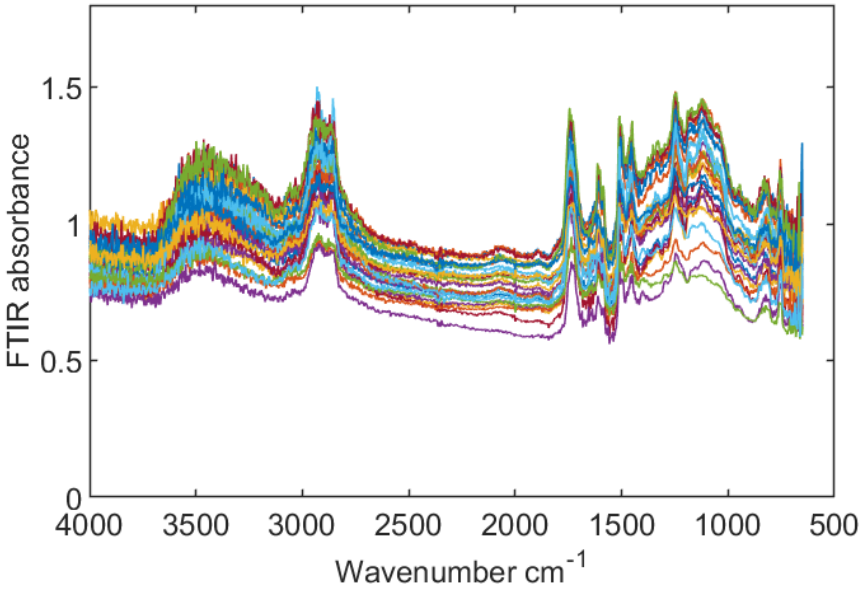

(b) Post-exposure FTIR signals

Figure 2.2: Raw FTIR signals collected collected from the CFRP coupons in the our experiments (Figure 2.1) before plasma exposure (a) and after plasma exposure at various distances (b).

from a common template signal. Then, the pre-treatment signal is modeled as

$$\mathbf{x}_{0,i} = a_{0,i}\left(\mathbf{x}_0 + \boldsymbol{\varepsilon}_{0,i}\right) + b_{0,i}\mathbf{1},\ i = 1, \ldots, n \tag{2.1}$$

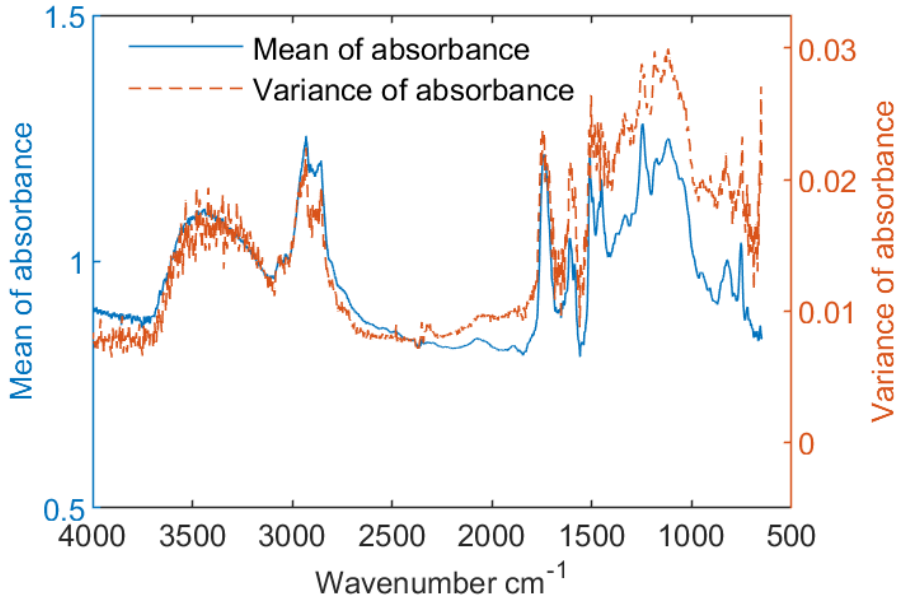

[ht]

Figure 2.3: The sample variance (the dashed line) and the sample mean (the solid line) of the FTIR signals obtained from the experiment in Figure 2.1.

where $\mathbf{x}_{0,i} = \left(x_{0,i}^{(1)}, \ldots, x_{0,i}^{(p)}\right)^\top \in \mathbb{R}^p$ denotes the i-th pre-exposure signal, $\mathbf{x}_0 \in \mathbb{R}^p$ denotes the common template signal, $a_{0,i} \in \mathbb{R}$ is the factor for the multiplicative error, $b_{0,i} \in \mathbb{R}$ is the factor for the offset, and $\boldsymbol{\varepsilon}_{0,i} \in \mathbb{R}^p$ is the noise vector whose elements are independent and follow a normal distribution $\varepsilon_{0,i}^{(j)} \sim N\left(0, \sigma^2\right),\ i = 1, \ldots, n;\ j = 1, \ldots, p$, and $\mathbf{1} = (1, \ldots, 1)^\top \in \mathbb{R}^p$.

Note that in the formulation (Equation 2.1), the parameters are not identifiable without further constraints, since the tuple $(a_{0,i},\ \mathbf{x}_0,\ b_{0,i})$ and $(ka_{0,i},\ (\mathbf{x}_0 - \mu\mathbf{1})/k,\ b_{0,i} + a_{0,i}\mu)$ correspond to the same probability model for $\mathbf{x}_{0,i}$ for any k and μ. To make the model identifiable, two additional constraints are applied to $\mathbf{x}_0$:

$$\|\mathbf{x}_0\|^2 = \mathbf{x}_0^\top \mathbf{x}_0 = 1, \quad \mathbf{x}_0^\top \mathbf{1} = 0 \tag{2.2}$$

In this formulation, it is assumed that the FTIR spectral measurements are statistically independent with each other. This is because the area that the FTIR equipment samples is very small, about 200 μm^2 at wavenumber 1700 cm^{-1}, according to the operation manu of

our 4300 Handheld FTIR from Agilent. Therefore, the handheld FTIR equipment cannot collect pre-exposure and post-exposure measurements at exactly the same location on the sample. Also, note that the random error $\boldsymbol{\varepsilon}_{0,i}$ is first added to the template signal $\mathbf{x}_0$, and then affected by the multiplicative error factor $a_{0,i}$. Therefore, the standard deviation of the noise from the signal is proportional to the multiplicative error, and thus every entry of the observed pre-exposure signals follows a normal distribution with different variance $x_{0,i}^{(j)} \sim N\left(a_{0,i}x_0^{(j)} + b_{0,i}, a_{0,i}^2\sigma^2\right)$. This observation corroborates with the property of FTIR signals discussed earlier.

The proposed model is different from the model proposed by Yue et al. [4] where $x_{0,i}^{(j)} \sim N\left(x_0^{(j)}, ax_0^{(j)} + b\right)$, because the multiplicative error and offset error are not considered in Yue's model. As will be seen later, estimating $\mathbf{x}_0$ in our model is different from simply denoising the raw signals analytically. Also, our representation of the signals is different from the MSC approach [10, 5], which implicitly assumes that all signals have the same error magnitudes in calculating the sample mean as the template signal.

The FTIR measurements obtained after the treatment procedure, such as plasma exposure, are also subject to offset shift and multiplicative error, etc. Moreover, the treatment effect leads to the shape change from the template signal. For all samples obtained with different strengths of the treatments, it is assumed that the plasma treatment results in the same pattern of change on the signals, and the plasma distance only affects the overall magnitude of changes in an FTIR signal. In the current example, the magnitude of change is larger when the plasma nozzle is closer to the CFRP coupon. From the above reasoning, the post-exposure template is modeled as $\mathbf{x}_0 + \delta_i\mathbf{g}$, where $\mathbf{g} \in \mathbb{R}^p$ represents the pattern of modification: the shape change of the template caused by plasma exposure. The value δ_i represents the magnitude of modification on the i-th spectrum, and $\boldsymbol{\delta} = (\delta_1, \ldots, \delta_n)^\top$ is referred to as the vector of effects. Therefore, the following model is introduced for the

post-exposure signal:

$$\mathbf{x}_{1,i} = a_{1,i}\left(\mathbf{x}_0 + \delta_i \mathbf{g} + \boldsymbol{\varepsilon}_{1,i}\right) + b_{1,i}\mathbf{1},\ i = 1, \ldots, n \tag{2.3}$$

Like the pre-exposure model (Equation 2.1), $\mathbf{x}_{1,i} = \left(x_{1,i}^{(1)}, \ldots, x_{1,i}^{(p)}\right)^\top \in \mathbb{R}^p$ denotes the i-th post-exposure signal, $a_{1,i}$ and $b_{1,i}$ represent the multiplicative error and the offset shift, respectively. Note that here $a_{1,i}$ and $b_{1,i}$ are also independent on the $a_{0,i}$ and $b_{0,i}$ in the pre-exposure signals. The error $\boldsymbol{\varepsilon}_{1,i}$ is the noise vector following the same distribution as $\boldsymbol{\varepsilon}_{0,i}$, and is independent on $\boldsymbol{\varepsilon}_{0,i}$.

Similar to the pre-exposure model (Equation 2.1), the parameters in the post-exposure model (3) are not identifiable, and therefore, the additional constraint $\|\mathbf{g}\|^2 = 1$ is imposed. Also, each element of $\mathbf{g}$ is assumed to be close to 0, since the change of the chemical composition caused by the surface treatment corresponds to certain peaks on an FTIR signal rather than all frequency bands on the FTIR signal. Note that the magnitude vector $\boldsymbol{\delta}$ is very flexible without further constraints.

In the above pre-exposure model (Equation 2.1) and post-exposure model (3), the uncertainties involved with the FTIR measurements and the effect of the exterior treatment on the CFRP surfaces are fully characterized. In the following subsections, a two-step procedure is developed to estimate the template signal $\mathbf{x}_0$, the pattern of the signal change $\mathbf{g}$ and the magnitude of the signal change $\boldsymbol{\delta}$. In the first step, the pre-exposure signals are used to estimate the template signal $\mathbf{x_0}$. And in the second step, the template signal $\mathbf{x_0}$ estimated in Step 1 is regarded as known and fixed, and the post-exposure signals are used to estimate the pattern of modification $\mathbf{g}$ and the vector of effect $\boldsymbol{\delta}$.

2.2.2 Step 1: Estimate the Template Spectra $\mathbf{x}_0$

In Step 1, our objective is to estimate the template signal $\mathbf{x}_0$ in model (Equation 2.1) from the pre-exposure FTIR measurements $\mathbf{x}_{0,1}, \mathbf{x}_{0,2}, \ldots, \mathbf{x}_{0,n}$. Recall that the existing ad-hoc

methods for estimating the template signal have no guarantee to eliminate the error to the greatest extent [5]. In this study, the maximmum likelihood estimation (MLE) principle is adopted to develop a computational efficient algorithm to estimate $\mathbf{a}_0,\ \mathbf{b}_0$, and $\mathbf{x}_0$.

Based on the pre-exposure model (1), it is clear that $\mathbf{x}_{0,i} \sim N\left(a_{0,i}\mathbf{x}_0 + b_{0,i}\mathbf{1},\ a_{0,i}^2\sigma^2\mathbf{I}\right)$, where $\sigma^2 = \mathrm{var}(\varepsilon_{0,i}^{(j)})$. Thus, the log-likelihood function is

$$\ell\left(\boldsymbol{a}_0, \boldsymbol{b}_0, \mathbf{x}_0; \mathbf{x}_{0,\mathrm{i}}\right) = -\frac{n}{2}\ln\left(2\pi\sigma^2\right) - \sum_{i=1}^{n}\frac{\|\mathbf{x}_{0,i} - a_{0,i}\mathbf{x}_0 - b_{0,i}\mathbf{1}\|^2}{2a_{0,i}^2\sigma^2} - \sum_{i=1}^{n}\ln|a_{0,i}| \quad (2.4)$$

Note that the log-likelihood function has to be optimized subject to the constraints in (Equation 2.2). It is computationally challenging to find the solution for this constrained optimization jointly over the parameter space ($\mathbf{a}_0,\ \mathbf{b}_0,\ \sigma^2,\ \mathbf{x}_0$) of the dimension $2n + 1 + (p-1) = 2n+p$. To circumvent this difficulty and focus on the parameters $\mathbf{x}_0$, we propose to investigate the main term related to $\mathbf{x}_0$ in the (Equation 2.4) and minimize the objective function:

$$\sum_{i=1}^{n}\|\mathbf{x}_{0,i} - a_{0,i}\mathbf{x}_0 - b_{0,i}\mathbf{1}\|^2/a_{0,i}^2$$

Re-parameterize $c_{0,i} = a_{0,i}^{-1}$ and $d_{0,i} = -a_{0,i}^{-1}b_{0,i}$ and apply the constraints in the model (1), the optimization problem needs to be solved becomes as follows:

$$\begin{aligned} &\min_{\mathbf{x}_0,\mathbf{c}_0,\mathbf{d}_0}\sum_{i=1}^{n}\|c_{0,i}\mathbf{x}_{0,i} + d_{0,i}\mathbf{1} - \mathbf{x}_0\|^2 \\ &\text{subject to} \quad \mathbf{x}_0^\top 1 = 0,\ \|\mathbf{x}_0\|^2 = 1 \end{aligned} \quad (2.5)$$

where $\mathbf{c}_0 = (c_{0,1}, \ldots, c_{0,n})^\top$ and $\mathbf{d}_0 = (d_{0,1}, \ldots, d_{0,n})^\top$, and $\|\cdot\|$ represents the Euclidian norm. The parameters $a_{0,i},\ b_{0,i}$ can be computed by $c_{0,i}^{-1}$ and $-c_{0,i}^{-1}d_{0,i}$, respectively.

Given $\mathbf{x}_0$, the optimal value of $c_{0,i},\ d_{0,i}$ can be calculated from solving least square

problems:

$$\begin{bmatrix} \hat{c}_{0,i}\left(\mathbf{x}_0\right) \\ \hat{d}_{0,i}\left(\mathbf{x}_0\right) \end{bmatrix} = \begin{bmatrix} \mathbf{x}_{0,i}^\top \mathbf{x}_{0,i} & \mathbf{x}_{0,i}^\top \mathbf{1} \\ \mathbf{1}^\top \mathbf{x}_{0,i} & p \end{bmatrix}^{-1} \begin{bmatrix} \mathbf{x}_{0,i}^\top \mathbf{x}_0 \\ \mathbf{1}^\top \mathbf{x}_0 \end{bmatrix}$$

Plug them in (Equation 2.1) and denote $\mathbf{H}_i = \mathbf{x}_{0,i}\mathbf{x}_{0,i}^\top \left(\mathbf{x}_{0,i}^\top \mathbf{x}_{0,i}\right)^{-1} \left[\mathbf{I} - \frac{\mathbf{1}\mathbf{1}^\top}{p}\right]$, the objective of (Equation 2.5) is transformed to

$$f\left(\mathbf{x}_0, \mathbf{c}_0\left(\mathbf{x}_0\right), \mathbf{d}_0\left(\mathbf{x}_0\right)\right) = \sum_{i=1}^{n} \left\|\mathbf{H}_i \mathbf{x}_0 - \mathbf{x}_0\right\|^2$$

Then, it can be further written as $f\left(\mathbf{x}_0, \mathbf{c}_0\left(\mathbf{x}_0\right), \mathbf{d}_0\left(\mathbf{x}_0\right)\right) = \mathbf{x}_0^\top \mathbf{M} \mathbf{x}_0$, where $\mathbf{M} = \sum_{i=1}^{n} \mathbf{V}_i^\top \mathbf{V}_i$, and $\mathbf{V}_i = \mathbf{H}_i - \mathbf{I}$, and thus the problem (Equation 2.5) is transformed to

$$\begin{aligned} &\min_{\mathbf{x}_0, \mathbf{c}_0, \mathbf{d}_0} \mathbf{x}_0^\top \mathbf{M} \mathbf{x}_0 \\ &\text{subject to} \quad \mathbf{x}_0^\top \mathbf{1} = 0,\ \left\|\mathbf{x}_0\right\|^2 = 1 \end{aligned} \tag{2.6}$$

The objective function becomes a quadratic function of $\mathbf{x}_0$, and thus the problem is essentially an eigen problem with linear constraint. It can be shown that the solution $\hat{\mathbf{x}}_0$ to this problem is $\mathbf{P}\mathbf{v}$, where $\mathbf{P} = \mathbf{I} - \mathbf{1}\mathbf{1}^\top$ and $\mathbf{v}$ is the eigenvector of $\mathbf{PMP}$ corresponding to the smallest eigenvalue [30].

2.2.3 Step 2: Estimate $\boldsymbol{\delta}$ and $\mathbf{g}$ from the Post-exposure Spectra

In Step 1, the estimation of the template signal $\mathbf{x}_0$ was obtained from the last step based on the pre-exposure signals. In Step 2, this template is regarded as known and our objective is to estimate $\mathbf{g} \in \mathbb{R}^p$ and $\boldsymbol{\delta} = \left(\delta_1, \ldots, \delta_n\right)^\top$ from the post-exposure signals. Like problem (Equation 2.5), the $\boldsymbol{\delta},\ \mathbf{g}$ can be estimated by solving the following least square problem

(Equation 2.7):

$$\min_{\boldsymbol{\delta},\mathbf{g}_1,\mathbf{c}_1,\mathbf{d}_1} \sum_{i=1}^{n} \|c_{1,i}\mathbf{x}_{1,i} + d_{1,i}\mathbf{1} - (\mathbf{x}_0 + \delta_{\mathrm{i}}\mathbf{g})\|_2^2$$
$$\text{subject to} \quad \|\mathbf{g}\|^2 = 1 \tag{2.7}$$

However, similar to the problem in Step 1, the parameters $c_{1,i}$, $d_{1,i}$, and δ_i are not identifiable without further constraints. To solve the identifiability issue, the pattern of modification $\mathbf{g}$ can be any function obtained from the linear combination of $\tilde{\mathbf{g}}, \mathbf{1}$ and $\mathbf{x}_0$, where $\tilde{\mathbf{g}}$ is the component of $\mathbf{g}$ in the null space of $\mathbf{1}$ and $\mathbf{x}_0$. In what follows, the vector $\tilde{\mathbf{g}}$ is first estimated by solving problem (Equation 2.7) subject to two constraints on $\mathbf{g}$: $\mathbf{g}^\top\mathbf{x}_0 = 0$ and $\mathbf{g}^\top\mathbf{1} = 0$, which leads to problem (Equation 2.8):

$$\min_{\boldsymbol{\delta},\tilde{\mathbf{g}},\mathbf{c}_1,\mathbf{d}_1} \sum_{i=1}^{n} \|c_{1,\mathrm{i}}\mathbf{x}_{1,i} + d_{1,i}\mathbf{1} - (\mathbf{x}_0 + \delta_i\tilde{\mathbf{g}})\|_2^2$$
$$\text{subject to} \quad \tilde{\mathbf{g}}^\top\mathbf{x}_0 = \mathbf{0},\ \tilde{\mathbf{g}}^\top\mathbf{1} = \mathbf{0} \tag{2.8}$$

After that, it will be discussed that how to find the pattern of modification $\mathbf{g} = \epsilon_1\mathbf{x}_0 + \epsilon_2\mathbf{1} + \sqrt{1-\epsilon_1^2-\epsilon_2^2}\tilde{\mathbf{g}}$ with the best interpretability in the sense of minimum $\|\mathbf{g}\|_1$. Note that the reason to minimize $\|\mathbf{g}\|_1$ is because $\mathbf{g}$ is supposed to be sparse according to its physical meaning aforementioned, but the $\tilde{\mathbf{g}}$ is not sparse statistically. Rather, the most important property of $\tilde{\mathbf{g}}$ is being orthogonal to $\mathbf{x}_0$ and $\mathbf{1}$.

2.2.4 Solution Procedure for Problem (Equation 2.8)

For the simplicity of notations, the subscript "1" in $c_{1,i}$, $d_{1,i}$ and $\mathbf{x}_{1,i}$ are dropped. Then, the objective function in (Equation 2.8) can be rewritten as

$$\begin{aligned} F(\boldsymbol{\delta}, \tilde{\mathbf{g}}, \mathbf{c}, \mathbf{d}) &= \sum_{i=1}^{n} \sum_{j=1}^{p} \left(c_i x_{ij} + d_i - x_{0,j} - \delta_i \tilde{g_j}\right)^2 \\ &= \left\| \left(\mathbf{c}\mathbf{1}^\top\right) \odot \mathbf{X} + \mathbf{d}\mathbf{1}^\top - \mathbf{1}\mathbf{x}_0^\top - \boldsymbol{\delta}\tilde{\mathbf{g}}^\top \right\|_F^2 \end{aligned} \tag{2.9}$$

where $\mathbf{c} = (c_1, c_2, \ldots, c_n)^\top$, $\mathbf{d} = (d_1, d_2, \ldots, d_n)^\top$, and $\mathbf{X} = [\mathbf{x}_1, \ldots, \mathbf{x}_n]^\top$. The operator $\odot$ is the elementwise product of two matrices. To solve problem (Equation 2.9), the block-wise coordinate descent method (BCD) is proposed, as illustrated in Algorithm 1.

Algorithm 1 Block-wise Coordinate Descent Algorithm

1: Initialization: $\boldsymbol{\delta} \leftarrow \mathbf{0}$ and arbitrary $\tilde{\mathbf{g}}$
2: **loop**
3: Given $\boldsymbol{\delta}$ and $\tilde{\mathbf{g}}$, update $\mathbf{c}$ and $\mathbf{d}$:
$[\mathbf{c}, \mathbf{d}] \leftarrow \arg\min_{\mathbf{c},\mathbf{d}} F(\boldsymbol{\delta}, \tilde{\mathbf{g}}, \mathbf{c}, \mathbf{d})$;
4: Given $\mathbf{c}$ and $\mathbf{d}$, update $\boldsymbol{\delta}$ and $\tilde{\mathbf{g}}$:
$[\boldsymbol{\delta}, \tilde{\mathbf{g}}] \leftarrow \arg\min_{\boldsymbol{\delta},\tilde{\mathbf{g}}} F(\boldsymbol{\delta}, \tilde{\mathbf{g}}, \mathbf{c}, \mathbf{d})$
subject to $\tilde{\mathbf{g}}^\top \mathbf{1} = 0;\ \tilde{\mathbf{g}}^\top \mathbf{x}_0 = 0$ and $\|\tilde{\mathbf{g}}\|^2 = 1$;
5: **end loop**

In this algorithm, the optimization problem in line 3 can be solved by multiple least-square formulations to obtain $(c_i, d_i)^\top$, which can be seen from (8). The closed-form solution to line 3 is

$$\begin{bmatrix} c_i \\ d_i \end{bmatrix} = \begin{bmatrix} \mathbf{x}_i^\top \mathbf{x}_i & \mathbf{x}_i^\top \mathbf{1} \\ \mathbf{1}^\top \mathbf{x}_i & p \end{bmatrix}^{-1} \begin{bmatrix} \mathbf{x}_i^\top \left(\mathbf{x}_0 + \delta_i \tilde{\mathbf{g}}\right) \\ \mathbf{1}^\top \left(\mathbf{x}_0 + \delta_i \tilde{\mathbf{g}}\right) \end{bmatrix}$$

Denote $\mathbf{M} = \left(\mathbf{c}\mathbf{1}^\top\right) \odot \mathbf{X} + \boldsymbol{d}\mathbf{1}^\top - \mathbf{1}\mathbf{x}_0^\top$. Line 4 is equivalent with solving the problem

(Equation 2.10):

$$[\boldsymbol{\delta}, \tilde{\mathbf{g}}] = \text{argmin}_{\boldsymbol{\delta},\tilde{\mathbf{g}}} \left\|\mathbf{M} - \boldsymbol{\delta}\tilde{\mathbf{g}}^\top\right\|_F^2$$
$$\text{subject to } \tilde{\mathbf{g}}^\top \mathbf{1} = 0,\ \tilde{\mathbf{g}}^\top \mathbf{x}_0 = 0,\ \ \|\tilde{\mathbf{g}}\|^2 = 1 \tag{2.10}$$

In this formulation, the constraint $\|\tilde{\mathbf{g}}\| = 1$ specifies the scale of $\tilde{g}$, so that it has an unique solution. Note that under the constraints that $\tilde{\mathbf{g}}^\top \mathbf{1} = 0$ and $\tilde{\mathbf{g}}^\top \mathbf{x}_0 = 0$, the objective of (Equation 2.10) can be reduced to

$$\begin{aligned}
&\left\|\mathbf{M} - \boldsymbol{\delta}\tilde{\mathbf{g}}^\top\right\|_F^2 \\
=&\left\|\mathbf{M} - \widetilde{\mathbf{M}} + \widetilde{\mathbf{M}} - \boldsymbol{\delta}\tilde{\mathbf{g}}^\top\right\|_F^2 \\
=&\left\|\widetilde{\mathbf{M}}\right\|_F^2 + \left\|\mathbf{M} - \widetilde{\mathbf{M}} - \boldsymbol{\delta}\tilde{\mathbf{g}}^\top\right\|_F^2
\end{aligned}$$

where $\widetilde{\mathbf{M}} = \mathbf{H}\mathbf{M}, \mathbf{H} = \widetilde{\mathbf{X}}_0 \left(\widetilde{\mathbf{X}}_0^\top \widetilde{\mathbf{X}}_0\right)^{-1} \widetilde{\mathbf{X}}_0^\top$, and $\widetilde{\mathbf{X}}_0 = [\mathbf{1},\ \mathbf{x}_0]$. Geometrically, $\widetilde{\mathbf{M}}$ is obtained by projecting every column of $\mathbf{M}$ onto the space spanned by $\mathbf{1}$ and $\mathbf{x}_0$. Then, the minimizer of problem (Equation 2.10) can be obtained from solving the reduced-rank problem:

$$[\boldsymbol{\delta}, \tilde{\mathbf{g}}] = \arg\min_{\boldsymbol{\delta},\tilde{\mathbf{g}}} \left\|\mathbf{M} - \widetilde{\mathbf{M}} - \boldsymbol{\delta}\tilde{\mathbf{g}}^\top\right\|_F^2$$

Let the singular value decomposition of $(\mathbf{M} - \widetilde{\mathbf{M}})$ be $\mathbf{M} - \widetilde{\mathbf{M}} = \sum_k \lambda_k \mathbf{u}_k \mathbf{v}_k^\top$, with $\lambda_1 \geq \lambda_2 \geq \cdots$. The solution $\tilde{\mathbf{g}}$ is the first right singular vector $\mathbf{v}_1$, and $\boldsymbol{\delta}$ is $\lambda_1 \mathbf{u}_1$. See, for example, Theorem 2.4.8 of Golub et al. [31].

2.2.5 Find the Most Interpretable Pattern of Modification g

After $\tilde{\mathbf{g}}$ is obtained from last step, the pattern of modification $\mathbf{g}$ can be any function obtained from the linear combination of $\tilde{\mathbf{g}}, \mathbf{1}$ and $\mathbf{x}_0$. As our objective is to understand the change of chemical components, it is desirable for $\mathbf{g}$ to be close to zero in most elements, corresponding to frequencies that are not the peaks of the FTIR signal. For this reason,

we aim to find $\theta \in [0, 2\pi]$ and $\phi \in [0, \pi]$ to minimize $G(\theta, \phi) = \|\mathbf{g}(\theta, \phi)\|_1$, where $\mathbf{g}(\theta, \phi) = \tilde{\mathbf{g}} \cos\phi + \frac{\mathbf{1}}{\sqrt{p}} \cos\theta \sin\phi + \mathbf{x}_0 \sin\theta \sin\phi$. After solving

$$(\theta^*, \phi^*) = \arg\min_{\theta,\phi} G(\theta, \phi)$$

the pattern of modification $\mathbf{g}$ is obtained as

$$\mathbf{g}(\theta^*, \phi^*) = \tilde{\mathbf{g}} \cos\phi^* + \frac{\mathbf{1}}{\sqrt{p}} \cos\theta^* \sin\phi^* + \mathbf{x}_0 \sin\theta^* \sin\phi^*$$

As discussed earlier, the pattern of modification $\mathbf{g}$ will help us understand the change of chemicals: it provides a map of the treatment effect on all frequency bands, giving comprehensive information on how the chemical bonds change as a result of the surface treatment.

For a better and easier understanding, the proposed two-step procedure is visualized in the flow chart in Figure 2.4. The template signal $\mathbf{x_0}$ is estimated from the pre-exposure signals first. And then, with the known template signal $\mathbf{x_0}$, the pattern of modification $\mathbf{g}$ and the vector of effect $\boldsymbol{\delta}$ are estimated from the post-exposure signals. Note that the final $\mathbf{g}$ with the best interpretability is obtained after a little bit of further optimization.

2.3 Simulation Study

In this section, the proposed two-step methodology is implemented on synthetic data with the uncertainties described in Section 2.2 to validate its effectiveness.

In our simulation, to mimic the real experimental data, the true template signal $\mathbf{x}_0$ is chosen by averaging and standardizing some signals obtained from the experiment. First, the pre-exposure signals are generated from the template signal $\mathbf{x}_0$ according to our model: $\mathbf{x}_{0,i} = a_{0,i}(\mathbf{x}_0 + \varepsilon_{0,i}) + b_{0,i}\mathbf{1}, i = 1, \ldots, 33$. Then, to generate the post-exposure signals, the true value for the vector of effect is designed as $\boldsymbol{\delta} = [8\ 5\ 3\ 2\ 2\ 2\ 2\ 2\ 2]^\top$, as shown in Figure 2.5. The simulated pattern of modification $\mathbf{g}$ is shown in Figure 2.6. For each $\delta_i, i = 1, \ldots, 9$, three post-exposure signals are generated by adding $\delta_i \mathbf{g}$ onto the baseline signals

[htb]

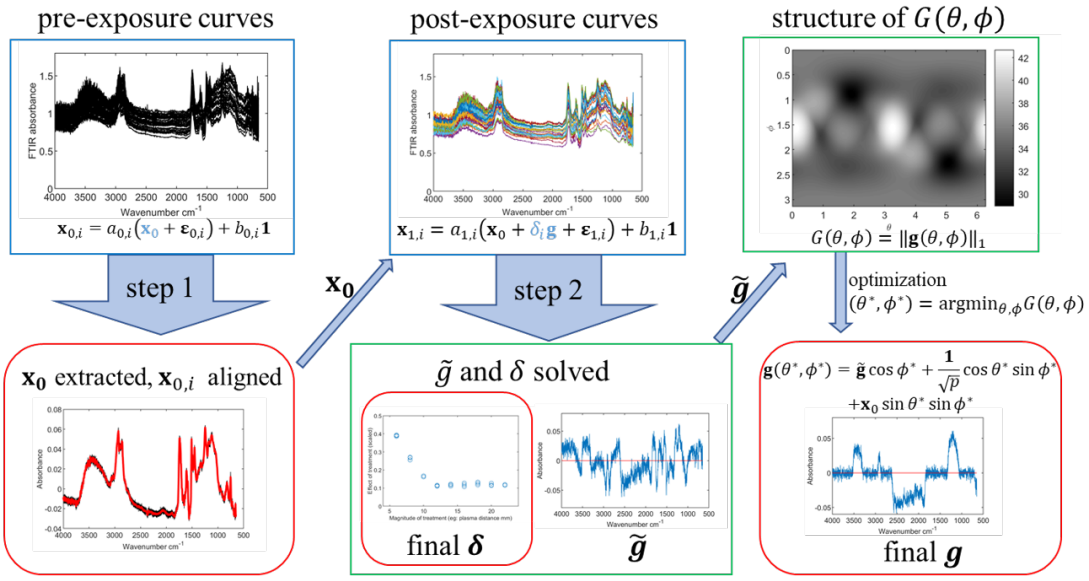

Figure 2.4: Our proposed two-step framework.

that are also subject to the aforementioned uncertainties: $\mathbf{x}_{1,i} = a_{1,i}\left(\mathbf{x}_0 + \delta_i \mathbf{g} + \boldsymbol{\varepsilon}_{1,i}\right) + b_{1,i}\mathbf{1}$, $i = 1, \ldots, 27$. As a result, 27 post-exposure signals are obtained as shown in Figure 2.7. Here, the number of synthetic signals, 33 for pre-exposure and 27 for post-exposure, is set in consistency with the sample size in our experiments to be detailed in the next section. The analysis of the real data will be illustrated in the next section as well.

In Step 1, the template signal $\mathbf{x}_0$ with the aligned pre-exposure FTIR signals are estimated by solving problem (Equation 2.5), and the result is shown in Figure 2.8 (a). The thinner lines are the aligned pre-exposure signals $\hat{c}_{0,i}\mathbf{x}_{0,i} + \hat{d}_{0,i}\mathbf{1}$, and the wider line in the middle is the reconstructed template signal $\mathbf{x}_0$. Compared with the raw data seen in Figure 2.7, the pre-exposure signals are well aligned. Figure 2.8 (b) shows the comparison of the true template signal and the reconstructed template signal estimated by the proposed algorithm. The two curves almost coincide, which implies that the template signal is extracted accurately and thus the effectiveness of the proposed algorithm on pre-exposure FTIR spectra is verified.

Then, the pre-exposure template FTIR signal $\mathbf{x}_0$ is regarded as known and the proposed

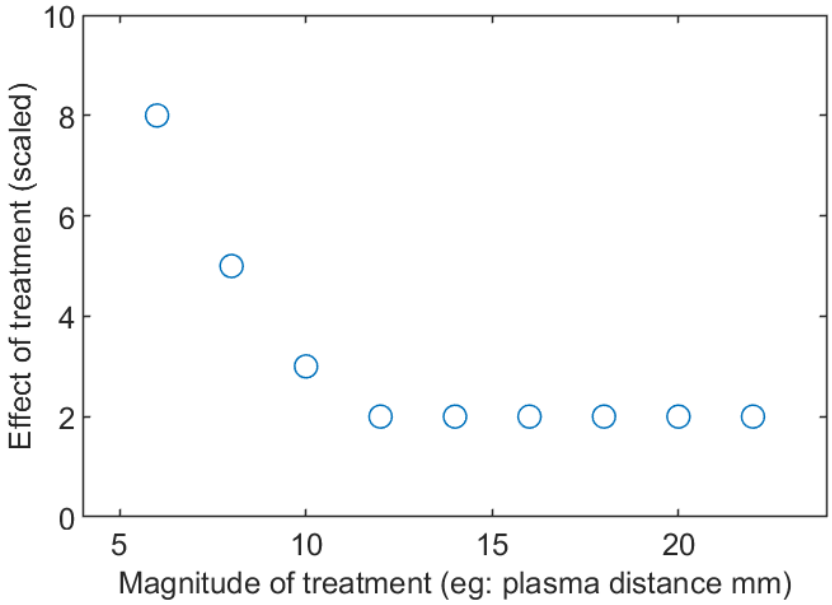

Figure 2.5: Simulated $\boldsymbol{\delta}$ function.

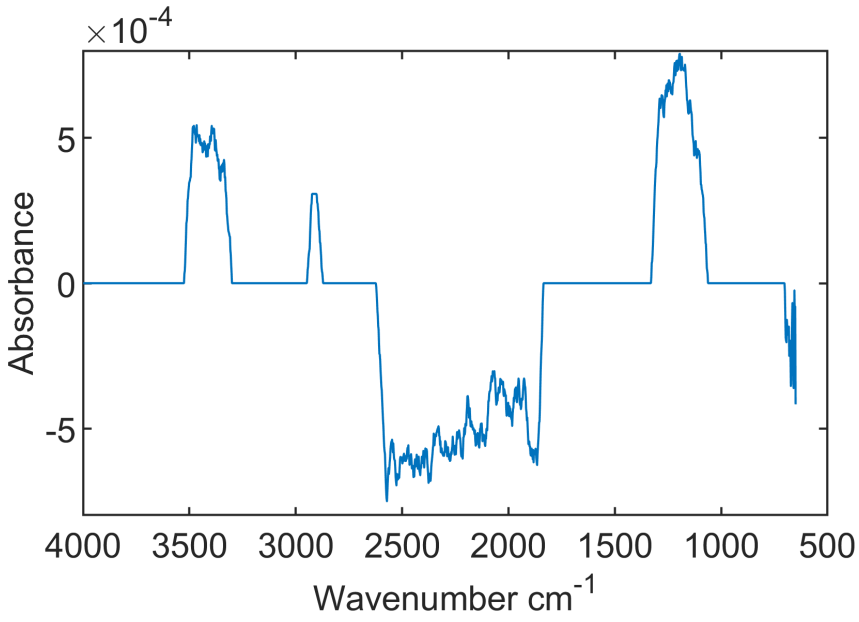

Figure 2.6: Simulated g function.

BCD algorithm is implemented on the simulated post-exposure signals to estimate the vector of effect $\boldsymbol{\delta}$ and the pattern of modification g. After solving the problem (Equation 2.8), the estimation of the vector of effect $\boldsymbol{\delta}$ and component of the pattern of modification $\tilde{\mathrm{g}}$ are

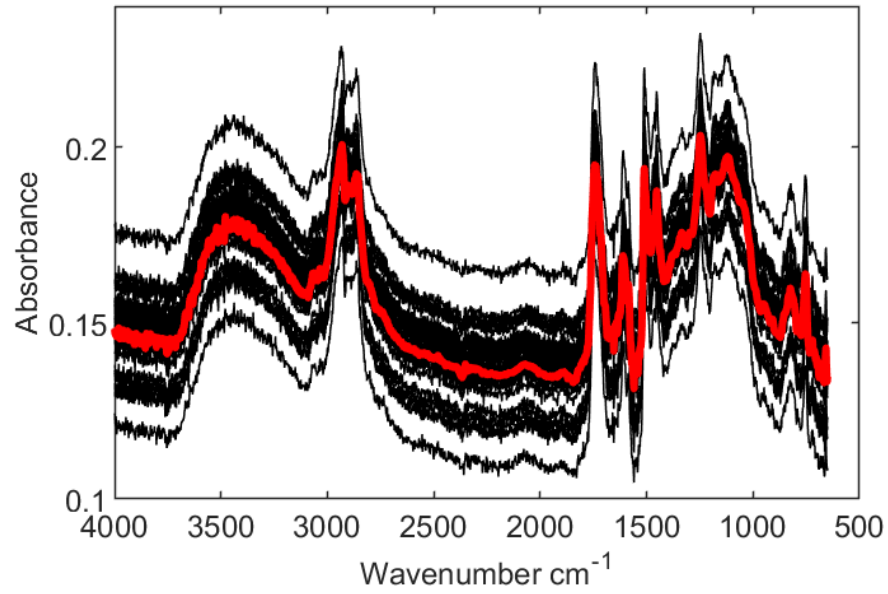

(a) Simulated pre-exposure signals (the thinner lines) and the true template signal $\mathbf{x}_0$ (the wider line in the middle)

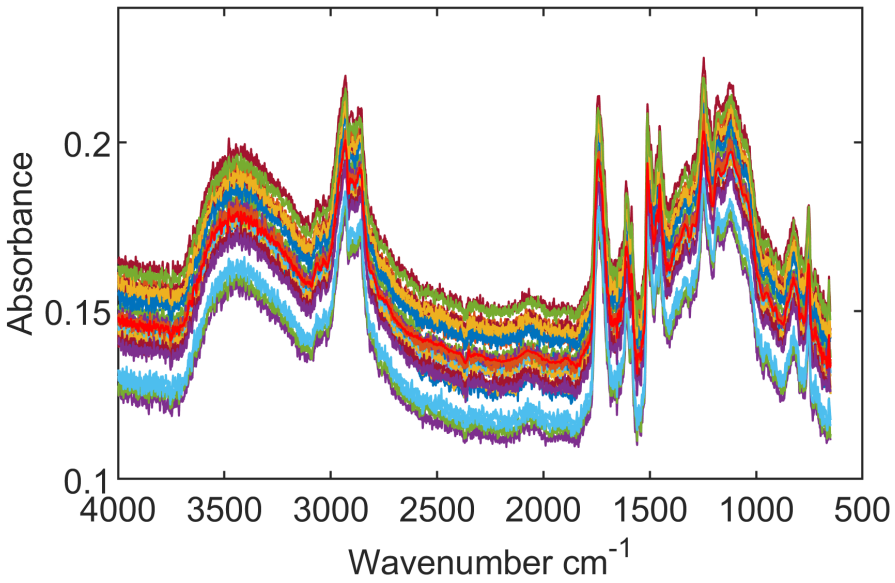

(b) Simulated post-exposure signals

Figure 2.7: Simulated FTIR signals.

obtained, as shown in Figure 2.9 and Figure 2.10.

In Figure 2.9, the estimated vector of effect $\boldsymbol{\delta}$ is plotted against the treatment magnitude. From this figure, it can be seen that the shape of $\boldsymbol{\delta}$ is very similar to that of the true

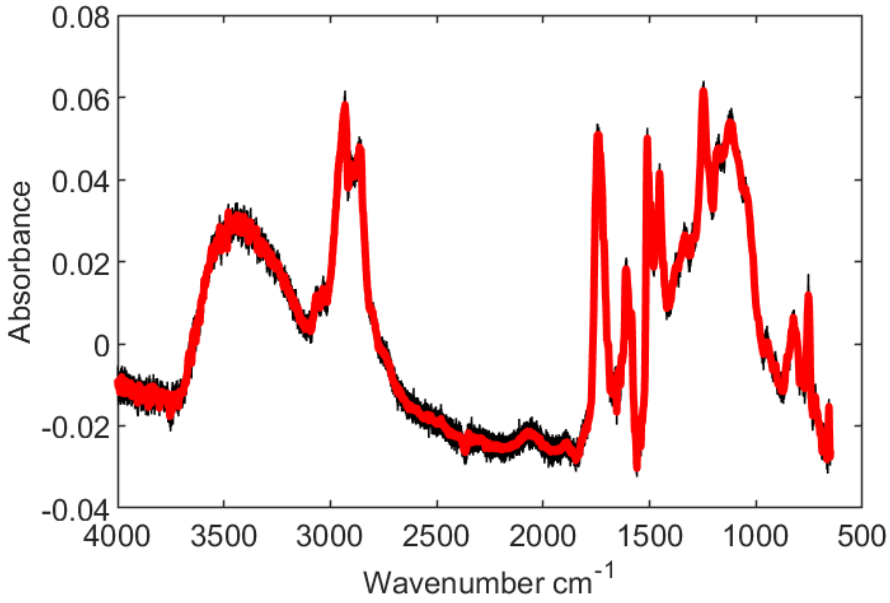

(a) Corrected simulated pre-exposure FTIR signals and the reconstructed template signal (the wider line in the middle)

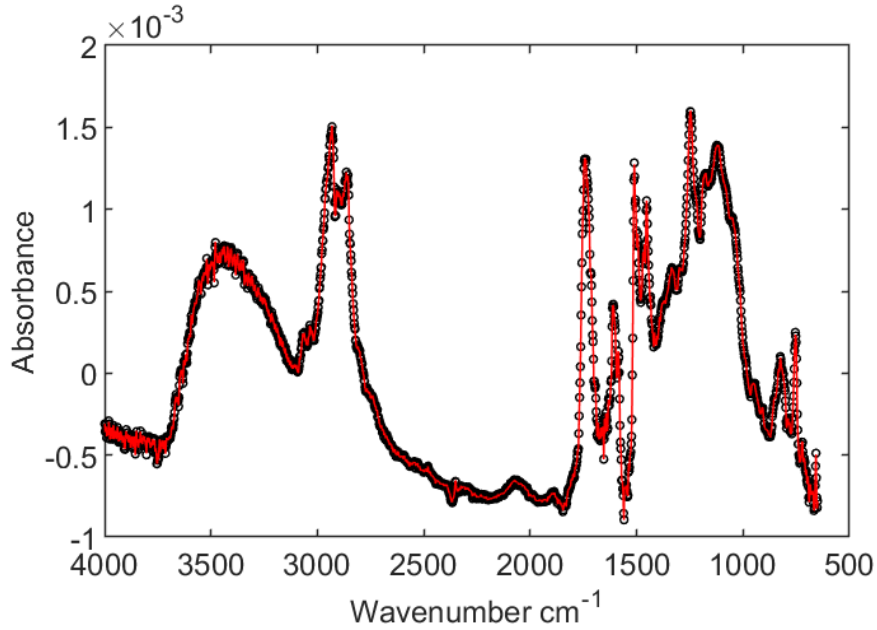

(b) (b) Comparison of normalized true template signal (solid line) and reconstructed template signal (circles) estimated by the proposed algorithm

Figure 2.8: Estimation results of proposed Step 1 on the simulated data in Fig Figure 2.7 (a).

value $\boldsymbol{\delta}$ illustrated in Figure 2.5. It verifies that the accuracy of the proposed algorithm on estimating the vector of effect $\boldsymbol{\delta}$. Though the estimated vector of effect $\boldsymbol{\delta}$ has a differ-

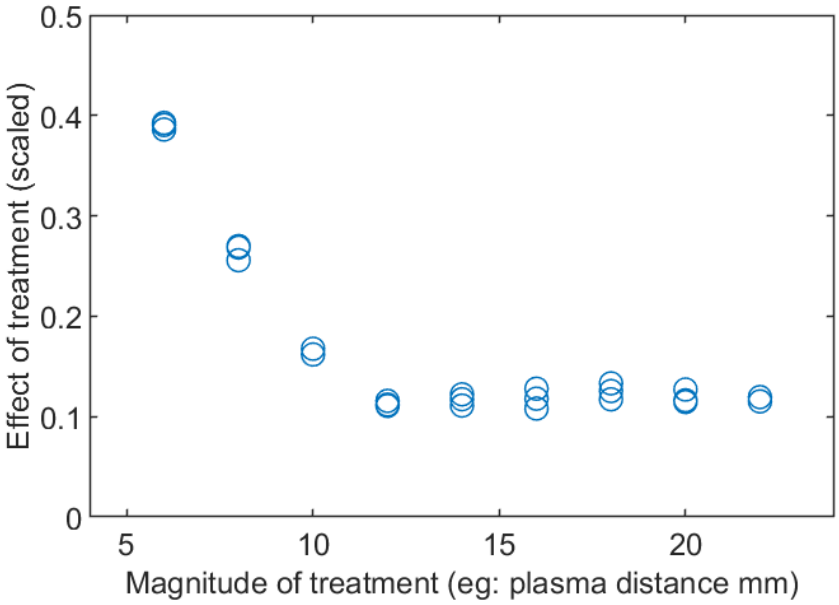

Figure 2.9: The δ function reconstructed by the proposed procedure.

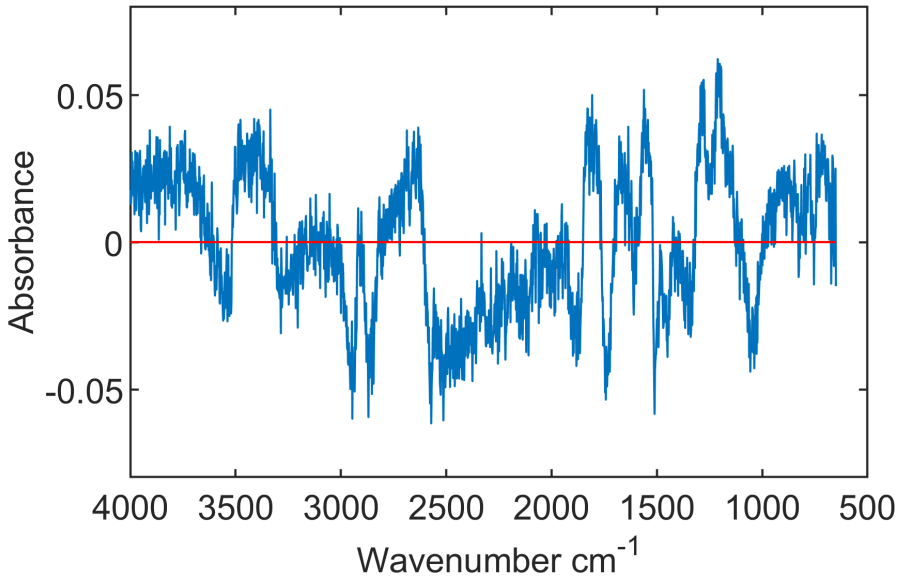

Figure 2.10: The reconstructed $\tilde{\mathbf{g}}$ solved from (Equation 2.8).

ent magnitude from the ground-truth in Figure 2.5 due to the constraint on its scale, their trends are very similar. The small variation between them is caused by the estimation error of $\mathbf{a}_1, \mathbf{b}_1$, and the random error $\boldsymbol{\varepsilon}_1$.

Figure 2.10 illustrates the shape of $\tilde{\mathbf{g}}$. To find the pattern of modification $\mathbf{g}$ with the best

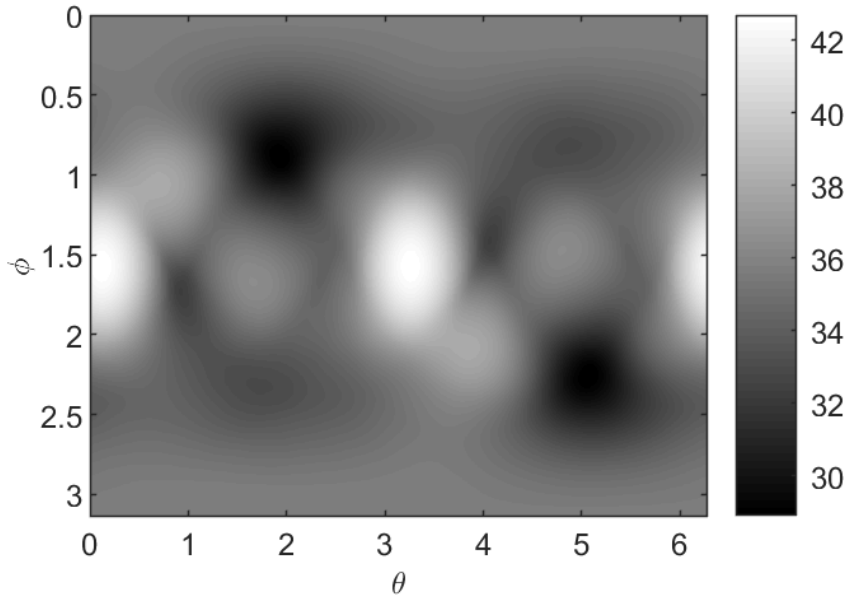

Figure 2.11: The plot of function $G(\theta, \phi)$ for simulation data, where $\theta \in [0, 2\pi], \phi \in [0, \pi]$.

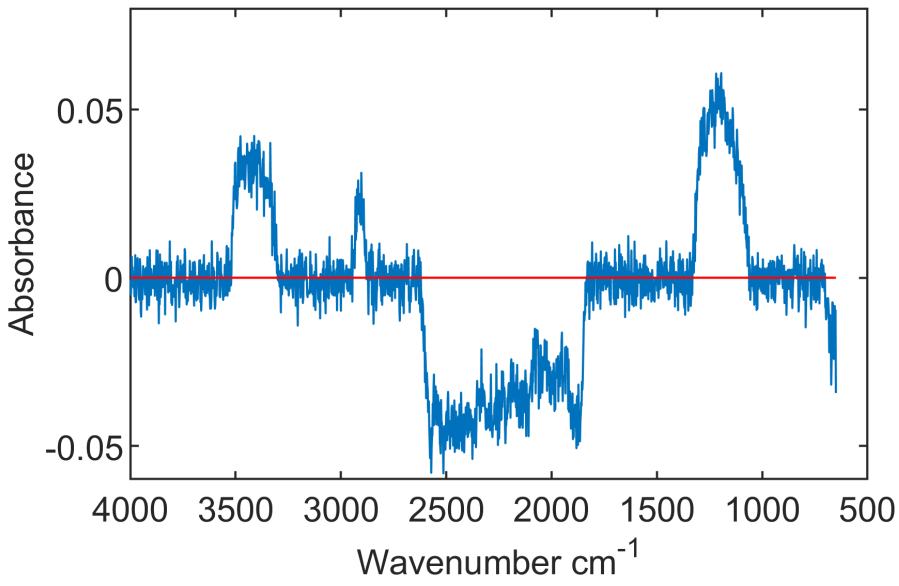

Figure 2.12: The g function reconstructed by the proposed procedure.

interpretability, we need to find θ^*, ϕ^* that minimize the value of $G(\theta, \phi)$. To understand the structure of $G(\theta, \phi)$, its values are plotted for all $\theta \in [0, 2\pi]$ and $\phi \in [0, \pi]$, as shown in Figure 2.11. From this figure, it can be seen that $G(\theta, \phi)$ is highly non-convex with

multiple local minima. Among these local minima, the one with $\phi \approx 0$ or $\phi \approx \pi$ is selected as an optimum, as the function $\mathbf{g}$ is desired to be mainly determined by $\tilde{\mathbf{g}}$, and thus $\cos(\phi)$ be close to 1. Therefore, the local optimum is determined to be $\theta^* = 1.8972,\ \phi^* = 0.8741$, and the resulted vector of $\mathbf{g}$ is illustrated in Figure 2.12.

The estimated $\mathbf{g}$ function in Figure 2.12 is consistent with the ground-truth of $\mathbf{g}$ in Figure 2.6. Our simulation study verifies the accuracy of the proposed algorithm on the estimation of $\mathbf{g}$ as well. Note that the magnitude of the absorbance is significantly different from the ground-truth in Figure 2.6. Similar to the reconstructed $\boldsymbol{\delta}$ function, such difference is believed to be caused by the constraints in solving the optimization problem. The shape of $\hat{\mathbf{g}}$ is close to $\mathbf{g}$ thereof.

There are several obstacles for us to fairly compare the performance of existing approaches with the proposed two-step procedure. First, in the signal correction step, the performance of the proposed method is very similar to the SNV and MSC. It has been proved in [9, 32] that the SNV and MSC are linearly interchangeable: $\mathbf{x}_{MSC} \approx \mathbf{x}_{SNV} \cdot \overline{s_{\mathbf{X}}} + \overline{\overline{\mathbf{X}}}$, where $\bar{s}_{\mathrm{x}}$ is the average standard deviation of all spectra, and $\overline{\overline{\mathbf{X}}}$ is the grand mean over all spectra. Our proposed method is also similar to MSC, except the idea behind: the reference spectrum is estimated by formulating an MLE optimization problem rather than set a known reference spectrum, and an adjusted variance term is adopted. Secondly, for the univariate effect quantification step, there are little existing comparable ways for extracting the pattern of the effect $\mathbf{g}$ and the magnitude of that effect $\boldsymbol{\delta}$.

2.4 Case Study: Investigation of Real FTIR Spectra

The study is motivated by the engineering problem of understanding the effect of plasma exposure on the CFRP panels at various plasma distance. In this section, we further demonstrate how to implement the proposed method to quantify the effect of plasma exposure, and discuss how the results benefit manufacturing engineering. First, the setting of the experiment is introduced to illustrate how the pre-exposure and post-exposure FTIR signals

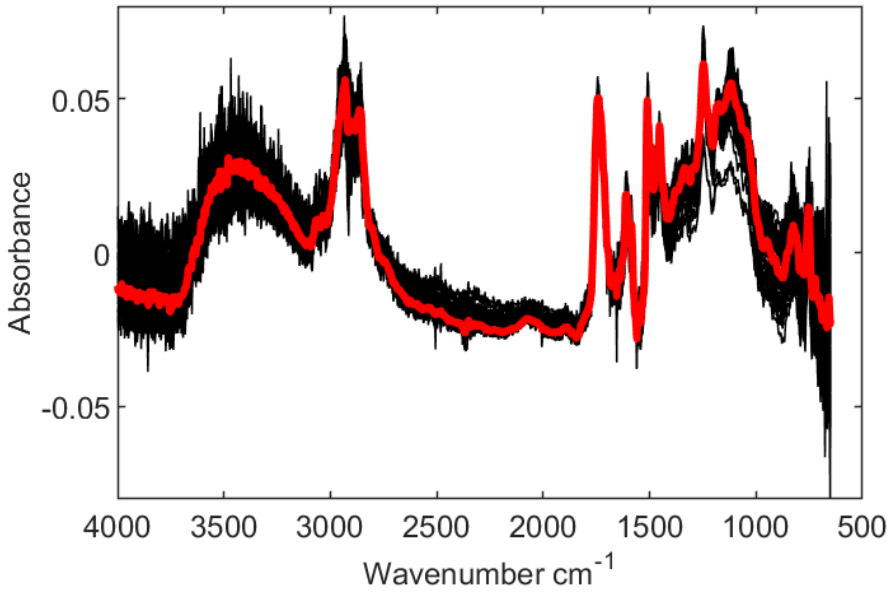

Figure 2.13: Corrected pre-exposure FTIR signals from real experiments and the template signal (the wider line in the middle).

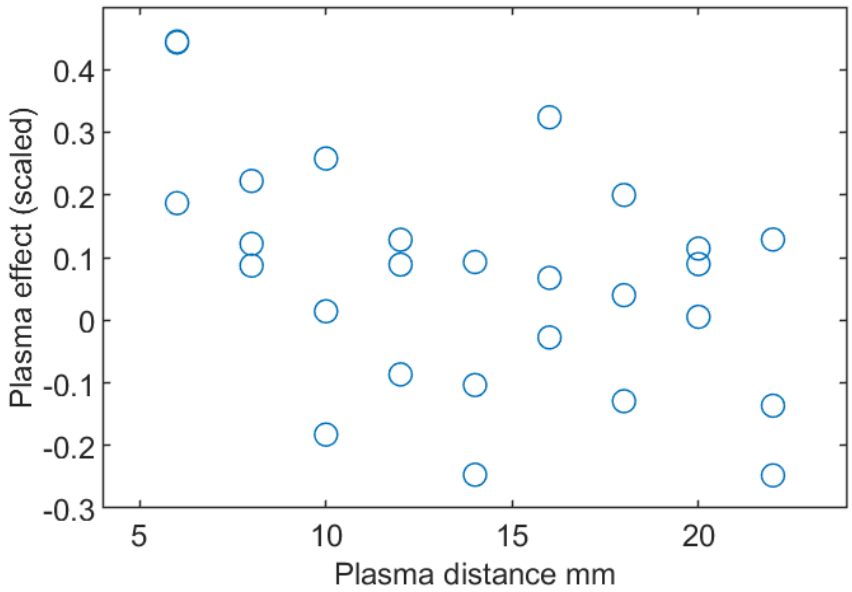

Figure 2.14: The effect of plasma exposure δ versus the corresponding plasma distance in real experiments.

are collected when the plasma distance varies. Then, the proposed analysis procedure is demonstrated in detail and our findings are then discussed.

2.4.1 Experiments

The experiment is elaborated in Figure 2.1. The goal of this experiment is investigating the effect of plasma exposure on the CFRP panels at various plasma distance. Four steps are conducted sequentially in this experiment to collect data.

First, prepare test coupons. Eleven $1" \times 1"$ CFRP test coupons are prepared from the same batch of CFRP panels. The CFRP panels are manually fabricated with carbon fiber called # 1530 3K Plain Weave Carbon Fiber Fabric, the product of Fibre Glast, and HexPly® M20 266°F (130°C) curing epoxy matrix, the product of Hexcel®. To avoid potential interference, the CFRP panels are specially kept clean and pristine without any sanding or artificial contamination.

After preparing the CFRP test coupons, take the FTIR signal measurements three times on each of the eleven test coupons to obtain $n = 33$ pre-exposure FTIR spectra. The FTIR spectrometer adopted in our experiment is 4300 Handheld FTIR from Agilent Company. On a small area on the sample, about $200\mu m^2$ at wavenumber $1700cm^{-1}$, it captures the absorbance intensity of infrared light whose wavenumber (determined by frequency) is between 650cm^{-1} and 4000cm^{-1}. Within this range, each FTIR spectrum is represented by a signal containing $p = 1798$ equidistant data points. The pre-exposure FTIR signals are denoted as $\mathbf{x}_{0,1}, \ldots, \mathbf{x}_{0,n} \in \mathbb{R}^p$ and plotted in Figure 2.2 (a).

Then, these eleven test coupons are processed with atmospheric plasma with prescribed plasma distances $h = 2$mm, 4mm, ..., 22mm in order to understand the effect of plasma treatment when the plasma distance varies. In this study, the plasma distance is chosen as the univariate factor to illustrate our methodology because it is one of the factors that our industrial collaborators are most interested in. The plasma distance is set by manually adjusting the relative location of the plasma nozzle to the plasma platform. And the range and step size of plasma distance is designed by our engineer according to visual observation on the plasma torch in our lab experimental scenario.

Finally, three repeated FTIR measurements are taken again on each test coupon soon

after plasma treatment, with the same procedure as the pre-exposure measurement. Similarly, the post-exposure FTIR signals are denoted as $\mathbf{x}_{1,1}, \ldots, \mathbf{x}_{1,n} \in \mathbb{R}^p$, and plotted in Figure 2.2 (b), where multiple colors are used to distinguish different plasma distances. Note that a reported disadvantage of plasma modification is the time dependency of the induced changes, i.e., aging [33]. Therefore, the second FTIR measurements would be performed within half an hour after plasma treatment to avoid storage stability issues [24].

It is noticed that the six post-exposure FTIR signals collected from the two coupons that underwent the plasma exposure with 2mm and 4mm plasma distances are significantly different from the signals obtained from the other coupons. Observations from the two post-exposure samples indicate that their surfaces are highly likely to be carbonized due to the excessive heat caused by the strong plasma exposure [22]. Therefore, these six FTIR measurements are eliminated from our analysis, and the post-exposure spectra contain 27 FTIR signals.

2.4.2 Implementation of the Proposed Method on Real Data

Similar to the procedure of simulation on synthetic data, the proposed methodology is implemented on real FTIR data collected from the experiment described in the last part.

In Step 1, the template signal $\mathbf{x}_0$ and the aligned pre-exposure FTIR signals are estimated by solving problem (Equation 2.5), and the result is shown in Figure 2.13. The thinner lines are all the aligned pre-exposure signals $\hat{c}_{0,i}\mathbf{x}_{0,i} + \hat{d}_{0,i}\mathbf{1}$, and the wider line in the middle is the template signal $\mathbf{x}_0$. Compared with the raw data seen in Figure 2.2, the pre-exposure signals are well aligned, and the template signal $\mathbf{x}_0$ is the representation of these curves.

Then, the proposed BCD method is implemented on the post-exposure signals to quantify the effect of plasma surface treatment. Similar to the process in the last section, the vector of effect $\boldsymbol{\delta}$ and the signal $\tilde{\mathbf{g}}$ can be obtained by solving the problem (Equation 2.8), as shown in Figure 2.14 and Figure 2.15.

The vector of effect $\boldsymbol{\delta}$ is plotted against the plasma distance in Figure 2.14. From this figure, it can be seen that the effect of the plasma treatment is more significant as the plasma distance is small, and gradually decreases as the plasma distance increases, and generally becomes constant after the plasma distance gets greater than $10mm$. From such a trend, it can be seen that a smaller plasma distance tends to cause a more significant chemical change, which corresponds to better surface quality indicated by the contact angle. This result confirms our previous experiment that the wettability of the CFRP material is higher when smaller plasma distance is used, as long as the CFRP surface is not carbonized (also mentioned in [34]).

The result in Figure 2.14 can provide a valuable guideline to plasma parameter selection during CFRP surface preprocessing in aircraft maintenance. Although there is an upper bound of plasma distance under which the plasma treatment is effective, the shape of the vector $\boldsymbol{\delta}$ tells us that 10 mm is approximately the threshold, as plasma treatment at a longer distance will barely change the FTIR curve. In other words, the analysis gives us a relatively quantitative and persuasive understanding of the surface treatment effect on the FTIR measurements.

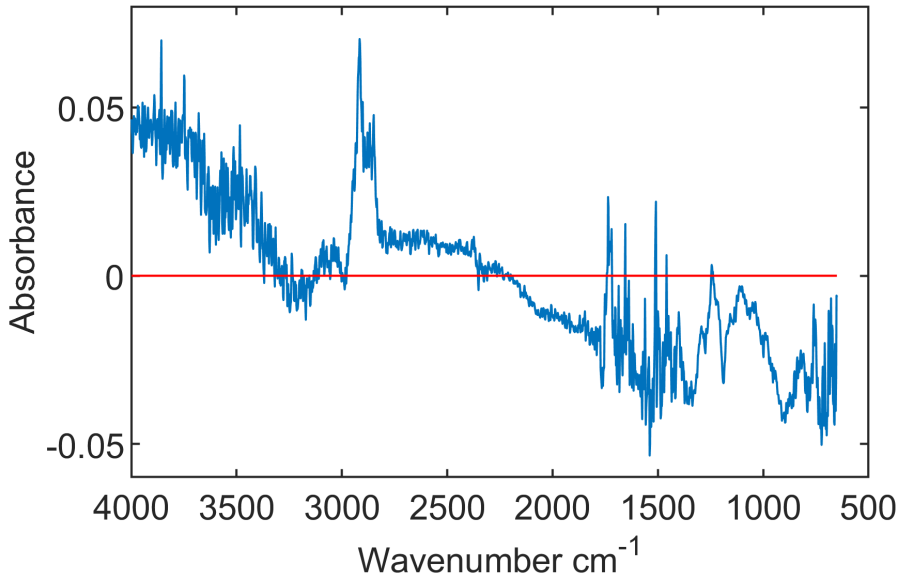

Figure 2.15: The signal $\tilde{\mathbf{g}}$, as solved from the problem (Equation 2.8).

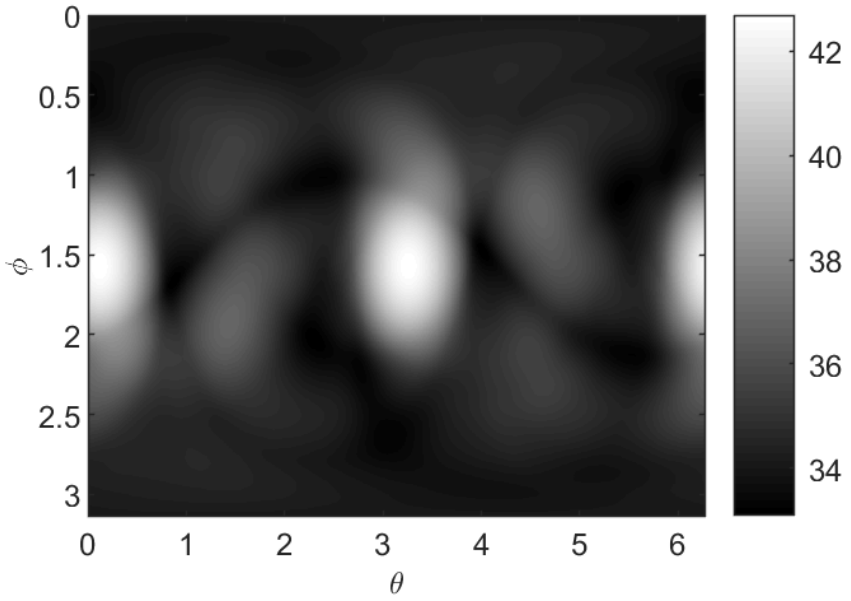

Figure 2.16: The plot of function $G(\theta, \phi)$ for real data, where $\theta \in [0, 2\pi], \phi \in [0, \pi]$.

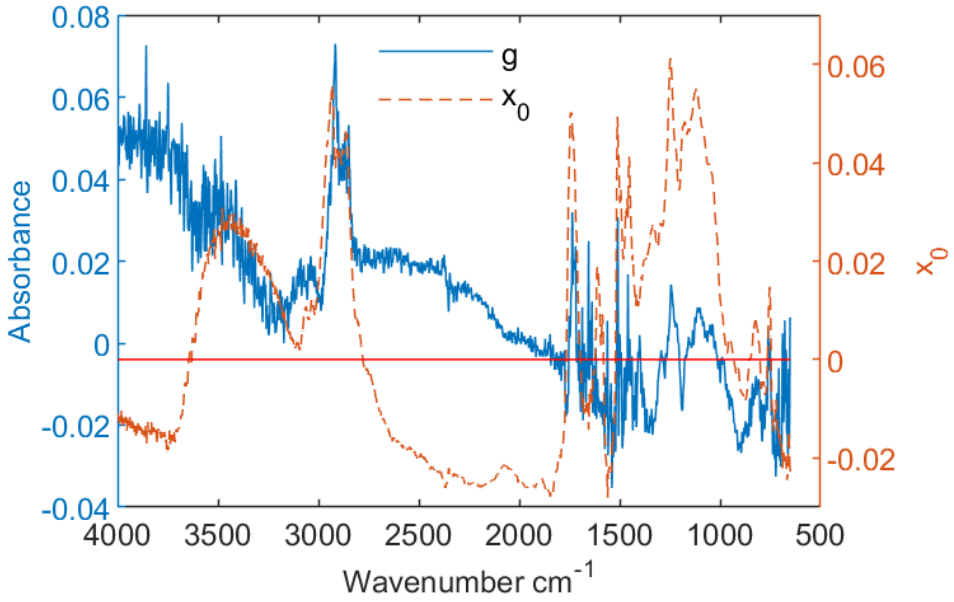

Figure 2.17: The pattern of modification g (the solid line) and the extracted template curve $\mathbf{x}_0$ (the dashed line) as reference for results explanation.

In Figure 2.15, the pattern of modification g that minimizes the value of $G(\theta, \phi)$ is found based on $\tilde{\mathbf{g}}$. The structure of $G(\theta, \phi)$ is illustrated in Figure 2.16. The local optimum is determined to be $\theta^* = 0.0009,\ \phi^* = 0.5053$, and the resulted vector of g is illustrated in

Figure 2.17.

Recall that the pattern of modification g illustrates the effect of plasma exposure on all frequency bands. The change of FTIR gives comprehensive information on how the chemical bonds changed as the result of plasma exposure [26, 18, 17]. According to the raw FTIR data shown in Figure 2.2 and chemical information of materials of the test coupons, with the help of the IR absorption table [35], it can be concluded that the peaks of FTIR signals roughly correspond to the following chemical bonds: O–H, C–H, C=O, C=C, C–O.

From Figure 2.17, it can be seen that when the wavenumber is within the range of $3200-3700cm^{-1}$, $2750-3200cm^{-1}$, $1650-1800cm^{-1}$, and $1000-1300cm^{-1}$, the pattern of modification g has several significant positive values. It implies that the corresponding chemical bonds, including O–H, C–H, C=O, and C–O, are created by plasma exposure. When wavenumber is in the range of $1600-1750cm^{-1}$ and $650-1000cm^{-1}$, the pattern of modification g oscillates and takes negative values, which implies that the corresponding chemical bonds, mainly C=C, are decreased by plasma exposure. The pattern of modification g in the rest frequency regions tends to be around zero, which means that plasma does not change the chemical bonds whose characteristic wavenumbers are in those regions.

Our result agrees with existing researches on the effects of plasma exposure on materials. For example, it is suggested in [20] that the plasma grafting to the carbon fiber surface increased the proportion of oxygen atoms, and that the plasma modified carbon fiber shows a significant increase in oxygen and nitrogen concentration [19, 22], and plasma treatment can generate chemical groups on CFRP such as O–H, –COOH,[36, 22], C=O or O–C = O [22].

Finally, it is worthwhile to note that our experiment is conducted under lab conditions. The results of the data analytics may be slightly different in real industrial processes, which involves different types of materials, different devices, and possibly other chemical stains on the sample panels. However, our analytical procedure is applicable to data collected from any process conditions, as long as the assumptions on the data given in Section 2.2.1

holds.

2.5 Conclusion and Discussion

In this article, a general procedure is proposed to quantify the effects of a certain treatment on the spectral signals subjecting to multiple uncertainties. With this procedure, two types of uncertainties in the spectral signals, offset shift and multiplicative error, are carefully addressed. In the two-step procedure, a novel optimization problem is formulated to estimate the representative template spectrum first, and then another optimization problem is formulated to obtain the pattern of modification $\mathbf{g}$ that reveals how the treatment affects the shape of the spectral signal, as well as a vector $\boldsymbol{\delta}$ that describes the degree of change caused by different treatment magnitudes.

This methodology is illustrated by a motivating example of quantifying the plasma treatment effect on CFRP coupons through FTIR measurements. In the case study, the effective range of the plasma distances is revealed from the vector of effects $\boldsymbol{\delta}$, and the affected chemical bonds are identified from the pattern of modification $\mathbf{g}$. In future research, a promising step is mapping $\mathbf{g}$ to the chemical compounds with the help of the FTIR spectra libraries [37]. The knowledge on the modification of chemicals can shed some light on how the surface treatment changes the chemical composition of the material, which further indicates which chemicals shall be added or avoided to improve the surface quality before composite joining and repairing in aircraft manufacturing and maintenance.

Our technique is suitable and promising to quantify the effect of a large class of surface treatments apart from the plasma treatment. The pattern of modification $\mathbf{g}$ reveals the general effect pattern of a certain surface treatment in a range of treatment magnitude, providing a new way to understand the intrinsic reasons behind the improvement of surface quality. Recall that the surface treatment methods have been well-developed, including thermal treatment, wet chemical or electrochemical oxidation, plasma treatment, gas-phase oxidation, coating treatment, etc., applying and extending this method to solve more prob-

lems in the manufacturing industry is a direction for our further research.

Also, the method in this article is applicable to analyze the data obtained from a wide range of spectral measurements, including ultraviolet-visible spectroscopy (UV-Vis) [38], X-ray diffraction (XRD) [39], Raman spectroscopy [40, 41] etc., when the background noise leads to uncertain offset and the uncertain signal level results in the multiplicative error. Typically, these uncertainties are of greater magnitude in real manufacturing environments than in lab conditions, due to the inexperienced operators and the uncontrolled surroundings. Therefore, the analytic methodology proposed in this article also helps to broaden the application scope of portable spectrometers, such as the handheld FTIR devices.

Finally, the methodology of this study can also be extended. For example, this study assumes that the pattern of modification $\mathbf{g}$ is identical under all levels of treatment. New methodologies can be developed in future research, based on the assumption that the pattern of modification is different for distinct levels of surface treatment.

CHAPTER 3
INCOMPLETE DATA ANALYSIS WITH AN APPLICATION ON DUCTAL GALLSTONE EVALUATION

Incomplete data must frequently be dealt with in healthcare decision making to determine accurate diagnoses and form treatment recommendations based on a limited amount of clinical data. In this study, a multistage sequential decision-making model is developed to actively collect only the necessary patient data in a sequential manner. There are two novelties in the proposed model. First, unlike the existing ordinal logistic regression model which only models a single stage, we estimate the parameters for all stages together. Second, it is assumed that the coefficients for common features in different stages are kept consistent. The effectiveness of the proposed model is validated on both a simulation cohort and testing cohort. Compared with the baseline model where the data is modeled individually and independently, the proposed model improves the estimation efficiency by 62%-1838%. For both simulation and testing cohorts, the proposed method is more effective, stable, interpretable, and computationally efficient on parameter estimation. The proposed method can be easily extended to a variety of scenarios where decision-making can be done sequentially with only necessary information.

3.1 Introduction

In this section, firstly, the background of the common bile duct stone (CBDS) is introduced and the objective is claimed. Then, with the challenge of a highly incomplete dataset, the ad-hoc methods for dealing with incomplete data are reviewed. Finally, the motivation of proposing our multistage sequential decision-making model is explained.

3.1.1 Background of the CBDS Project

Figure 3.1 shows the location of CBDS [42]. Gallstone are solid particles that can form from cholesterol, bilirubin, and other substances within the gallbladder. These densities are often benign when localized to the gallbladder, but can cause pain, infection, and liver damage when they become stuck in the common bile duct (CBD) and impede the flow of bile into the digestive tract. A stone that becomes impacted in the CBD, can be difficult to detect definitively, but its presence requires a procedural intervention, endoscopic retrograde cholangiopancreatography (ERCP). As with most procedures, ERCP requires anesthesia and carries the risk of complications, including pancreatitis, infection, and bleeding. As a result, it is imperative to ensure that ERCP is only performed when there is a stone definitively obstructing the duct. This is particularly true in children. Therefore, in this research, our objective is to definitively predict the presence of a CBD stone in a child with high accuracy and specificity.

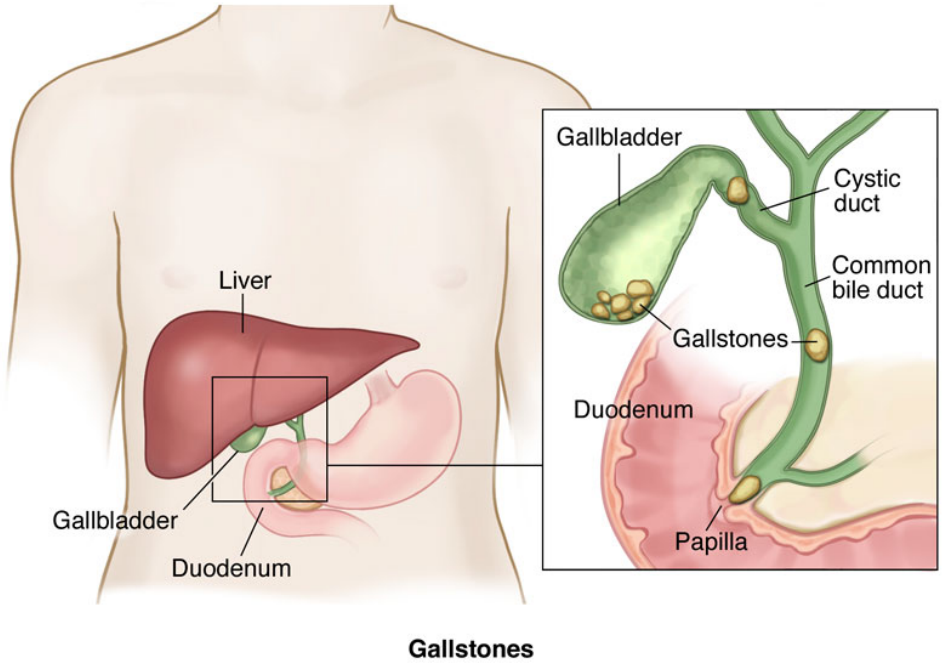

Figure 3.1: Introduction to CBDS [42]. Gallstones in CBD are tricky to detect. Failing to remove them can cause severe infection

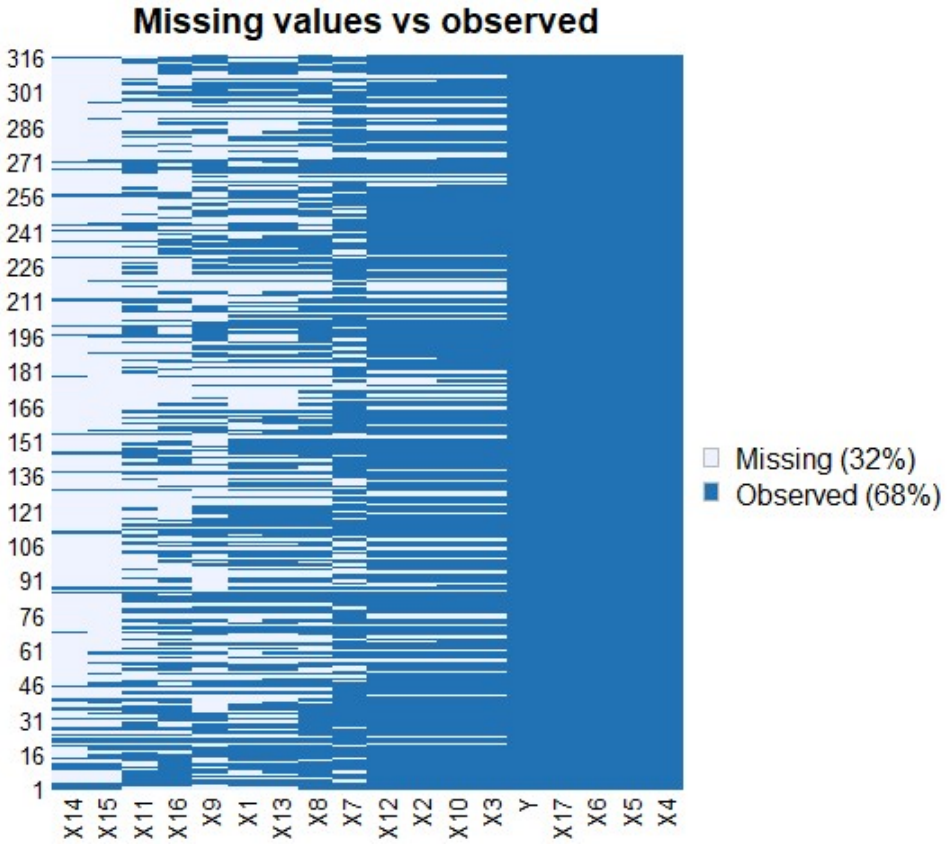

Figure 3.2: The missing map of clinical data for the gallstone evaluation.

The probalility of the existence of CBDS can be estimated from the clinical data, including demographic data, laboratory test data, and imaging data, such as MRI and US data. Given the estimated probability of the existence of the CBDS, the doctor can then decide the procedure type accordingly. For example, if the probability of the existence of the ductal gallstone is higher than 95%, the ERCP procedure will be considered. Otherwise, the Cholangiogram may be preferred to remove the gallbladder directly.

Thus, the expected outcome is the probability estimation of the existence of CBDS. The status of the existence of CBDS is either existing or not, which can be denoted as "1" (there is stone) and "0" (no stone) in a statistical way, respectively. Therefore, the modeling task is, building a predictive model for a supervised binary classification task. The model should reveal the relationship between the existence of the CBDS (response variable Y) and other features/variables (predictor variables X) from clinical trials, yet interpretable

and intuitive.

The data comes from our collaborator, doctors from Emory Pediatrics Residency Training Program. The data is collected from 316 pediatric patients, each has 17 features ($X_1 \sim X_{17}$) collected at most. The challenges associated with this clinical dataset are clear: (1) The clinical data is often precious with limited sample size. The limited data size restricts the usage of most advanced deep learning algorithms, which often require a big dataset for training and learning [43]. (2) Missing data is commonly seen for most features. Deleting features with a high missing rate will lose some treasurable data and is not acceptable. In this gallstone dataset, the missing ratio is pretty big. Figure 3.2 shows the distribution of missing values (NAs), and the table shows the number of NAs. In this case, we have to deal with the missing values first to avoid numeric issues in the computation.

For most of the popular machine learning models, more features often contain more crucial information, leading to higher modeling accuracy and more stable performance. However, in real-world scenarios, some informative features could be expensive and hard to obtain. This can be a particular problem in clinical decision making. Obtaining additional clinical data often comes with a price, including delayed time to intervention, cost, and complications. This price can be particularly high in pediatric care. As a result, a common clinical challenge is decision making based on incomplete data.

To address the issues caused by incomplete data in statistical modeling, many widely-used methods are developed according to missing patterns, such as simple deletion on feature or record, mean/median/mode/zeros substitution, regression imputation, last observation carried forward, EM, etc. [1]. In the next section, we'll briefly review the existing methods dealing with incomplete data.

3.1.2 Existing Popular Methods of Dealing With Incomplete Data

The most common ways of dealing with missing data can be summarized as follows:

1. Ad-hoc methods

- Complete case analysis. Case deletion or feature deletion.
- Mean/median/mode/"0" imputation.
- Predictive imputation. Create a model to predict variables with NAs based on other features. The predictive model can be almost every kind of predictive model, such as logistic regression, random forest, etc.
- Indicator method. Use dummy variable (1/0) indicates missing status.
- Last observation carried forward.

2. Multiple Imputation. Multiple imputation results in a number of complete datasets which can be analyzed separately and then the results combined using rules set out by Rubin [44].

3. Expecation-Maximisation (EM) algorithm. EM algorithm, introduced by Dempster et al. [45], use a maximum likelihood approach to estimate the parameters of the model.

The choice of these methods depends on the characteristics of the dataset and the target users of the model. For example, we cannot simply delete the observations with NAs, otherwise only 11 out of 316 observations (patients) are kept for analysis. Neither can we delete the features with NAs which will lead to a huge loss of information. The naïve imputation method, such as mean/mode/median imputation, cannot be convincing enough and be of a high risk of potential danger. Other widely used benchmark methods, such as substituting missing values with 0/mean/median/mode, are helpful in a way but have their drawbacks as well. To maximum the information available, we propose to learn NAs from the non-missing values as much as possible.

3.1.3 Recommended Approach for Our Clinical Dataset–KNN Imputation

The k-nearest neighbors (KNN) algorithm enables us to "guessing" the missing value based on the similarities (distance) between the patients. The first k most similar neighbors will

contribute to the estimation of the NAs of a patient. And the amount of their contribution, the weights, depends on their similarities. Thus, the key point here is the similarity measure between 2 observations. We propose to consider the following three similarity metrics:

1. Euclidean Distance: $d(x, y) = \sqrt{(x-y)S^{-1}(x-y)}$

2. Mahanlanobis Distance: $d(x, y) = \sqrt{(x-y)S^{-1}(x-y)}$

   If the S is the identity matrix, the Mahalanobis distanc becomes Euclidean distance
   If the S is diagonal, the Mahalanobis distance becomes standardized Euclidean distance.

3. Cosine Distance (Pearson correlation coefficient)

   Cosine Distance:

$$\cos(m, m') = \frac{\sum_{i=1}^{n} x_i y_i}{\sqrt{\sum_{i=1}^{n} x_i^2}\sqrt{\sum_{i=1}^{n} y_i^2}}$$

   Cosine distance is equivalent to the Pearson correlation coefficient. In detail, Cosine distance = 1 – cosine similarity. Here is the simple proof:

   Pearson correlation coefficient:

$$\rho(m, m') = \frac{\sum_j \left(X_{j,m} - \bar{X}_j\right)\left(X_{j,m'} - \bar{X}_j\right)}{\sqrt{\sum_j \left(X_{j,m} - \bar{X}_j\right)^2 \sum_j \left(X_{j,m'} - \bar{X}_j\right)^2}} = \frac{\left(V_m - \bar{V}\right)^\top \left(V_{m'} - \bar{V}\right)}{||V_m - \bar{V}||^2 \cdot ||V_{m'} - \bar{V}||^2}$$
$$= \frac{U_m^\top U_{m'}}{||U_m||^2 \cdot ||U_{m'}||^2} = \cos < U_m, U_{m'} >$$

The higher the similarity between the patients, the higher the likelihood that they have similar potential values on unseen features (NAs). Thus, the estimation for the NA is the weighted or unweighted means of the top k most similar neighbors. And if weighted, the weights depend on their similarities:

$$W_{j,m} = \frac{\sum_m' \text{sim}(m, m') X_{i,m'}}{\sum_m' |\text{sim}(m, m')|}$$

The KNN imputation is recommended because it not only works well but also makes our collaborator doctors feel reasonable. In our other research, the KNN imputation outperforms other methods in the downstream predictive modeling on the prediction of CBDS.

After the completion of the dataset, the classifier can be trained accordingly, such as logistic regression, support vector machine, decision trees, random forest, neural networks, etc. And the KNN imputation plus L_1 penalized logistic regression was adopted in one of our publications based on this dataset.

3.1.4 Motivation of Proposing the Multistage Sequential Decision-Making Model

In the last section, we briefly reviewed some popular methods of dealing with incomplete data in statistical modeling.These methods were developed from two primary approaches. One is deleting the records or features with missing values, which will lead to a waste of available data and some intrinsic problems associated with limited data size. The other approach is "guessing" or "learning" the missing data from the observed data, which can be dangerous for clinical modeling since the synthetic data brings extra uncertainties.

To circumvent such drawbacks, in this research, a multistage sequential decision-making model is proposed. We aim to develop a sequential decision-making model to help make reliable diagnostic decisions and treatment recommendations with high positive predictive value and in a cost-effective and convenient manner. In this model, some patients possess fewer laboratory results often due to test availability and provider experience, while other patients have a more comprehensive laboratory evaluation.

There are several benefits to the proposed model. This novel platform allows the healthcare provider to actively collect only the necessary data sequentially rather than collecting all the data at inception. As a result, the diagnostic process can be faster, more convenient, and cost effective, while retaining significant accuracy. In the research setting, our model offers a novel solution to address challenges raised by incomplete data through offering sequential decision-making in an active learning way. Active learning is a special case of

machine learning in which a learning algorithm can interactively query a user (or some other information source) to label new data points with the desired outputs [46]. The active learning-based model allows some missing data yet guarantees reliability and prediction accuracy, which makes the incomplete data missing "at control" rather than missing at random.

In Section 3.2, the proposed model is elaborated with a 2-stage simplest case as an example. In Section 3.3, the details and novelties about the parameter estimation for the proposed model are discussed. In Section 3.4, the performance of the proposed methodology on synthetic data is reported. In section 3.5, the analytical result on our real clinical data is demonstrated. Finally, the article is concluded with further discussion in Section 3.6.

3.2 Proposed Active Learning-Based Multistage Sequential Decision-Making Model

In this section, first, we'll formulate the problem in detail. Then, the framework of the proposed active learning multistage sequential decision-making model is illustrated. Finally, to clarify the details of the proposed model, such as data organization and model formulation, a 2-stage model is elaborated as the simplest example.

3.2.1 Problem Formulation

The motivation for formulating the proposed multistage decision-making model is elaborated on in Section 3.1.4. In the proposed framework, one important thing is to identify a proper predictive model for every stage as the building block. The basic requirement of the predictive model is providing ordered outcomes: almost surely healthy ("0"), indeterminate("0.5"), and almost surely sick ("1"). Also, the predictive model should have good interpretability for doctors and patients who are not familiar with data science, and work stable with limited data size. After comparing the performance of different machine learning models, such as the popular neural networks, random forest, logistic regression, our

collaborator doctor prefers the logistic regression model, which gives a stable and pretty good performance, yet easy to interpret. Therefore, what to do next is building a generalized logistic regression model as building blocks for each stage.

In the proposed framework, general categorization is required to utilize the model. Patients must be stratified to: certainly healthy ("0"), indeterminate ("0.5"), and certainly sick ("1"). After comparing the performance of different machine learning models, including neural networks, random forest, logistic regression, we selected a logistic regression model, which provided stability and accuracy with easy interpretability. In the sections to follow, a generalized logistic regression model will be utilized as a building block for each stage.

Multiclass logistic regression, also called softmax/multinoulli/multinomial regression, is a classification method that generalizes logistic regression to multiclass problems, i.e. with more than two possible discrete outcomes ($K > 2$). The idea behind this classification model is one-vs-all or one-vs-rest, which means K binary classifier models will be trained to ensure every class has a binary classifier to identify whether a sample belongs to this specific class or not. This is similar to our scenario on the multiple-outcomes property. However, the above approach of modeling ignores the ordering of the categorical dependent variable. We are not trying to classify cats, dogs, and elephants, but classifying low-risk patients, medium-risk patients, and high-risk patients.

The ordinal logistic regression model, also called the ordered logit model or proportional odds model, overcomes this limitation by calculating the log of the odds of cumulative events [47, 48, 49]. Unlike simple logistic regression, ordinal logistic models consider the probability of an event and all the events that are below the focal event in the ordered hierarchy. Ordinal logistic regression assumes that the coefficients that describe the relationship between, say, the lowest versus all higher categories of the response variable are the same as those that describe the relationship between the next lowest category and all higher categories, etc. It assumes different intercepts θ_j for different categories. The sequence of θ_j can also be interpreted as cutoff points on a continuous variable Y^*, the

linear combination of explanatory variables, in the latent variable explanation. This model seems to be a promising candidate for our case. However, the existing ordinal logistic regression only deals with a single model which can only be a sub-model of our multistage sequential decision-making model. Therefore, in this research, we'll develop our own multistage model with the existing ordinal logistic regression model as a building block for each stage, but estimate the parameters in all stages together. The contribution of our work is twofold. In terms of statistical analysis, an active learning model is proposed in a multistage decision-making process. This learning algorithm can interactively query a patient to collect additional clinical data for collecting necessary information [50]. Also, the proposed model introduces a novel way of dealing with incomplete data by allowing some data to be absent and modeling with incomplete but necessary data directly, rather than guessing the incomplete data with uncertainty. To apply this model in a clinical setting, a general strategy is developed to making diagnostic decisions and treatment recommendations sequentially when some laboratory data are more expensive, invasive, or time-consuming to collect than other data. By recommending only requisite testing to those patients in whom symptoms do not support a definitive diagnosis, the proposed process is fast, cost-effective, yet reliable.

3.2.2 Model Framework

The proposed multistage sequential decision-making model is shown in Figure 3.3.

To achieve the goal of optimizing the diagnosis process for doctors, this framework recommends the following procedure:

First, group all possible patients' features into K categories according to their characteristics, such that each category of features corresponds to one stage. The earlier stages should involve features that are patient-friendly, costless, but properly less informative. And the latter stages should involve some cutting-edge technology, time-consuming, expensive, unwanted but more informative examinations. For example, in stage 1, the de-

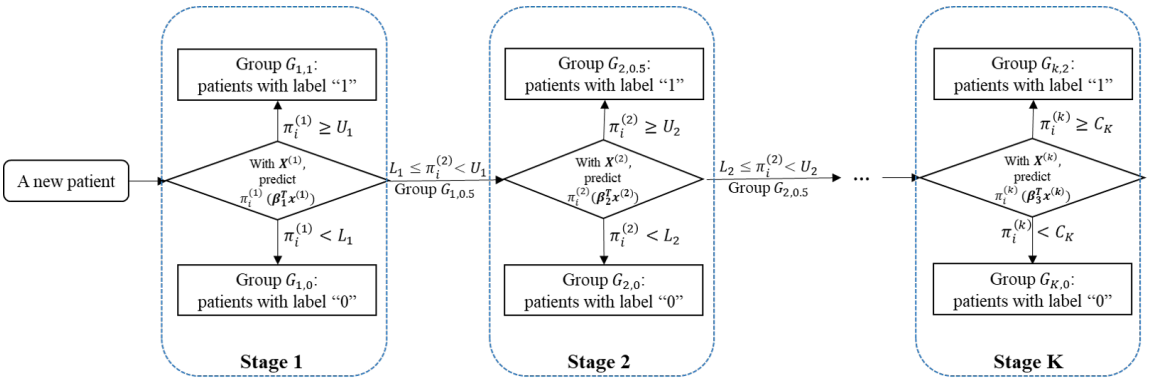

Figure 3.3: The framework of the proposed multistage sequential decision-making model, where K is the number of stages, $\pi_i^{(j)}$ is the probability of patient i having disease estimated by the predictive model in stage j, U_j and L_j is the cutoff points on the estimated probability in stage j, and C_K is the single cutoff point in the last stage.

mographic data of the patients are collected without any lab-test or imaging examinations. This may include the patient's characteristics such as age, gender, BMI, and family history of certain diseases. And in stage 2, for example, the lab-test data would be collected. The features in this stage are more informative but cost more time and money as well as patients' satisfaction. For example, blood or urine tests usually give more accurate and direct information about the status of a patient. And in later stages, imaging data can be involved, such as X-Ray imaging, computerized tomography (CT) scan, ultrasound (US) examination, Magnetic resonance imaging (MRI). These kinds of examinations may involve some potential side-effects, expensive, and special requirements such as staying still for a long time which may be hard for pediatric patients.

Then, at each stage, a predictive model is trained to estimate the probability of being sick according to the features in current and all former stages. The predictive models will quantify the probability of being sick via those currently available features which could be more objective and stable compared with the doctor's empirical estimation. If the patient i is apparently healthy (probability of sick $\pi_i^{(1)} < L_1$) or strongly suspected to be sick (probability of sick $\pi_i^{(1)} > U_1$), the model would label the patient as "0" or "1" respectively, and indicates the doctor to recommend the treatment choice confidently: suggest the patients

with label $'1'$ to accept treatment such as surgery, and patients with label $'0'$ to stop worrying, relax and go back home. For the rest of the patients whose probability of sick falls in between the cutoff points, they will be labeled as "0.5" and would be suggested to take more tests by going to the next stage. And for the last stage, as it is the last stage in the proposed model, no more technical choice available currently, the doctor has to make treatment recommendations anyway. Thus, in this stage, only one threshold, C_K, is designed to classify the patient as either healthy or sick.

Finally, for a new patient, the doctors can follow this framework with trained parameters to make diagnosis decisions and recommend treatments accordingly. In such a way, the features in different stages are collected sequentially, actively, and only when necessary.

One of the key elements in the proposed model is the cutoff criteria. Given cutoff criteria, the predictive model will filter the patients into three groups, or two in the final stage,until all patients have been decided, or all possible examinations have been done in the final stage. And in the proposed model, the cutoff points are not prescribed but parameters to be optimized.

Another key element is the predictive model in each stage. In the proposed multistage model, ordinal logistic regression is adopted as the basic predictive model in each stage. What's special is, the patients' groups in the different stages have a nested structure rather than independent. What's more, the features in the current stage k includes all the features in former stages and newly added features in category k. Since the data in different stages are nested, it inspires us to consider the predictive models in different stages together rather than isolatedly. And the details here will be discussed in the parameter estimation part in Section 3.3.

In what follows, we'll use the simplest example, a 2-stage decision-making model, to illustrate the proposed active learning style multistage sequential decision-making model.

3.2.3 Data Organization for 2-stage Model as Example

As discussed earlier, the features can be divided into several categories, each corresponds to a certain stage in our multistage model. The criteria for feature grouping are flexible which can be adjusted according to real scenarios case-by-case. Basically, we recommend the following principles for reference:

1. For the features inside a category, the cost of collection and the information contained should be similar. For example, all indices can be obtained from one examination such as a blood test.

2. For different feature categories, the should be a gap between the expense and information contained.

3. Make sure each category contains some useful information, and avoid too many categories. For example, there's no need to split each variable into one category, especially less informative variables, such as gender, age, race, etc.

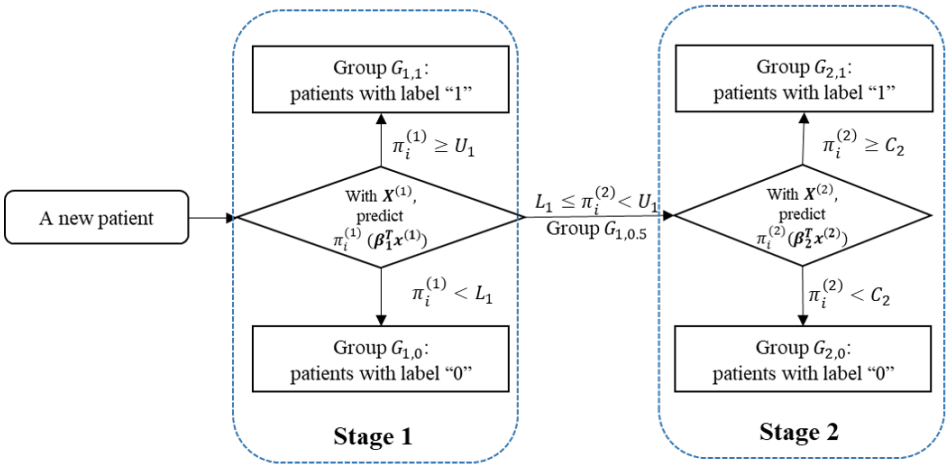

Figure 3.4: A simple 2-stage sequential decision-making model.

To illustrate the data organization for the proposed model, without loss of generality, we take the simplest case, a 2-stage sequential decision-making model in Figure 3.4, as an example as follows.

- Stage 1: $\left\{y_i^{(1)}; x_{i,1}^{(1)}, x_{i,2}^{(1)}, \ldots, x_{i,p_1}^{(1)}\right\} = \left\{\boldsymbol{y}^{(1)}; \boldsymbol{X}^{(1)}\right\}, i = 1, 2, \ldots, N_1,$
  $y_i^{(1)} \in \{\text{“0”}, \text{“0.5”}, \text{“1”}\};$
- Stage 2: $\left\{y_i^{(2)}; x_{i,1}^{(1)}, x_{i,2}^{(1)}, \ldots, x_{i,p_1}^{(1)}; x_{i,1}^{(2)}, x_{i,2}^{(2)}, \ldots, x_{i,p_2}^{(2)}\right\} = \left\{\boldsymbol{y}^{(2)}; \boldsymbol{X}^{(2)}\right\}, i = 1, 2, \ldots,$
  $N_2, y_i^{(2)} \in \{\text{“0”}, \text{“1”}\};$

Here, the superscripts (1) and (2) denote the stage 1, p_1 and p_2 are the number of features collected in category 1 and category 2, respectively. The number of patients labeled in the 2 stages are N_1 and N_2, respectively. Note that, the feature set for stage 2, $\boldsymbol{X}^{(2)}$ contains the feature set for stage 1, $\boldsymbol{X}^{(1)}$, i.e. $\boldsymbol{X}^{(1)} \in \boldsymbol{X}^{(2)}$, and the number of features in stage 2 is actually $p_1 + p_2$. In other words, the data in the 2 groups have a nested structure rather than statistically independent.

3.2.4 Our Proposed Model vs. Existing Ordinal Logistic Regression

In our multistage decision-making model, the building block in each stage is essentially an ordinal logistic regression model. As aforementioned, the existing logistic regression in each stage can satisfy our needs of giving ordered multiclass outputs, which can serve as a filter in each stage to split patients into 3 groups based on the ordered probability of being sick: almost surely healthy, almost surely sick, or indeterminate and better to the next stage to take more examinations.

Ordinal logistic regression can be seen as a form of a generalized linear model (GLM) similar to the logistic regression. In logistic regression, the response variable Y_i has a logistic distribution (or normal or extreme-value or Cauchy distribution with scale parameter one) and a linear model for the mean: $\operatorname{logit} \mathcal{E}(Y) = \boldsymbol{\beta}^\top \boldsymbol{x}$. In ordinal logistic regression, the response variable Y_i will fall into several ordinal categories with proper estimated cutoff points. Instead of finding the cutoff points that work directly on Y_i, people find the cutoff points on the linear predictor Y_i^* instead for convenience:

$$Y_i^* = \boldsymbol{\beta}^\top \boldsymbol{x}_i + \boldsymbol{\varepsilon}_i \tag{3.1}$$

Here the Y_i^* is regarded as an underlying continuous latent variable such that it would be the response variable in an ordinary linear model [51]. And ε_i is the error term.

Therefore, in the proposed 2-stage sequential decision-making model, we'll have the following expression for the sub-models in the two stages, respectively:

$$Y_i^{(1)} = \begin{cases} 0, & \text{if } Y_i^{(1)*} < L_1^* \\ 0.5, & \text{if } L_1^* \leq Y_i^{(1)*} < U_1^* \\ 1, & \text{if } Y_i^{(1)*} \geq U_1^* \end{cases}, \quad Y_i^{(2)} = \begin{cases} 0, & \text{if } Y_i^{(2)*} < C_2^* \\ 1, & \text{if } Y_i^{(2)*} \geq C_2^* \end{cases} \tag{3.2}$$

Note that here the cutoff points $\{L_1^*, U_1^*, C_2^*\}$ applying on the latent variable Y^* is not the cutoff points $\{L_1, U_1, C_2\}$ applying on the probability estimation π_i in the Figure 2.4. Instead, the former set needs to go through a link function projection to get the latter.

Recall that in our multistage model, the output $Y_i \in \{\text{“0”}, \text{“0.5”}, \text{“1”}\}$ represents “labeled as healthy”, “unclear, go to next stage”, and “labeled as sick”, respectively. And for the last stage, $Y_i \in \{\text{“0”}, \text{“1”}\}$ indicates “labeled as healthy” and “labeled as sick” similarly. And the outputs are ordered, i.e. $Y_i \leq Y_{i+1}$. Thus, if we look at the sub-models in each stage individually, it is a special case of the existing ordinal logistic regression model with the latent variable interpretation. However, in the proposed multistage sequential decision-making model Equation 3.2, $Y_i^{(1)*} = \boldsymbol{\beta}^{(1)\top}\boldsymbol{x}_i^{(1)}$ and $Y_i^{(2)*} = \boldsymbol{\beta}^{(2)\top}\boldsymbol{x}_i^{(2)}$. Recall that $\boldsymbol{X}^{(1)} \in \boldsymbol{X}^{(2)}$, the data in different stages have a nested structure rather than independent, which makes the existing ordinal logistic regression problematic. In what follows, we'll start with existing ordinal logistic regression, and develop our proposed model based on it.

Existing Ordinal Logistic Regression Model

The scenario in the ordinal logistic model is a categorical variable Y with ordered outcomes $1, 2, ..., J$ and predictors $\boldsymbol{X} = X_1, X_2, ..., X_p$. In the latent variable interpretation, it is assumed that there is a real-valued latent variable Y^*, same to Equation 3.1. Suppose that

the manifest response Y results from grouping the underlying variable Y^* using cutoff points $\theta_1 < \theta_2 < \ldots < \theta_{J-1}$, so that:

$$Y = \begin{cases} 1, \text{ if } y^* \leq \theta_1 \\ 2, \text{ if } \theta_1 < y^* \leq \theta_2 \\ 3, \text{ if } \theta_2 < y^* \leq \theta_3 \\ \vdots \\ J, \text{ if } \theta_{J-1} < y^* \end{cases} \tag{3.3}$$

Defining $\theta_0 = -\infty$ and $\theta_J = \infty$, then, the above model Equation 3.3 will lead to the following conclusion:

$$y = j \iff \theta_{j-1} < y^* \leq \theta_j$$

From these assumptions, we can derive the conditional distribution of y as

$$\begin{aligned} P(y = j \mid \boldsymbol{x}) &= P\left(\theta_{j-1} < y^* \leq \theta_j \mid \boldsymbol{x}\right) \\ &= P\left(\theta_{j-1} < \boldsymbol{\beta}^\top \boldsymbol{x} + \varepsilon \leq \theta_j\right) \\ &= F\left(\theta_j - \boldsymbol{\beta}^\top \boldsymbol{x}\right) - F\left(\theta_{j-1} - \boldsymbol{\beta}^\top \boldsymbol{x}\right) \end{aligned} \tag{3.4}$$

where $\boldsymbol{\beta}, \theta_j$ are model coefficients and cutoff points to be estimated from the data, P is the abbreviation of probability, and F is the cumulative distribution function (CDF) of the error term $\boldsymbol{\varepsilon}$, and takes on the role of the inverse link function.

Note that the error term $\boldsymbol{\varepsilon}$ in Equation 3.1 may have various distributions, such as logistic or probit or complementary log-log or Cauchit (corresponding to a Cauchy latent variable). Especially, for a probit version model, we have $\varepsilon \sim N(0, 1)$, and for logit version of model, we have $\varepsilon \sim Logistic(0, 1)$. When we assume that the error term ϵ follows the standard logistic distribution, the model can be called ordinal logistic regression, ordered logit model, or proportional odds model. In what follows we'll focus on the ordinal

logistic regression. This means we'll have

$$F(t) = \frac{1}{1 + e^{-t}}$$

Naturally, we have the following expression:

$$P\left(Y \leq j\right) = P(\varepsilon \leq \theta_j - \boldsymbol{\beta}^\top \boldsymbol{X}) = F\left(\theta_j - \boldsymbol{\beta}^\top X\right) = \frac{1}{1 + e^{\left(\boldsymbol{\beta}^\top X - \theta_j\right)}}$$

Cumulative Link Model and Proportional Odds Model

The above expression coincides well with the proportional odds model explanation. To understand the proportional odds model, one should first review the cumulative link model (CLM) because the proportional odds model is a member of a wider family of models called cumulative link models [52]. To use category ordering, it models the cumulative probabilities like follows:

$$P(Y \leq j \mid \boldsymbol{x}) = \pi_1(\boldsymbol{x}) + \cdots + \pi_j(\boldsymbol{x}), \quad j = 1, \ldots, j, \ldots, J. \tag{3.5}$$

where $\pi_j = P(y_i = j|\boldsymbol{x}_i)$ and $\sum_{j=1}^{J} \pi_{ij} = 1$.

Naturally, a *cumulative logits* are defined as [52]:

$$\begin{aligned} \text{logit}[P(Y \leq j \mid \boldsymbol{x})] &= \log \frac{P(Y \leq j \mid \boldsymbol{x})}{1 - P(Y \leq j \mid \boldsymbol{x})} \\ &= \log \frac{\pi_1(\boldsymbol{x}) + \cdots + \pi_j(\boldsymbol{x})}{\pi_{j+1}(\boldsymbol{x}) + \cdots + \pi_J(\boldsymbol{x})}, \quad j = 1, \ldots, J-1 \end{aligned}$$

The relationship between cumulative link model and proportional odds model is as follows: a model for $logit[P(Y \leq j)]$ along is an ordinary logit model for a binary response—categories $\{1, ..., j\}$ vs. categories $\{j + 1, ..., J\}$. A model that simultaneously

uses all cumulative logits called the proportional odds model, which can be represented as

$$\text{logit}[P(Y \leq j \mid \boldsymbol{x})] = \theta_j + \boldsymbol{\beta}^\top \boldsymbol{x}, \quad j = 1, \ldots, J-1 \tag{3.6}$$

where θ_j is the intercept for the j^{th} cumulative logit model, and the sequence θ_j are increasing with j.

The definition of the proportional odds model can be explained by the Equation 3.7. If $\boldsymbol{x}_1$ and $\boldsymbol{x}_2$ are different data points, with the cumulative link model Equation 3.6 they satisfies

$$\begin{aligned} &\text{logit}\left[P\left(Y \leq j \mid \boldsymbol{x}_1\right)\right] - \text{logit}\left[P\left(Y \leq j \mid \boldsymbol{x}_2\right)\right] \\ =&\log \frac{P\left(Y \leq j \mid \boldsymbol{x}_1\right)/P\left(Y > j \mid \boldsymbol{x}_1\right)}{P\left(Y \leq j \mid \boldsymbol{x}_2\right)/P\left(Y > j \mid \boldsymbol{x}_2\right)} \\ =&\boldsymbol{\beta}^\top \left(\boldsymbol{x}_1 - \boldsymbol{x}_2\right) \end{aligned} \tag{3.7}$$

From Equation 3.7, it can be seen that the odds ratio of the event $y_i \leq j$ at $\boldsymbol{x}_1$ relative to the same event at $\boldsymbol{x}_2$, which is independent of j. Thus, the cumulative odds ratio is proportional to the distance between $\boldsymbol{x}_1$ and $\boldsymbol{x}_2$ which motivated McCullagh [47] to denote the cumulative logit model a proportional odds model. As the name suggests, the model only applies to data that meet the proportional odds assumption [47]. The proportional odds assumption is that the number added to each of these logarithms to get the next is the same in every case. In other words, these logarithms form an arithmetic sequence. The model states that the number in the last column of the table—the number of times that that logarithm must be added—is some linear combination of the other observed variables. Thus, the proportional odds model is identical to the linear logistic model [48]:

$$\text{logit}(P(Y \leq j)) = \log \frac{P(Y \leq j)}{1 - P(Y \leq j)} = \log \frac{P(Y \leq j)}{P(Y > j)} = \theta_j - (\beta_1 X_1 + \cdots + \beta_p X_p)$$

The logistic function is the inverse of the logit-function, so the predicted probabilities

$\hat{P}(Y \leq j)$ are

$$\hat{P}(Y \leq j) = \frac{e^{\hat{\theta}_j - \left(\hat{\beta}_1 X_1 + \cdots + \hat{\beta}_p X_p\right)}}{1 + e^{\hat{\theta}_j - \left(\hat{\beta}_1 X_1 + \cdots + \hat{\beta}_p X_p\right)}}$$

Naturally, the predicted probability for each class is

$$\hat{P}(Y = j) = \hat{P}(Y \leq j) - \hat{P}(Y \leq j - 1) \tag{3.8}$$

Clearly, we can seen that Equation 3.8 is equivalent to Equation 3.4.

Then, given a new observation $\boldsymbol{x}_{new}$, the probability that it belongs to each category, $[\pi_1(\boldsymbol{x}_{new}), \pi_2(\boldsymbol{x}_{new}), ..., \pi_J(\boldsymbol{x}_{new})]$, can be calculated respectively. And the maximum probability indicate the most likely class that $\boldsymbol{x}_{new}$) belongs to.

3.3 Parameter Estimation

There is a couple of ways to estimate parameters in the model (Equation 3.2). The first one is the baseline approach that estimating the parameters in two stages separately by assuming the $\boldsymbol{\beta}^{(1)}$ and $\boldsymbol{\beta}^{(2)}$ are independent without considering the nested structure and potential correlations between the two adjacent stages. That is, conduct the ordinal logistic regression model for each stage independently with existing software packages.

The second method of parameter estimation is to assume that $\boldsymbol{\beta}^{(1)}$ and $\boldsymbol{\beta}^{(2)}$ share some common parts. Recall that the feature data in the current stage contains the feature in all former stages, e.g:

$$\boldsymbol{X}^{(2)} = \left\{x_{i,1}^{(1)}, x_{i,2}^{(1)}, \ldots, x_{i,p_1}^{(1)}; x_{i,1}^{(2)}, x_{i,2}^{(2)}, \ldots, x_{i,p_2}^{(2)}\right\} = \left\{\boldsymbol{X}^{(1)}; x_{i,1}^{(2)}, x_{i,2}^{(2)}, \ldots, x_{i,p_2}^{(2)}\right\}$$

In other words, the feature in every stage is actually the "cumulative available features". Such property of data inspires us to make the following assumption: the model coefficients

should have consistent common parts correspondingly, e.g

$$\boldsymbol{\beta}^{(2)} = \left\{\beta_1^{(1)}, \beta_2^{(1)}, \ldots, \beta_{p_1}^{(1)}; \beta_1^{(2)}, \beta_2^{(2)}, \ldots, \beta_{p_2}^{(2)}\right\} = \left\{\boldsymbol{\beta}^{(1)}; \beta_1^{(2)}, \beta_2^{(2)}, \ldots, \beta_{p_2}^{(2)}\right\}$$

Under such assumption, $\boldsymbol{\beta}^{(1)} \in \boldsymbol{\beta}^{(2)}$.

One significant advantage of such an assumption is saving the computational cost. In the baseline approach, the total number of parameters in $\boldsymbol{\zeta}$ to be estimated is $(p_1+p_2+p_K)+2(K-1)+1$ for a K-stage model, and people have to conduct a ordinal logistic regression for each stage, totally K times. While in the second method with the common coefficients assumption, the total number of parameters to be estimated is only $p_K + 2(K-1)+1$, and all these parameters can be estimated in one time.

Another significant advantage of such an assumption is reducing the variance of parameter estimation. In the baseline approach, single models are trained on the subgroup of observations in that stage without making use of the observations stopping at former stages. In this case, the observations in every stage reduce significantly stage by stage. But in the proposed model, the parameters for every stage are estimated together simultaneously with all observations involved, which should make the parameter estimation more stable.

Therefore, in what follows, we'll focus on the parameter estimation for the proposed model with common coefficients assumption. Along the direction of MLE, the unknown parameters can be denoted as $\boldsymbol{\zeta}$:

$$\boldsymbol{\zeta} = \left\{\boldsymbol{\beta}^{(2)}, \theta_1^{(1)}, \theta_2^{(1)}, \theta_1^{(2)}\right\}$$

where $\{L_1^*, U_1^*, C_2^*\}$ in the proposed 2-stage model is actually equivalent to $\left\{\theta_1^{(1)}, \theta_2^{(1)}; \theta_1^{(2)}\right\}$ in the exited ordinal logistic regression formulation. and all the unknown parameters included in $\boldsymbol{\zeta}$ will be estimated jointly.

3.3.1 Joint Likelihood of Proposed Model with Common Coefficients Assumption

To estimate the parameters $\boldsymbol{\zeta}$ in the proposed model, the probability modeling style inspires the adoption of MLE. Similarly, we start with the existing ordinal logistic regression. The log-likelihood of the proportional odds model for a single training example $\boldsymbol{x}_i, y_i$ can be stated as

$$\log \mathcal{L}\left(\boldsymbol{\beta}, \boldsymbol{\theta} \mid \boldsymbol{x}_i, y_i\right) = \sum_{j=1}^{J} I(y_i = j) \log \left[F\left(\theta_j - \boldsymbol{\beta}^\top \boldsymbol{x}_i\right) - F\left(\theta_{j-1} - \boldsymbol{\beta}^\top \boldsymbol{x}_i\right)\right] \quad (3.9)$$

where $I(y_i = j)$ is the indicator function, $\theta_0 = -\infty$ and $\theta_J = \infty$, and θ_j is the cutoff points on Y^* between the j^{th} and $j + 1^{th}$ category.

Obviously, the joint log-likelihood function for all samples would be the summation of the single sample likelihood:

$$\log \mathcal{L}\left(\boldsymbol{\beta}, \boldsymbol{\theta} \mid \boldsymbol{X}, Y\right) = \sum_{i=1}^{N} \sum_{j=1}^{J} I(y_i = j) \log \left[F\left(\theta_j - \boldsymbol{\beta}^\top \boldsymbol{x}_i\right) - F\left(\theta_{j-1} - \boldsymbol{\beta}^\top \boldsymbol{x}_i\right)\right]$$

The parameter estimation for the existing ordinal logistic regression has been well studied since the log-likelihood objective function owns a lot of proved nice properties. McCullagh presented a Fisher scoring algorithm for ML estimation, expressing the likelihood in the form Equation 3.9 using cumulative probabilities. McCullagh showed that sufficiently large n guarantees a unique maximum of the likelihood [47, 52]. Burridge and Pratt showed that the log-likelihood is concave for many cumulative link models, including the logit, probit, and complementary log-log [52]. Iterative algorithms usually converge rapidly to the ML estimates. The optimization computing algorithms are developed based on these nice properties. The existing approaches compute the maximum-likelihood estimates by iteratively reweighted least squares (IRLS). And actually, in R software, all GLM are fit using IRLS estimation method for the log-likelihood. IRLS is used to find the MLE of a GLM and find an M-estimator in robust regression, as a way of mitigating the influence of

outliers in an otherwise normally distributed data set.

Developed upon the existing ordinal logistic regression model, our proposed model involves two significant novelties. Firstly, our target is to estimate all the parameters $\boldsymbol{\zeta}$ in all stages jointly, while the existing ordinal logistic regression model only deals with the individual model in each stage independently. Meanwhile, building ordinal logistic models independently for each stage sequentially will be adopted as a baseline approach for comparison. Secondly, as we discussed earlier, we expect the coefficients have consistent common parts in a cumulative way. Thus, for our proposed multistage model, the joint likelihood function for all samples in all stages would be like follows:

$$\ell(\boldsymbol{\zeta}) = \sum_{k=1}^{K} \sum_{i=1}^{N_k} \sum_{j=1}^{J_k} I(y_i^{(k)} = j) \log \left[F\left(\theta_j^{(k)} - \boldsymbol{\beta}^{(k)\top} \boldsymbol{x}_i^{(k)}\right) - F\left(\theta_{j-1}^{(k)} - \boldsymbol{\beta}^{(k)\top} \boldsymbol{x}_i^{(k)}\right) \right]$$

where $\log \mathcal{L}\left(\boldsymbol{\zeta} \mid \boldsymbol{X}, Y\right)$ is rewritten as $\ell(\boldsymbol{\zeta})$ for simplicity, K is the number of stages in the proposed multistage sequential decision-making model, N_k is the total number of patients/observations in the k^{th} stage, and J_k is the number of categories in the k^{th} stage for which we have

$$J_k = \begin{cases} 3, \text{ if } 1 \leq k < K \\ 2, \text{ if } k = K \end{cases}$$

Given the joint likelihood function for all stages, the next step is to estimate all the parameters $\boldsymbol{\zeta}$ simultaneously. For the MLE algorithm, the key is to find the gradient of the likelihood function. We can find the gradient for each parameter individually as follows:

$$\frac{\partial \ell(\boldsymbol{\zeta})}{\partial \boldsymbol{\beta}^{(k)}} = \sum_{i=1}^{N_k} \sum_{j=1}^{J_k} I(y_i^{(k)} = j) \frac{(-\boldsymbol{x}_i^{(k)}) \left[f\left(\theta_j^{(k)} - \boldsymbol{\beta}^{(k)\top} \boldsymbol{x}_i^{(k)}\right) - f\left(\theta_{j-1}^{(k)} - \boldsymbol{\beta}^{(k)\top} \boldsymbol{x}_i^{(k)}\right) \right]}{F\left(\theta_j^{(k)} - \boldsymbol{\beta}^{(k)\top} \boldsymbol{x}_i^{(k)}\right) - F\left(\theta_{j-1}^{(k)} - \boldsymbol{\beta}^{(k)\top} \boldsymbol{x}_i^{(k)}\right)}$$

$$\frac{\partial \ell(\boldsymbol{\zeta})}{\partial \theta_j^{(k)}} = \sum_{i=1}^{N_k} \sum_{j=1}^{J_k} I(y_i^{(k)} = j) \{ \frac{f\left(\theta_j^{(k)} - \boldsymbol{\beta}^{(k)\top} \boldsymbol{x}_i^{(k)}\right)}{F\left(\theta_j^{(k)} - \boldsymbol{\beta}^{(k)\top} \boldsymbol{x}_i^{(k)}\right) - F\left(\theta_{j-1}^{(k)} - \boldsymbol{\beta}^{(k)\top} \boldsymbol{x}_i^{(k)}\right)} - \frac{f\left(\theta_j^{(k)} - \boldsymbol{\beta}^{(k)\top} \boldsymbol{x}_i^{(k)}\right)}{F\left(\theta_{j+1}^{(k)} - \boldsymbol{\beta}^{(k)\top} \boldsymbol{x}_i^{(k)}\right) - F\left(\theta_j^{(k)} - \boldsymbol{\beta}^{(k)\top} \boldsymbol{x}_i^{(k)}\right)} \}$$

Recall that F is the CDF of the error term $\varepsilon \sim Logistic(0, 1)$, and $f(t) = F'(t)$ is the probability density function (PDF) of $\boldsymbol{\varepsilon}$:

$$F(t; 0, 1) = \frac{1}{1 + e^{-t}}, \quad f(t; 0, 1) = \frac{1}{(e^{t/2} + e^{-t/2})^2}$$

Note that the coefficient in stage k, $\boldsymbol{\beta}^{(k)}$, contains $\boldsymbol{\beta}^{(k-1)}$ and newly added coefficients for features in the k^{th} stage, which makes the coefficients in different stages of different length. To deal with this issue, we propose to find the gradient in each stage $\frac{\partial \ell(\boldsymbol{\zeta})}{\partial \boldsymbol{\beta}^{(k)}}$ individually first. And then, add them together with the front ends aligned, and pad the shorter ends with 0's:

$$\frac{\partial \ell(\boldsymbol{\zeta})}{\partial \boldsymbol{\beta}} = \left[\frac{\partial \ell(\boldsymbol{\zeta})}{\partial \boldsymbol{\beta}^{(1)}}; 0, 0, ..., 0\right] + ... + \left[\frac{\partial \ell(\boldsymbol{\zeta})}{\partial \boldsymbol{\beta}^{(K)}}\right]$$

In computation, the indicator function $I(y_i^{(j)} = j)$ can be replace with a mask matrix with boolean values. Also, the indicator function can be avoided data preprocessing in the training process. For example, people can split the patients into different groups to mark the identity, use $G_{k,j}$ to denote the group of patients who have label j in stage k. Take our 2-stage illustrating case as an example, the log-likelihood function can be written as:

$$\begin{aligned} \ell(\boldsymbol{\zeta}) = & \sum_{i, n_i \in G_{1,1}} \log\left\{1 - F\left(U_1^* - \boldsymbol{\beta}^{(1)^\top} \boldsymbol{x}_i^{(1)}\right)\right\} + \sum_{i, n_i \in G_{1,0}} \log F\left(L_1^* - \boldsymbol{\beta}^{(1)^\top} \boldsymbol{x}_i^{(1)}\right) + \\ & \sum_{i, n_i \in G_{1,0.5}} \log\left\{F\left(U_1^* - \boldsymbol{\beta}^{(1)\top} \boldsymbol{x}_i^{(1)}\right) - F\left(L_1^* - \boldsymbol{\beta}^{(1)\top} \boldsymbol{x}_i^{(1)}\right)\right\} + \\ & \sum_{i, n_i \in G_{2,1}} \log\left\{1 - F\left(C_2^* - \boldsymbol{\beta}^{(2)\top} \boldsymbol{x}_i^{(2)}\right)\right\} + \sum_{i, n_i \in G_{2,0}} \log F\left(C_2^* - \boldsymbol{\beta}^{(2)\top} \boldsymbol{x}_i^{(2)}\right) \end{aligned} \tag{3.10}$$

Since here $\boldsymbol{\beta}^{(2)} = \left\{\boldsymbol{\beta}^{(1)}, \beta_1; \beta_2, ..., \beta_{p_2}\right\}$, to avoid any potential confusing notation, we rewrite them as:

$$\boldsymbol{\beta}^{(1)} = \{\alpha_1, ..., \alpha_m, ..., \alpha_{p1}\}, \quad \boldsymbol{\beta}^{(2)} = \{\alpha_1, ..., \alpha_m, ..., \alpha_{p1}; \beta_1, ..., \beta_m, ..., \beta_{p_2}\}$$

$$\boldsymbol{\zeta} = \{\alpha_1, ..., \alpha_m, ..., \alpha_{p1}; \beta_1, ..., \beta_m, ..., \beta_{p_2}; \quad L_1^*, U_1^*, C_2^*\}$$

Given the joint log-likelihood function, we can write the derivative for each coefficient in $\boldsymbol{\zeta}$ individually accordingly.

For the common coefficients, α_m for $m = 1, ..., p_1$, we have:

$$\begin{aligned}\frac{\partial \ell(\boldsymbol{\zeta})}{\partial \alpha_m} = &\sum_{i,\forall n_i \in G_{1,1}} \frac{x_{i,m}^{(1)} f\left(U_1^* - \boldsymbol{\beta}^{(1)\top}\boldsymbol{x}_i^{(1)}\right)}{1 - F\left(U_1^* - \boldsymbol{\beta}^{(1)\top}\boldsymbol{x}_i^{(1)}\right)} + \sum_{i,\forall n_i \in G_{1,0}} \frac{-x_{i,m}^{(1)} f\left(L_1^* - \boldsymbol{\beta}^{(1)\top}\boldsymbol{x}_i^{(1)}\right)}{F\left(L_1^* - \boldsymbol{\beta}^{(1)\top}\boldsymbol{x}_i^{(1)}\right)} + \\ &\sum_{i,\forall n_i \in G_{1,0.5}} \frac{-x_{i,m}^{(1)}\left[f\left(U_1^* - \boldsymbol{\beta}^{(1)\top}\boldsymbol{x}_i^{(1)}\right) - f\left(L_1^* - \boldsymbol{\beta}^{(1)\top}\boldsymbol{x}_i^{(1)}\right)\right]}{F\left(U_1^* - \boldsymbol{\beta}^{(1)\top}\boldsymbol{x}_i^{(1)}\right) - F\left(L_1^* - \boldsymbol{\beta}^{(1)\top}\boldsymbol{x}_i^{(1)}\right)} + \\ &\sum_{i,\forall n_i \in G_{2,1}} \frac{x_{i,m}^{(2)} f\left(C_2^* - \boldsymbol{\beta}^{(2)\top}\boldsymbol{x}_i^{(2)}\right)}{1 - F\left(C_2^* - \boldsymbol{\beta}^{(2)\top}\boldsymbol{x}_i^{(2)}\right)} + \sum_{i,\forall n_i \in G_{2,0}} \frac{x_{i,m}^{(2)} f\left(C_2^* - \boldsymbol{\beta}^{(2)\top}\boldsymbol{x}_i^{(2)}\right)}{F\left(C_2^* - \boldsymbol{\beta}^{(2)\top}\boldsymbol{x}_i^{(2)}\right)}\end{aligned} \tag{3.11}$$

For the coefficients for newly added features in stage 2, β_m for $m = 1, ..., p_2$, we have:

$$\frac{\partial \ell(\boldsymbol{\zeta})}{\partial \beta_m} = \sum_{i,\forall n_i \in G_{2,1}} \frac{x_{i,m}^{(2)} f\left(C_2^* - \boldsymbol{\beta}^{(2)\top}\boldsymbol{x}_i^{(2)}\right)}{1 - F\left(C_2^* - \boldsymbol{\beta}^{(2)\top}\boldsymbol{x}_i^{(2)}\right)} + \sum_{i,\forall n_i \in G_{2,0}} \frac{x_{i,m}^{(2)} f\left(C_2^* - \boldsymbol{\beta}^{(2)\top}\boldsymbol{x}_i^{(2)}\right)}{F\left(C_2^* - \boldsymbol{\beta}^{(2)\top}\boldsymbol{x}_i^{(2)}\right)} \tag{3.12}$$

For the cutoff points in all 2 stages, we have:

$$\frac{\partial \ell(\boldsymbol{\zeta})}{\partial U_1^*} = \sum_{i,\forall n_i \in G_{1,1}} \frac{-f\left(U_1^* - \boldsymbol{\beta}^{(1)\top}\boldsymbol{x}_i^{(1)}\right)}{1 - F\left(U_1^* - \boldsymbol{\beta}^{(1)\top}\boldsymbol{x}_i^{(1)}\right)} + \sum_{i,\forall n_i \in G_{1,0.5}} \frac{f\left(U_1^* - \boldsymbol{\beta}^{(1)\top}\boldsymbol{x}_i^{(1)}\right)}{F\left(U_1^* - \boldsymbol{\beta}^{(1)\top}\boldsymbol{x}_i^{(1)}\right) - F\left(L_1^* - \boldsymbol{\beta}^{(1)\top}\boldsymbol{x}_i^{(1)}\right)} \tag{3.13}$$

$$\frac{\partial \ell(\boldsymbol{\zeta})}{\partial L_1^*} = \sum_{i,\forall n_i \in G_{1,0}} \frac{f\left(L_1^* - \boldsymbol{\beta}^{(1)\top}\boldsymbol{x}_i^{(1)}\right)}{F\left(L_1^* - \boldsymbol{\beta}^{(1)\top}\boldsymbol{x}_i^{(1)}\right)} + \sum_{i,\forall n_i \in G_{1,0.5}} \frac{-f\left(L_1^* - \boldsymbol{\beta}^{(1)\top}\boldsymbol{x}_i^{(1)}\right)}{F\left(U_1^* - \boldsymbol{\beta}^{(1)\top}\boldsymbol{x}_i^{(1)}\right) - F\left(L_1^* - \boldsymbol{\beta}^{(1)\top}\boldsymbol{x}_i^{(1)}\right)} \tag{3.14}$$

$$\frac{\partial \ell(\boldsymbol{\zeta})}{\partial C_2^*} = \sum_{i,\forall n_i \in G_{2,1}} \frac{-f\left(C_2^* - \boldsymbol{\beta}^{(2)\top}\boldsymbol{x}_i^{(2)}\right)}{1 - F\left(C_2^* - \boldsymbol{\beta}^{(2)\top}\boldsymbol{x}_i^{(2)}\right)} + \sum_{i,\forall n_i \in G_{2,0.5}} \frac{f\left(C_2^* - \boldsymbol{\beta}^{(2)\top}\boldsymbol{x}_i^{(2)}\right)}{F\left(C_2^* - \boldsymbol{\beta}^{(2)\top}\boldsymbol{x}_i^{(2)}\right)} \tag{3.15}$$

3.3.2 Computation: $optim$ solver in R Software

There exist many well-developed software packages for implementing the existing ordinal logistic regression model [53]. In R software, several packages on CRAN implements CLMs. $polr$ from MASS [54] implements standard CLMs allowing for the 5 standard link functions but no further extensions; the VGAM package [55] includes CLMs via the $vglm$ function using the cumulative link. $vglm$ allows for several link functions as well as partial effects. The lrm and orm functions from the rms package [56] also implements CLMs with the 5 standard link functions but without scale effects, partial or structured thresholds. A Bayesian alternative is implemented in the $brms$ package [57] which includes structured thresholds in addition to random-effects.

In our joint-optimization problem, we'll follow the framework of the existing $polr()$ function in R software, and adopt the $optim()$ function as optimization solver with some modification to solve our specific joint optimization problem. The $polr()$ function in the package MASS in R software is popular for solving the ordinal logistic regression. In $polr()$, $optim()$ is adopted to solve the optimization problem. The $optim()$ is a function designed for general-purpose optimization based on Nelder–Mead, quasi-Newton and conjugate-gradient algorithms. It includes an option for box-constrained optimization and simulated annealing.

When using the $optim()$ solver, it's important to specify the input parameters properly. One is the objective function f_n to be minimized (or maximized), and the other is a function g_n to return the gradient for the "BFGS", or "CG", or "L-BFGS-B" methods. In our 2-stage example case, obviously, the parameter to be optimized over is $\boldsymbol{\zeta}$, the objective function to be minimized f_n is the negative joint log-likelihood function Equation 3.10, and the gradient function g_n would be the combination of the gradients, Equation 3.11, Equation 3.12, Equation 3.14, Equation 3.13, and Equation 3.15:

$$g_n = \left[\frac{\partial \ell(\boldsymbol{\zeta})}{\partial \alpha_1}, ..., \frac{\partial \ell(\boldsymbol{\zeta})}{\partial \alpha_{p_1}}; \quad \frac{\partial \ell(\boldsymbol{\zeta})}{\partial \beta_1}, ..., \frac{\partial \ell(\boldsymbol{\zeta})}{\partial \beta_{p_2}}; \quad \frac{\partial \ell(\boldsymbol{\zeta})}{\partial L_1^*}, \frac{\partial \ell(\boldsymbol{\zeta})}{\partial U_1^*}, \frac{\partial \ell(\boldsymbol{\zeta})}{\partial C_2^*}\right]$$

Similar to the existing $polr()$ function, we choose the "BFGS" method here for solving the optimization problem. "BFGS" is the abbreviation for Broyden–Fletcher–Goldfarb–Shanno algorithm, an iterative method for solving unconstrained nonlinear optimization problems [58]. It is a quasi-Newton method (also known as a variable metric algorithm), specifically that published simultaneously in 1970 by Broyden et. al. [59]. It uses function values and gradients to build up a picture of the surface to be optimized. It updates an approximation to the inverse Hessian using the "BFGS" update formulas, along with an acceptable point line search strategy. This method appears to work best with analytic gradients according to the documentation.

Another important input for this $optim()$ solver is variable initialization. It is nontrivial to find a proper start location for the parameter set $\boldsymbol{\zeta}_0$ since a bad initial value may force the result trapped in the local optimum due to the nature of $polr()$ function. To find a reasonable initial location, in the existing ordinal logistic regression, the K categories are reclassified into 2 categories with a single cutoff point in the middle, and then a regular logistic regression is used to estimate the coefficients $\boldsymbol{\beta}$ which will serve as the initial value of $\boldsymbol{\beta}$. And in the proposed model with common coefficients assumption, the initial value would be set as the mean vector of the coefficients estimated from the independent single-stage ordinal logistic regression model.

In the next section, a simulation study is conducted to illustrate the proposed multistage sequential decision-making model with common coefficients assumption. The performance of the proposed model is then compared with that of the baseline approach where the stages are treated individually with an existing ordinal logistic regression model.

3.4 Simulation Study

In this section, a simulation is conducted to verify the effectiveness and simplicity of the proposed methodology. First, the dataset, $\{X^{(1)}, Y^{(1)}; X^{(2)}, Y^{(2)}\}$ is generated with prescribed coefficient $\boldsymbol{\beta}^{(1)}, \boldsymbol{\beta}^{(2)}$ and classification threshold $\{L_1^*, U_1^*, C_2^*\}$. With the dataset

and model parameters as ground truth, we first conduct a baseline approach. In the baseline approach, we use the existing ordinal logistic regression package and train 2 classifiers independently for each stage. Then, we implement the proposed 2-stage algorithm with common coefficients assumption and estimate the parameters in all 2 stages $\boldsymbol{\zeta}$ simultaneously. Finally, we'll compare the performance of the baseline model and proposed model in the aspect of the prediction performance, stability, model interpretability, and simplicity.

3.4.1 Synthetic Data Generation

Let $N_1 = 10,000$ denotes the total number of synthetic patients at the beginning.

Feature Set Generation – $\boldsymbol{X^{(1)}}$ *and* $\boldsymbol{X^{(2)}}$

We design the features of patients as follows:

- $X_1 \sim Bernoulli(0.3)$
- $X_2 \sim N(-1, 1)$
- $X_3 \sim N(1, 1)$
- $X_4 \sim N(0, 2)$
- $X_5 \sim Bernoulli(0.4)$
- $X_6 \sim N(-1, 1)$
- $X_7 \sim N(0, 1)$

For stage 1, we assume the category 1 includes the first 4 features: $\boldsymbol{X}^{(1)} = \{X_1, X_2, X_3, X_4\}$. Then, for stage 2, 3 new feature in category 2 are added and the cumulative features for stage 2 are:

$$\boldsymbol{X}^{(2)} = \{X_1, X_2, X_3, X_4; X_5, X_6, X_7\} = \left\{\boldsymbol{X}^{(1)}; X_6, X_7, X_8\right\}$$

Noise Term Generation – $\boldsymbol{\varepsilon^{(1)}}$ and $\boldsymbol{\varepsilon^{(2)}}$

We designed the error term as follows:

$$\boldsymbol{\varepsilon^{(1)}} \sim Logistic(0,1), \quad \boldsymbol{\varepsilon^{(2)}} \sim Logistic(0,1)$$

where the first parameter in the logistic distribution is the location parameter and the second one is the scale parameter.

In the proposed model, the error term $\boldsymbol{\varepsilon}$ follows standard logistic regression for both stages. Note that if the error term $\boldsymbol{\varepsilon}$ follows logistic regression with other parameters, such as $\boldsymbol{\varepsilon^{(1)}} \sim Logistic(0, 0.1)$, the estimation of $\boldsymbol{\beta}$ and $\boldsymbol{\theta}$ will be scaled according to the inherent model assumption in the probability style formation. For example, in Equation 3.2, if the scale of $\boldsymbol{\varepsilon}$ is not fixed to "1", the number of solution for $\boldsymbol{\beta}$ and $\{L_1^*, U_1^*, C_2^*\}$ would be infinite as the the optimal solution is on a hyperplane rather than a point.

Weights Generation – $\boldsymbol{\beta^{(1)}}$ and $\boldsymbol{\beta^{(2)}}$

The coefficient/weight is designed as:

$$\boldsymbol{\beta}^{(1)} = [2, 2, 2, 2]$$

$$\boldsymbol{\beta}^{(2)} = [\boldsymbol{\beta}^{(1)}, 4, 4, 4] = [2, 2, 2, 2, 4, 4, 4]$$

Given feature set, we can calculate the latent variable Y^* according to Equation 3.1:

$$Y^{(1)*} = \boldsymbol{\beta}^{(1)\top}\boldsymbol{x}^{(1)} + \varepsilon^{(1)}, \quad Y^{(2)*} = \boldsymbol{\beta}^{(2)\top}\boldsymbol{x}^{(2)} + \varepsilon^{(2)}$$

Cutoff points and True label Generation – $\boldsymbol{\theta}$ and $Y^{(1)}, Y^{(2)}$

Next, we can cut the continuous latent variable Y^* with cutoff points, respectively. To cut the Y^* into ordered categories, we design the cutoff points as follows:

$$L_1^* = -2.2,\ U_1^* = 2.2,\ C_2^* = 0.5$$

The value -2.2 and 2.2 are chosen because $U_1 = F(2.2) = 0.9$ and $L_1 = F(-2.2) = 0.1$ which seems to be reasonable assumption of cutoff points on probability estimation Y.

With these predefined classification thresholds, the $Y^{(1)*}$ can be cut off into 3 categories, the corresponding true label Y can be obtained accordingly:

$$Y_i^{(1)} = \begin{cases} 0, & \text{if } Y_i^{(1)*} < L_1^* \\ 0.5, & \text{if } L_1^* \le Y_i^{(1)*} < U_1^* \\ 1, & \text{if } Y_i^{(1)*} \ge U_1^* \end{cases}, \quad Y_i^{(2)} = \begin{cases} 0, & \text{if } Y_i^{(2)*} < C_2^* \\ 1, & \text{if } Y_i^{(2)*} \ge C_2^* \end{cases}$$

Also, given the above prescribed cutoff points, we have $N_2 \approx \frac{1}{3} N_1$.

In the simulation, we adopt the Monte-Carlo method and run the data generation and parameter estimation 100 times.

The story behind this synthetic data set is as follows: there is $N_1 = 10,000$ patients in total at the beginning, and all the patients have the features in category 1 collectcd, including $\boldsymbol{X}^{(1)} = \{X_1, X_2, X_3, X_4\}$. With the ordinal logistic regression model in stage 1 which has coefficients $\boldsymbol{\beta}^{(1)}$ and classification thresholds L_1^* and U_1^*, the patients with the probability of being sick larger than 0.9 or less than 0.1 are classified as almost surely sick ("1"") or almost healthy ("0"), respectively. The rest of the patients are labeled as $Y^{(1)} =$ "0.5" and recommended to the next stages to take more examinations. For this subgroup, N_2 patients in total, their features in category 2, including X_5, X_6, X_7, are actively learned, which makes the cumulative feature set for stage 2 becomes $\boldsymbol{X}^{(2)} = \{X_1, X_2, X_3, X_4, X_5, X_6, X_7\}$. Similarly, given the (ordinal) logistic re-

gression model in stage 2 with prescribed model coefficients $beta^{(2)}$ and classification threshold C_2^*, the ground truth in stage 2 can be obtained accordingly.

3.4.2 Results Comparison: Baseline Approach vs. Proposed Method with Common Coefficients Assumption

The baseline approach and proposed method with common coefficients assumption are conducted on the synthetic data set generated in the last section. In the baseline approach, the data in 2 stages are treated separately. In the first stage, a standard ordinal logistic regression is applied to data in stage 1 via $polr()$ function in the MASS package in R. And in the second stage, a standard logistic regression is applied on data in stage 2 via the $glm()$ function in R. And in the proposed model with common coefficients assumption, all the parameters in 2 stages are estimated together via MLE. Note that the common coefficients assumption indicates that the $\hat{\boldsymbol{\beta}^{(2)}} = \{\hat{\boldsymbol{\beta}^{(1)}}; \hat{\beta}_5, \hat{\beta}_6, \hat{\beta}_7\}$ where the coefficients for common features keep consistent in later stages.

In what follows, we'll evaluate the mean and the standard deviation of the parameter estimation to evaluate the accuracy and stability of the two methods.

In Figure 3.5, we visualize the comparison of the mean coefficients estimated from the two methods. From Figure 3.5, we can see that the coefficients estimated from the proposed method coincide slightly better with the ground truth for both stages. To quantify the advantage, we can quantify the distance between the estimated coefficients and the ground truth with mean square error (MSE). The MSE of the proposed 2-stage model is 0.0003, while the MSE of the baseline method conducted in stage 2 individually is 0.0011; the MSE of the proposed model for the coefficients in stage 1 is 2.25×10^{-6}, and the MSE of the baseline method conducted in stage 1 individually is also 7.62×10^{-6}.

Figure 3.6 (a) shows the standard deviation (std) of coefficients estimation from the methods. It can be seen that the standard deviation of estimation from the proposed method is significantly smaller than those from baseline methods in both stages. This is a impor-

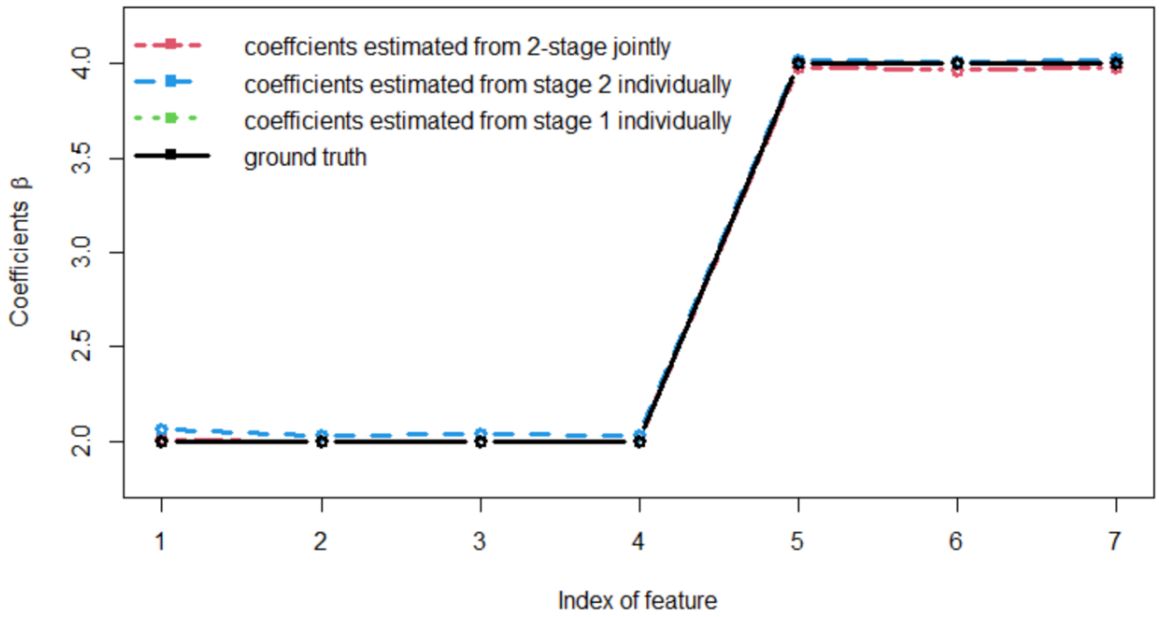

Figure 3.5: Mean coefficients estimation comparison among ground truth (black line), mean coefficients estimated from baseline approached individually (blue and green line), and mean coefficients estimated from proposed method jointly (red line).

tant advantage of the proposed methods since it proves the stability and robustness of the proposed method. The reason behind is also straightforward: in the proposed methods, all available data is involved in the parameter estimation, while in the baseline method, only a small subset of the data is involved in the parameter estimation in later stages.

Define the relative efficiency of the proposed model with respect to the baseline model as $e(T_1, T_2) = \frac{var(T_2)}{var(T_1)}$, where T_1 and T_2 represent the estimators for $\hat{\boldsymbol{\beta}}$ in the proposed model and baseline model, respectively. Figure 3.6 (b) shows the relative efficiency of the proposed method. It can be seen that the relative efficiency of the estimator in the proposed model for the coefficients in stage 1 is very big, as high as 19.38. And for the estimator for the coefficients in stage 2, the lowest relative efficiency is still as high as 1.62. This indicates that the efficiency of the parameter estimation is improved 62% 1838% in the proposed methodology. Efficiency in statistics is important because they allow one to compare the performance of various estimators. Usually, a more efficient estimator can be much more valuable. The relative efficiency strongly proved the efficiency of the proposed

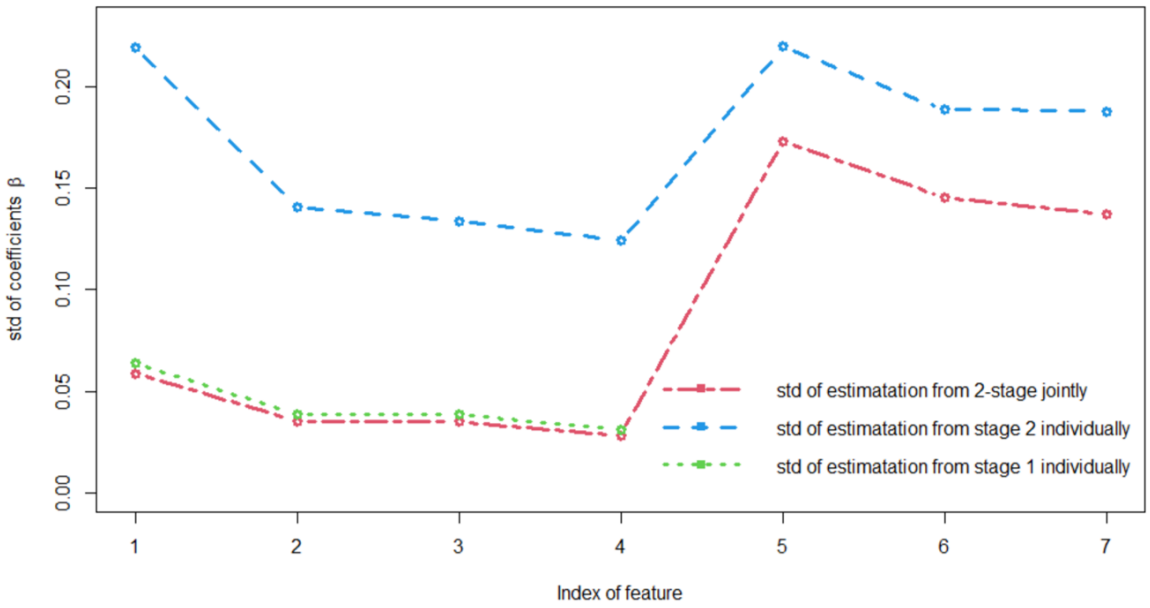

(a) Standard deviation of coefficients estimation from two methods.

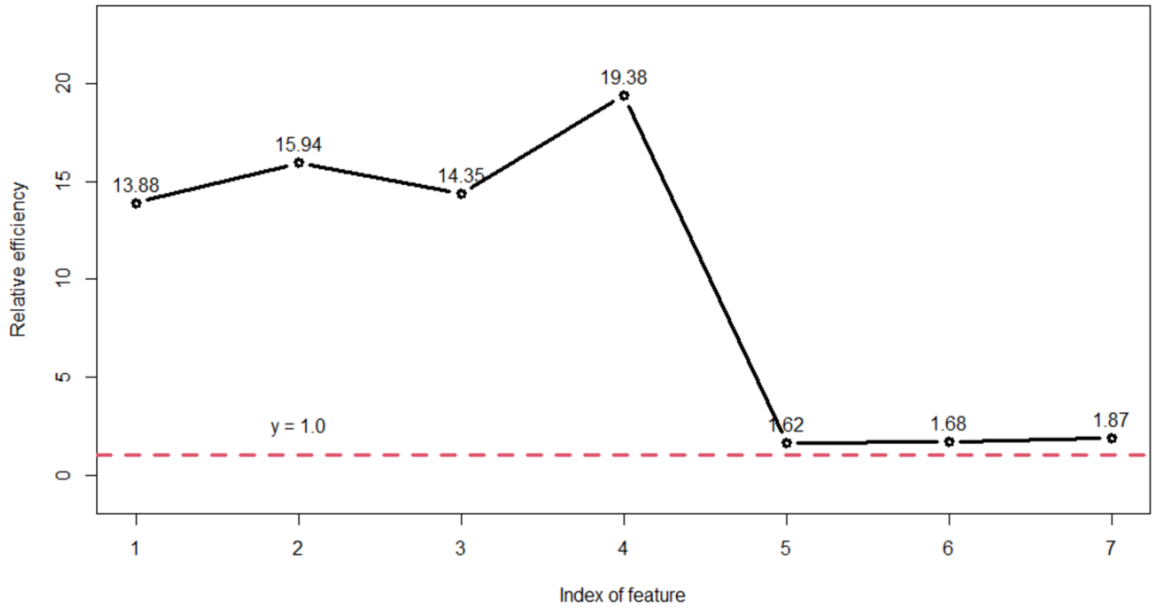

(b) Relative efficiency of the proposed model with respect to the baseline model

Figure 3.6: (a) Standard deviation of coefficients estimation from two methods, and (b) relative efficiency of the proposed method with respect to the baseline method. Both plots demonstrate the high efficiency of the proposed method on parameter estimation

methodology.

Figure 3.7 shows the mean prediction metrics for prediction for 2 stages with coefficients estimated from the two methods respectively. The evaluation metrics include sen-

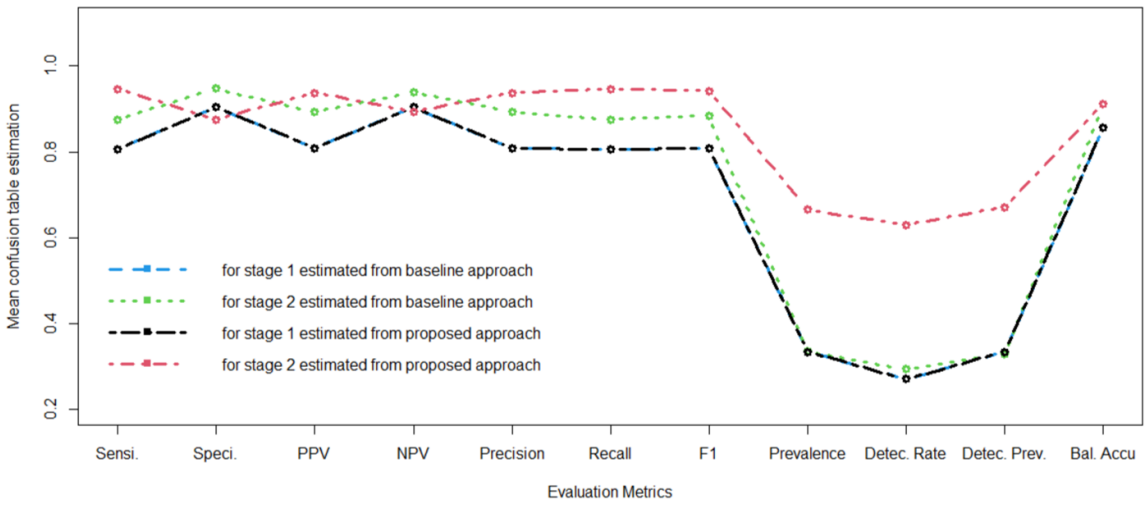

Figure 3.7: Mean prediction metrics for 2 stages with coefficients estimated from baseline approach individually (blue and green line), and coefficients estimated from proposed method jointly (red and black line). Note that the blue and black lines are too close to each other to distinguish them from each other visually.

sitivity (Sensi.), specificity (Speci.), positive predictive values (PPV), negative predictive values (NPV), and balanced accuracy, precision, recall, F1 value, prevalence, detection rate (Detec. Rate), detection prevalence (Detec. Prev.), and balanced accuracy (Bal. Accu). Balanced accuracy is a metric that one can use when evaluating how good a binary classifier is. It is especially useful when the classes are imbalanced, i.e. one of the two classes appears a lot more often than the other. In our dataset, we can see that the overall ratio of patients with and without CBDS are $Y_{0.5} : Y_1 = 120 : 196 \approx 0.38 : 0.62$, and the ratio in the stage 1 is $Y_0 : Y_{0.5} : Y_1 = 99 : 189 : 29$, in stage 2 is $Y_0 : Y_1 = 98 : 91$. Therefore, the balanced accuracy for the prediction in stage 1 is worthy of reference.

From the predictive performance comparison in Figure 3.7, it can be seen that the proposed method has a significant advantage for the prediction for stage 2 with almost higher values in every index, especially the prevalence, and detection rate, and detection prevalence. And for the prediction for stage 1, there's no significant difference between the proposed method and baseline method, as we can see that the blue and black lines are too close to each other to distinguish them from each other visually.

For the estimation of cutoff points, the baseline method and the proposed method give

the mean estimations as follows respectively:

$$mean\{\hat{L}_1^*, \hat{U}_1^*, \hat{C}_2^*\}_{baseline} = \{-2.201, 2.192, 0.536\}$$

$$mean\{\hat{L}_1^*, \hat{U}_1^*, \hat{C}_2^*\}_{proposed} = \{-2.199, 2.197, 0.506\}$$

And the standard of deviation of the estimations for the thresholds by two methods are as follows:

$$std\{\hat{L}_1^*, \hat{U}_1^*, \hat{C}_2^*\}_{baseline} = \{0.061, 0.064, 0.178\}$$

$$std\{\hat{L}_1^*, \hat{U}_1^*, \hat{C}_2^*\}_{proposed} = \{0.057, 0.062, 0.119\}$$

Compare with the ground truth, $\{L_1^*, U_1^*, C_2^*\}_{ground\ truth} = \{-2.2, 2.2, 0.5\}$, both methods work pretty well. And the proposed method has s a little bit smaller mean deviation and smaller standard deviation, working slightly better than the baseline methods.

Overall speaking, the proposed 2-stage model provides a more accurate and more stable estimation of the model coefficients since it involves all data in the parameter estimation. Also, in implementation, the proposed algorithm enjoys a big advantage of computational convenience since we estimated all parameters in ζ at once. And actually, the common coefficients assumption in the proposed model reduces the number of parameters to be estimated from $4 + 7 + 2 + 1 = 14$ to $7 + 2 + 1 = 10$ since the coefficients for features in stage 1 are not repeatedly estimated in later stages but assumed to be consistent instead.

3.5 Case Study

In this section, we'll conduct the baseline approach and our proposed algorithm with common coefficients assumption on the aforementioned real clinical dataset from the hospital. We still adopt the simplest version of our proposed mode – a 2-stage sequential decision-making model.

3.5.1 Data Review

In the proposed model, we have $N_1 = 316$ patients in the first stage. And based on the missing profile, we filter the patients who have features in the category 2 into the second stage and make their label in the first stage as $Y_i^{(1)} = 0.5, i = 1, ..., N_2$. And here $N_2 = 189$. Note that here we made the assumption that if a patient has features in the next stage observed, the patient should be labeled as "0.5" at the current stage. The reason for this assumption is that we believe that the doctor only recommends more examinations to a patient who has unclear symptoms at the current stage ("0.5"). In other words, the real data comes from the doctor's knowledge and experience, and the missing pattern is not missing at random but deliberately interfered with.

The data for the two stages are like follows:

- Stage 1: $\left\{y_i^{(1)}; x_{i,1}^{(1)}, x_{i,2}^{(1)}, \ldots, x_{i,11}^{(1)}\right\} = \left\{\boldsymbol{y}^{(1)}; \boldsymbol{X}^{(1)}\right\}, i = 1, 2, \ldots, 316,$
  $y_i^{(1)} \in \{\text{“0”}, \text{“0.5”}, \text{“1”}\};$
- Stage 2: $\left\{y_i^{(2)}; x_{i,1}^{(1)}, x_{i,2}^{(1)}, \ldots, x_{i,11}^{(1)}; x_{i,1}^{(2)}, x_{i,2}^{(2)}, \ldots, x_{i,4}^{(2)}\right\} = \left\{\boldsymbol{y}^{(2)}; \boldsymbol{X}^{(2)}\right\},$
  $i = 1, 2, \ldots, 189, y_i^{(2)} \in \{\text{“0”}, \text{“1”}\};$

where features in $\boldsymbol{X}^{(1)}$ includes hemolytic disease, gender, age, body mass index (BMI), total bilirubin, Alanine transaminase (ALT), Aspartate transaminase (AST), lipase, amalyse, Gamma-glutamyl transferase (GGT), Alkaline phosphatase (ALP). These features include demographic and laboratory blood test measurements. For features in $\boldsymbol{X}^{(2)}$, based on $\boldsymbol{X}^{(1)}$, it involves new imaging test data, including common bile duct (CBD) diameter and the presence of CBDS by US and MRI examinations, respectively. The descriptive statistics were calculated for all variables of interest in Table 3.1.

3.5.2 Performance Comparison: Baseline Approach vs Proposed Algorithm

The proposed method and baseline method are conducted and compared on the organized real data similar to the simulation study. Figure 3.8 visualizes the coefficients for features

Table 3.1: Descriptive statistics for demographic, laboratory, and imaging data

	CBD Stone Present	No CBD Stone Present	p-value
Total patients	120	196	
IOC	81	196	
ERCP	39	0	
Hemolytic disease	$23(19.2\%)$	$49(25.0\%)$	0.270
Female	$81(67.5\%)$	$123(62.8\%)$	0.400
Age (yrs)	13.8 ± 3.3	13.6 ± 3.6	0.883
BMI $(\mathrm{kg/m^2})$	25.7 ± 8.0	24.5 ± 8.7	0.125
Total bilirubin $(\mathrm{mg/dL})$	5.6 ± 8.3	2.6 ± 5.2	< 0.001
ALT (U/L)	258.5 ± 195.8	132.9 ± 146.2	< 0.001
AST (U/L)	153.3 ± 135.6	87.9 ± 110.6	< 0.001
Lipase (U/L)	578.4 ± 1516.9	268.4 ± 517.8	0.538
Amylase (U/L)	113.6 ± 197.8	119.3 ± 190.9	0.011
GGT (U/L)	296.0 ± 202.0	232.5 ± 216.1	0.024
Alkaline phosphatase (U/L)	247.1 ± 189.6	179.7 ± 98.1	0.014
CBD diameter (mm, by US)	7.4 ± 3.8	5.6 ± 3.8	< 0.001
Presence of CBD stone (US)	$11(13.4\%)$	$3(3.1\%)$	0.012
CBD diameter (mm, by MRI)	9.3 ± 3.8	8.3 ± 2.6	0.420
Presence of CBD stone (MRI)	$28(54.9\%)$	$10(19.6\%)$	0.041

in category 1 estimated by the baseline approach and proposed 2-stage model.

It can be seen that with the baseline line approach, the coefficients estimated by the two individual models are similar to each other for most features, $X_2 \sim X_{11}$, but significantly different for X_1. While with the proposed 2-stage model, the coefficients estimated for feature $X_1 \sim X_{11}$ seems to be a kind of weighted average of the coefficients obtained from baseline individual models and falls in between. Note that the estimated coefficients for features in stage 2 are not plotted here. This is because the $\hat{\boldsymbol{\beta}}^{(1)}$ hardly affect $\hat{\boldsymbol{\beta}}^{(2)}$, but the $\hat{\boldsymbol{\beta}}^{(2)}$ affect $\hat{\boldsymbol{\beta}}^{(1)}$ in some way. Thus, we focus on the comparison on the estimated common coefficients.

Compared with the baseline methods, the coefficients estimated by the proposed method have no dramatic spikes. Also, with the common coefficients assumption, our collaborator doctors feel more comfortable since newly added features will not affect the weights of existing ones. More importantly, in the proposed model, no matter how many stages the doctors prefer to use, the calculation can be done at once, which is much simpler than

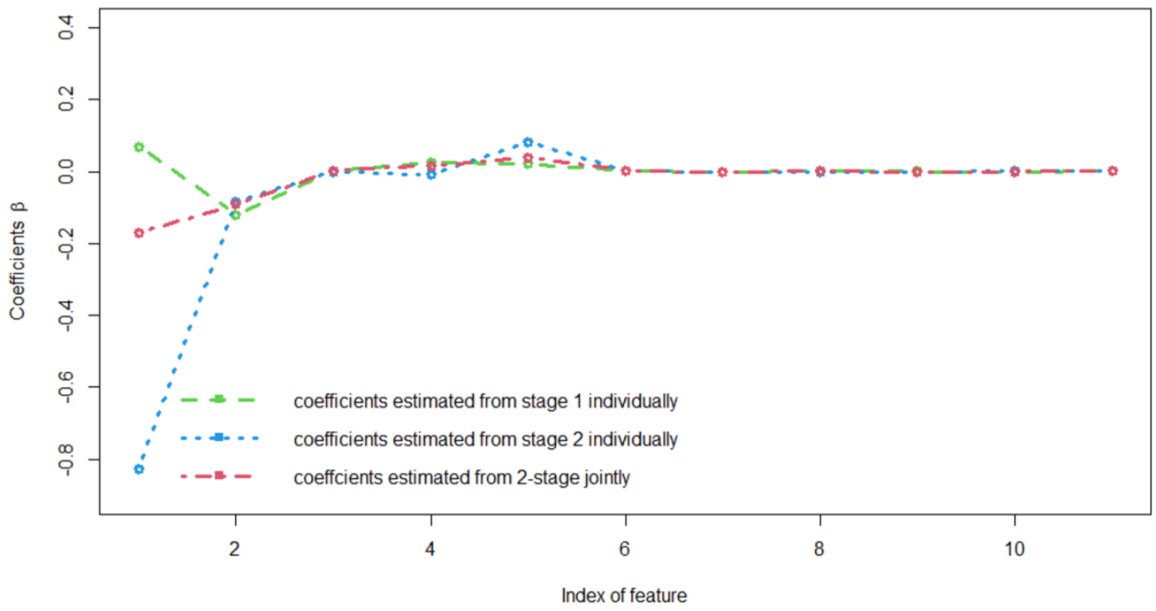

Figure 3.8: Coefficients comparison between coefficients obtained from 2 methods for features in stages 1.

building an individual model for each stage.

Given the parameters $\hat{\boldsymbol{\zeta}}$ estimated by the proposed model, when a new patient comes, the doctor can first recommend the patient to take examinations included in category 1, and calculate the $\hat{Y}^{(1)}$ accordingly. Based on the $\hat{L}_1$ and $\hat{U}_1$, the patient will be labeled as healthy ("1"), sick ("0"), or unclear and recommended to next stage ("0.5"). Then, only the patients whose symptoms are ambiguous are recommended to take extra examinations. In other words, only the necessary data are learned actively and sequentially, and the decisions are made sequentially. Definitely, this makes the whole diagnosis process quicker and cheaper, more intelligent and friendly. Besides, the doctors can adjust the multistage sequential decision-making model flexibly by designing the number of stages and the features in each stage. More details can be found in the feature grouping recommendations in Section 3.2.

3.6 Conclusion and Discussion

In this study, to augment healthcare clinical decision-making based on limited examinations, a multistage sequential decision-making model is developed to actively collect only minimal necessary diagnostic data.To illustrate the proposed model, we optimized a 2-stage model on synthetic data in the simulation study and applied the proposed algorithm to pediatric patients with suspicion for obstructive common bile duct stones in an effort to more efficiently and accurately arrive at a diagnosis that allowed expedited intervention with ERCP. In both the simulation study and real case study on collected pediatric data, the proposed method is more effective, stable, interpretable, and simpler in estimating the coefficients and cutoff points for all stages. It estimates all parameters simultaneously and fully considers the cumulative characteristics between these stages by making common coefficients assumption.

One limitation of the proposed methodology is that it involves all variables without selection. A potential future improvement to the model will be the addition of L_1 regularization term to the objective function to realize the variable selection.

Also, we can extend our proposed algorithm to satisfy more real-world cases with special requirements. For example, consideration of expense, delay to intervention, and need for invasive testing can be specified and minimized with modification to the objective function as follows:

$$\min_{N_1,N_2,\zeta} -\log \mathcal{L}(\zeta \mid X, Y) + \lambda \left(c_1 N_1 + c_2 N_2\right)$$

where the c_1, c_2 are the relevant cost per patient in stage 1 and stage 2, respectively. λ is the tuning parameter to adjust the weight between the negative likelihood and the relevant cost to the test. Note that here the N_1, N_2 can also be variables to be optimized over since the relevant cost depends on the number of patients in each stage.

In a healthcare setting, the penalty for misdiagnosis can vary based on the patient and diagnosis. For example, false-positive detection may lead to unnecessary procedures or

excess intervention, while false-negative detection may result in missed or delayed treatment. For such cases with weighted penalties on different types of misclassification, we can modify the objective function by specifying the penalties as follows:

$$\min_{\zeta} -\log \mathcal{L}(\zeta \mid X, Y) - \lambda_1 \sum_i I\left((y_i = 0.5 \mid 1), \hat{y}_i = 0\right) - \lambda_2 \sum_i I\left((y_i = 0 \mid 0.5) \,\&\, \hat{y}_i = 1\right)$$

where the λ_1 and λ_2 are the tuning parameter for false-negative prediction and false-positive prediction, respectively.

The proposed algorithm is also applicable to a broad range of decision-making scenarios outside of healthcare as it utilizes active learning to drive the sequential collection of minimal requisite information, rather than all possible information simultaneously. This will be an area of future development.

CHAPTER 4

UNSUPERVISED IMAGE SEGMENTATION WITH AN APPLICATION ON THE FAILURE MODE ANALYSIS FOR AIRPLANES

Image analysis refers to extracting meaningful information from digital images by digital image processing techniques [60]. Among them, image segmentation is a very hot topic that simplifies and/or changes the representation of an image into something that is more meaningful and easier to analyze, and thus is popular in object detection and tracking in medical imaging, traffic control systems, etc. In this project, our objective is to analyze the failure modes distribution and proportion on the surface of the CFRP specimen after the double cantilever beam (DCB) testing to investigate the surface property such as fracture toughness. From the image data captured from the CFRP specimen after the DCB testing, our task is to identify the attribution of each pixel, pink adhesive film or black CFRP substrate, on both pieces of the originally bonded specimens, which is essentially unsupervised image segmentation.

There are several significant challenges associated with image segmentation for failure mode analysis. For example, limited data size, imperfect imaging quality, unavailable true pixel labels. All of them limit the use of supervised machine learning algorithms. Besides, these pixels are not independent so that the spatial correlation among them should be properly considered. And the paring of pixels from symmetric faces which are originally bonded together should have some tolerance. To overcome these challenges, considering the specificity of this project, a baseline approach is proposed first: using the superpixels algorithm to push up the investigation from pixel-level to region-level (superpixels) first, then cluster the superpixels to binarize the labels of superpixels. The unsatisfactory performance of the baseline method drives us to propose a simple yet very effective method, named RG-filter, for our imaging data specially.

Unlike the traditional thresholding methods which work on the compressed grayscale image and lead to information loss, our proposed RG-filter works on the RGB color image directly with adjustable multiplicative coefficients and offset parameters. The effectiveness of the proposed RG-filter is then verified on our CFRP image data from experiments. The image segmentation results represent the distribution and proportion of failure modes. From the failure mode analysis, people can better understand the weak link during the bonding of composite materials, model them together with some downstream data as a whole, and the time-consuming and destructive DCB testing can be avoided accordingly. This would be very helpful for the joining and maintenance of aircraft.

4.1 Introduction

Bonding quality between composite material surfaces is the crucial and long-term focus of aircraft joining and maintenance. The DCB testing is a standard test method for determining mode I (opening mode, a tensile stress normal to the plane of the crack) fracture toughness of fabric composites or adhesively bonded joints [61]. The industry standard is to use a fixed-width DCB to perform the test, which is one of the widely-used methods to calculate the fracture toughness [62].

The motivation of this project is to identify the failure mode distribution and proportion over the surface of two pieces of originally bonded CFRP panels after DCB testing. After figuring out the distribution and proportion of failure mode, people can better understand the weak link during the bonding of composite material, which may give some clue on how to improve the quality of joining and repairing for aircraft. More importantly, the segmentation results can be crucial data when modeling together with some downstream data. Once we can predict the failure mode proportion and distribution directly from some easily obtained surface characterizing variables, the expensive, time-consuming, and destructive DCB testing can be avoided, and naturally, a huge amount of time and money will be saved.

There are several significant challenges associated with unsupervised image segmen-

tation for failure mode analysis. For example, we only have 50 images or so due to the expensive and time-consuming destructive testing. And the imaging quality is not ideal due to uneven light and strong reflection during data collection. What's worse, the true labels for these pixels are not available. Although our laboratory specialist can roughly clarify the identity of small regions by visual observation, it is not realistic to label every pixel for the training of supervised machine learning algorithms.

Another big challenge is, our data is not independent images, but **image pairs** coming from the two CFRP panels originally bonded together before DCB testing. Under such a situation, it is impossible to recover the exact location and paring relationships for pixel pairs from the symmetric specimen faces. Also, the pixels on the same face are not independent and the spatial correlation between them should be properly addressed.

Also, for our CFRP images, the label of the pixels are binary, which limits the direct use of the existing image segmentation algorithms. This is because the existing image segmentation usually focuses on grouping similar pixels together and identifying finer boundaries, but the labels of those superpixels are usually increasing integers without physical meaning. They tend to segment an image into many pieces for better boundary detection and create the same number of labels for them. While in our case, these multiple segment labels should be further clustered into two groups.

To address the challenges above, in this study, we proposed two segmentation methods for failure mode analysis after exploring our image data carefully. One is the baseline approach where we propose to add an extra layer of clustering on the regions rather than a single pixel. Compared with the existing superpixels algorithm for image segmentation, it adds one more step to cluster the segmented superpixels which enables us to specify the level or type of the label. In other words, it enables us to segment the CFRP specimen into many regions of only two types, pink adhesive film or black CFRP substrate. As we'll see, the baseline approach does not work ideally, which drives us to propose an image segmentation method specially for our CFRP image data. In the proposed method,

we investigate the problem in the thresholding direction. Unlike the existing thresholding methods which work on the grayscale channel with some information loss, we proposed an RG-filter method that works directly on the raw RGB image, labels the pixels according to the relationship between the red (R) channel and green (G) channel.

In Section 4.2, the problem formulation, literature review of image segmentation, and the baseline approach are elaborated. In Section 4.3, the proposed method is introduced in detail. Then, in Section 4.4, a series of experiments are conducted on our CFRP image to compare the performance of the typical existing image segmentation methods, baseline method, and the proposed method. In the end, this project is concluded and discussed further in Section 4.5.

4.2 Problem Formulation, Literature Review, and Baseline Approach

In this section, first, the engineering problem is formulated as an unsupervised image segmentation problem in a statistical manner, and the specificity of this project is highlighted. Then, a thorough literature review over the state-of-the-art for image segmentation is provided. Finally, a baseline approach is proposed accordingly to tackle these challenges preliminarily.

4.2.1 Problem Formulation

Figure 4.1 shows 4 typical image pairs captured from originally bonded CFRP pairs after the DCB testing. In an image, the two CFRP panels are referred to as A face (to the bottom) and B face (to the top), respectively. On the surface of CFRP specimens, the black substrate is the CFRP panel manufactured in our lab, and the pink material is the adhesive film used for bonding the two panels before DSB testing. Though the pixel color/type in the specimen varies gradually and continuously, it has to be identified with binary labels, either “pink adhesive films”, or “black CFRP substrate”. Therefore, the color information is critical for pixel labeling. Also, some other additional information, like texture and brightness, may

also be helpful or misleading and be captured by machine learning algorithms for pixel labeling.

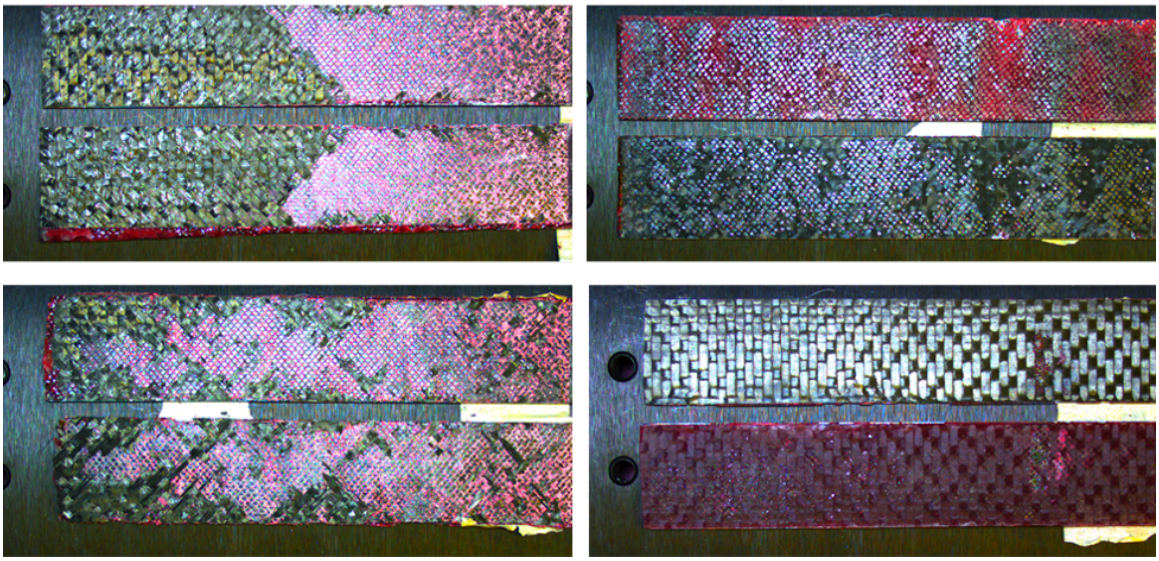

Figure 4.1: Several typical CFRP pairs. These images demonstrate the pairing relationship and indicate the challenges associated with the raw data.

The potential failure modes of adhesive bonds between composite materials are shown in Figure 4.2. This figure comes from a single-lap joint (SLJ) specimen [63], but the failure modes are the same as the specimen after the DCB testing in our case. The cohesive failure refers to the type of brokenness that occurs inside the adhesive film when stretching, see the purple part in (a). The adhesive failure refers to the detachment between cohesive film and CFRP substrate when stretching, see (b). And the adherent failure, also called substrate failure, refers to the brokenness that occurs inside the CFRP substrates, see (c). Different types of failure modes indicate different relative weak links during the stretching of DCB testing, which provides some clue for improvement in future bonding work for aircraft joining and repairing.

The failure mode can be identified after labeling pixel pairs on the broken specimens according to the labeling rule shown in Table 4.1. The pixel pairs refer to 2 pixels that originally bonded together at the same location before stretching apart and now lay on A

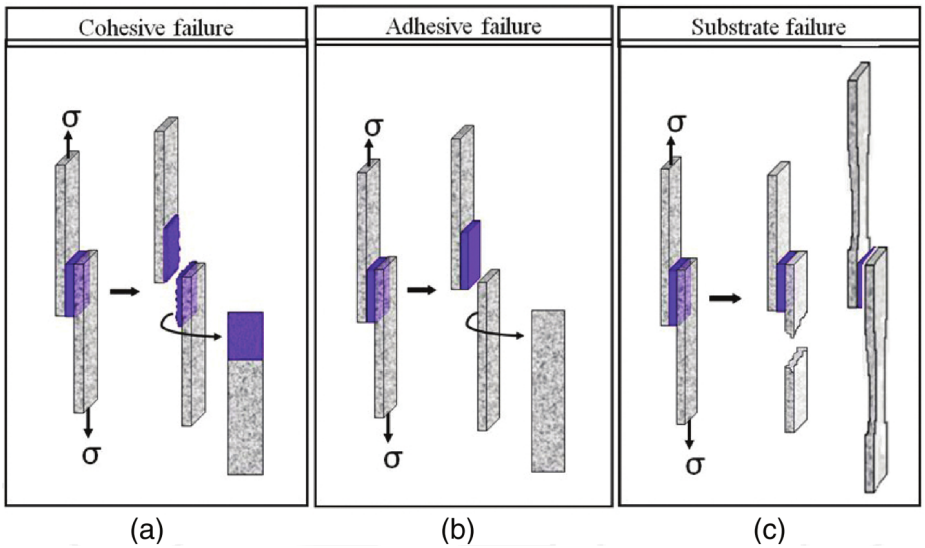

Figure 4.2: Types of adhesive bond failure of SLJ specimen [63]: a) cohesive failure, b) adhesive failure, c) adherent (substrate) failure.

face and B face symmetrically.

Table 4.1: Rule of identifying failure mode from pixel pairs

Pixel Pairs	Failure Mode
black-to- black	adherent(substrate) failure
pink-to-pink	cohesive failure
black-to-pink/pink-to-black	adhesive failure

The expected outcome is shown in Figure 4.3, including the distribution of the failure modes and the proportions of them on the specimens. Therefore, our objective is to develop an unsupervised image segmentation algorithm for the image data shown in Figure 4.1 and obtain the segmented results shown in Figure 4.3. Given the distributions and proportions of different failure modes for adhesive bonding, people can optimize the bonding quality for aircraft in a more comprehensive analysis, such as involving other isolate studies associated with CFRP surface quality, adhesive film storage, and CFRP panel manufacturing.

4.2.2 Literature Review of Image Segmentation

Image segmentation is the process of partitioning a digital image into different regions (sets of pixels, also known as superpixels) based on the characteristics of pixels. The goal

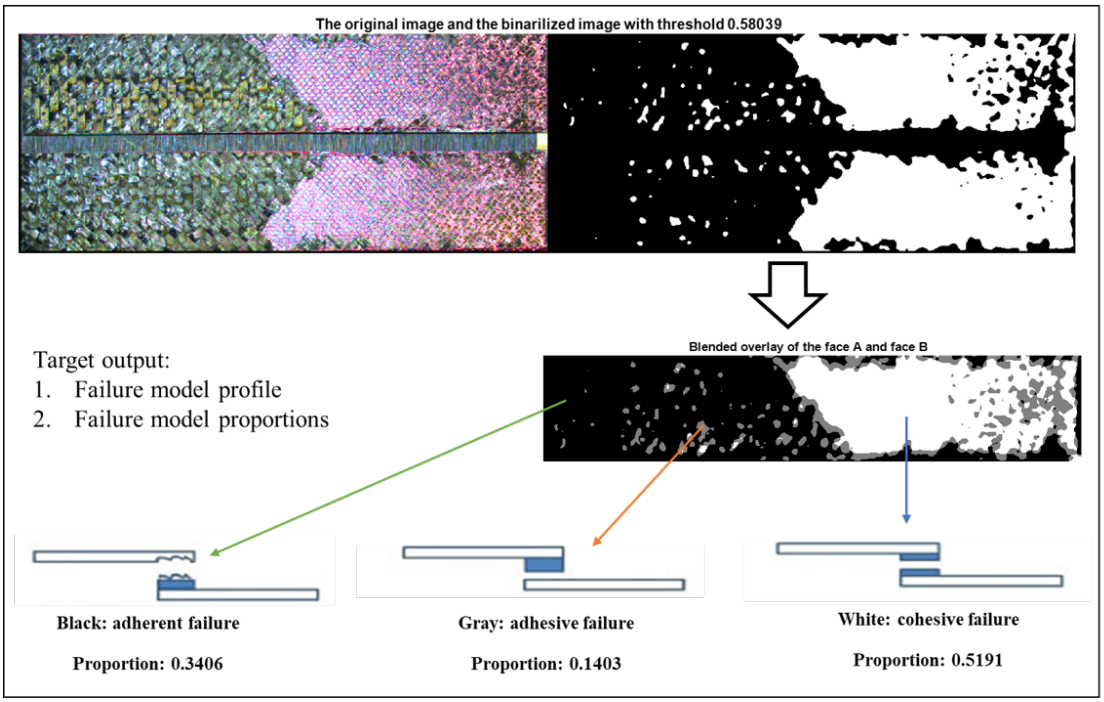

Figure 4.3: An example of the expected outcome from raw data. The raw image data (figure to the top right), and the expected outputs, including failure modes distribution (figure in the middle row) and proportion (figures in the last row).

of segmentation is to simplify and/or change the representation of an image into something that is more meaningful, easier, and efficient to analyze. Image segmentation is typically used to locate or identify objects and boundaries (lines, curves, etc.) in images. More precisely, image segmentation is the process of assigning a label to every pixel in an image such that pixels with the same label share certain characteristics. Segmentation impacts a number of domains. For example, in the filmmaking industry, image segmentation can be used to crop out the foreground and place it into certain backgrounds. Also, it can be used to track objects in a sequence of images. Besides, in the medical field, it can be used to identify the injured muscle and measure the bone or tissue [16].

The algorithms for image segmentation have been well-developed these years. In Table 4.2, we summarized these image segmentation algorithms based on the ideas and mechanisms behind them. In what follows, these algorithms are approximately grouped into three typical methodologies and discussed respectively: thresholding-based methods,

pixel-wise clustering-based methods, and deep learning-based methods.

Table 4.2: Overview of Superpixels-Based Image Segmentation

Mechanisms	Algorithms
Thresholding-based	Maximum entropy method
	Balanced histogram thresholding
	Otsu's method (maximum variance)
Desnity-based	Edge-Augmented Mean Shift (EAMS), Comaniciu and Meer [64], 2002
	Quick Shift (QS), Vedaldi and Soatto [65], 2008
	Density-Based Spatial Clustering of Applications with Noise (DBSCAN), Ester [66],1996
Watershed-based	Watershed (W), Meyer[67], 1993
	Compact Watershed(CW) Neubert and Protzel [68], 2014
	Morphological Superpixel Segmentation (MSS), Benesova and Kottman [69], 2014
	Water Pixels (WP), Machairas et al. [70], 2010
Graph-based	Normalized Cuts (NC), Ren and Malik [71], 2002
	Felzenswalb and Huttenlocher (FH), Felzenswalb et al. [72], 2004
	Random Walks (RW),Grady et al. [73], 2006
	Constant Intensity Superpixels (CIS), Veksler et al. [74], 2010
	Entropy Rate Superpixels (ERS), Liu et al.et al, [75], 2011
	Boolean Optimization Superpixels (PB), Zhang et al. [76], 2011
	Proposals for Objects from Improved Seeds and Energies (POISE),Humayun et al. [77], 2015
Contour evolution	Turbo Pixels (TP), Levinshtein et al. [78], 2009
	Eikonal Region Growing Clustering (ERGC), Buyssens et al. [79], 2014
Path-based	Path Finder (PF), Drucker et al. [80], 2009
	Topology Preserving Superpixels (TPS), Dai et al. [81], 2012
Clustering-based	Simple Linear Iterative Clustering (SLIC), Achanta et al [82], 2010
	k-means clustering, Pedregosa, Fabian et al [83], 2011
	Depth-Adaptive Superpixels (DASP), Weikersdorfer et al. [84], 2012
	VCells (VC), Wang and Wang [85], 2012
	Voxel-Cloud Connectivity Segmentation (VCCS), Papon et al. [86], 2013
	Preemptive SLIC (preSLIC), Neubert and Protzel [68], 2014
	Linear Spectral Clustering (LSC), Li and Chen [87], 2015
Energy optimization	Contour Relaxed Superpixels (CRS), Conrad et al. [88], 2013
	Superpixels Extracted via EnergyDriven Sampling (SEEDS), Van den Bergh et al. [89], 2012
	Convexity Constrained Superpixels(CCS), Tasli et al. [90], 2013
	Extended Topology Preserving Segmentation (ETPS), Yao et al. [91], 2015
Wavelet-based	Superpixels from Edge-Avoiding Wavelets (SEAW), Strassburg et al. [92], 2015
Deep Learning-based	Region-based semantic segmentation (R-CNN)
	Fully convolutional Network-based semantic segmentaion [93], 2015
	Weakly supervised semantic segmentation

Methodology I: Image Segmentation by Thresholding

The thresholding method is the simplest and most intuitive method for image segmentation. Based on a well-designed threshold value, this method binarizes the pixels of continuous single level or multiple levels, such as grayscale and RGB images. The key of such methods is identifying the threshold value(s). The overview of several popular algorithms using the thresholding ideas is shown on the top of Table 4.2. Recently, more thresholding-based

algorithms are developed towards the direction of multi-dimensional fuzzy rule-based non-linear thresholds.

Otsu's method is widely used to perform automatic image segmentation with global optimal threshold [94]. The output of this algorithm is a single intensity threshold that separates pixels into two classes: foreground and background. This threshold is determined by minimizing intra-class intensity variance, defined as a weighted sum of variances of the two classes, which is equivalent to maximizing inter-class variance. Otsu's method is a one-dimensional discrete analog of Fisher's Discriminant Analysis. It is related to the Jenks optimization method, and equivalent to a globally optimal k-means[95] performed on the intensity histogram. The extension to multi-level thresholding as described in the original paper [94] and computationally efficient implementations have since been proposed [96].

Besides Otsu's methods, there are also many choices for finding optimal global threshold values. Isodata thresholding is a way to automatically find a threshold for a given gray value image. The thresholding t is a value on grayscale such that t is halfway in between the mean of all pixels less than t and the mean of all pixels great than t: $t = \frac{m_L(t)+m_H(t)}{2}$. In Li thresholding, the objective is minimizing the cross-entropy between the foreground and the foreground mean, and the background and the background mean. It would give the best threshold in most situations. Mean thresholding, as its name suggests, is simply taking the mean grayscale value as the threshold. The minimum algorithm takes a histogram of the image and smooths it repeatedly until there are only two peaks in the histogram, then the minimum in between is the threshold value. The triangle method constructs a line between the histogram peak and the farthest end of the histogram. The threshold is the point of maximum distance between the line and the histogram. Yen implements thresholding based on a maximum correlation criterion as a more computationally efficient alternative to entropy measures.

There also exist some local thresholding algorithms. If the image background is relatively uniform, then you can use a global threshold value as Otsu's method do. However,

if there is a large variation in the background intensity, local thresholding, also known as adaptive or dynamic thresholding, may produce better results. Note that local is much slower than global thresholding in computation. The idea behind adaptive thresholding is simple. For example, if we binarize an image using the $threshold\_adaptive$ function in Python, which calculates thresholds in regions of size $block\_size$ surrounding each pixel (i.e. local neighborhoods). Each threshold value is the weighted mean of the local neighborhood minus an offset value.

Methodology II: Image Segmentation by Pixel-Wise Clustering

Another widely used methodology for implementing image segmentation is clustering at the pixel level, which we called pixel-wise clustering. With the widespread application of machine learning algorithms, it is natural to group pixels using the clustering algorithm, a methodology of unsupervised learning which don't require the true class label but group data points into groups based on some properties like distance or similarity.

In pixel-wise clustering, pixels sharing certain features, such as color, intensity, and texture, are grouped together and represented as a single entity called superpixel. Ren and Malik [71] introduced the superpixel-based algorithms, where superpixels group pixels similar in color and other low-level properties such as location coordinate. By involving location information, the spatial correlation between pixels is toke into consideration.

The contribution of involving superpixels is significant since it addresses two problems inherent to the processing of digital images: firstly, pixels are merely a result of discretization; and secondly, the high number of pixels in large images limit the computational feasibility of many algorithms. By grouping pixels that perceptually belong together, superpixels heavily reduce the number of primitives for subsequent algorithms [97].

In Table 4.2, the popular superpixel-based image segmentation algorithms are summarized with the help of an overview from David et al. [97]. In what follows, we'll elaborate on several typical pixel-wise clustering algorithms for image segmentation.

1. K-means [83]

   K-means is one of the most widely used clustering algorithms in the data science and machine learning area. Given a set of observations, k-means clustering aims to partition the n observations into $k(\leq n)$ sets so as to minimize the within-cluster sum of squares, i.e. variance. The key idea behind it can be expressed in its implementation process, a two-step iterative process: after randomly picking k centroids as group centers, (1) Each data point is classified into the group which has the closest centroid to it. (2) Based on these classified points, update the centroid for each group by taking the *mean* of all the members in the group. Repeat (1) and (2) for a fixed number of iterations (maximum iterations) or until the group centers don't change much between iterations (predefined tolerance). Note that if we modify step (2) a little bit by choosing real data points as centers (medoids or exemplars) rather than the group means, it becomes a new algorithm, the k-medoids algorithm.

   K-Means has the advantage that it is computationally efficient as we only compute the distances between points and group centers. Also, it is almost sure to converge to a locally optimal solution. On the other hand, K-Means has a couple of disadvantages. For example, the number of clusters k is an hyper parameter that determines the clustering performance and is not trivial to specify. Also, it can reach a global optimum after several random starts.

2. Mean-Shift Clustering [64]

   Mean-shift is a popular non-parametric clustering algorithm based on the idea of associating each data point to a mode of the underlying probability density function. It is a sliding window-based algorithm aiming at finding dense areas of data points. Assume a circular window centered at a random point C with a prescribed radius r is the kernel. The mean shift algorithm shifts this kernel iteratively to a higher density region until convergence, just like climbing hills. At every iteration, the kernel is

shifted to the centroid or the mean of the points within it.

The Mean Shift takes usually 3 inputs: (i) a well-defined distance function for measuring distances between pixels, such as Euclidean distance and Manhattan distance; (ii) a radius. All pixels within this radius (measured according to the above distance) will be accounted for in the calculation; and (iii) a value difference. From all pixels inside radius r, we will take only those whose values are within this difference for calculating the mean.

The simple clustering criterion has appealing advantages compared to other traditional clustering techniques: the structure of the clusters may be rather arbitrary and the number of clusters does not need to be known in advance as mean-shift automatically discover this. Also, being able to converge at the points of maximum density is quite desirable in real-world applications. The drawback is the selection of window size/radius r, which can be non-trivial.

3. Simple Linear Iterative Clustering (SLIC) [82]

   The SLIC algorithm can be seen as k-means in the five-dimensional (5D) space of color information (defined by the L, a, b values of the CIELAB colorspace) and image location (x, y coordinates). SLIC effectively generates compact and nearly uniform superpixels by clustering pixels based on their color similarity and proximity in the image plane, a combined 5D space.

   The SLIC is the state-of-the-art algorithm to segment superpixels without a high requirement computational power due to the simplicity of the k-means clustering mechanism. Meanwhile, it will encounter the drawbacks associated with the k-means clustering algorithm. In the implementation, it takes 2 input parameters mainly: (i) the $compactness$ parameter trades off color-similarity and proximity, as in the case of Quickshift, while (ii) the $n\_segments$ chooses the number of centers for K-means.

4. Felzenswalb' method [72]

   Felzenszwalb's method is a fast 2D image segmentation algorithm that is popular in the computer vision community. It is an efficient graph-based segmentation method developed with the motivation to speed up the segmentation of large images. Graph-based image segmentation accomplishes this by splitting images into tiles that are processed independently. The connectivity information inherent to graphs allows performing independent work on parts of the original image, and reconnecting them to yield an exact result as if processing had occurred globally.

   The Felzenszwalb method is developed based on Kruskal's minimum spanning tree (MST) algorithm. Edges are considered in increasing order of weight; their endpoint pixels are merged into a region if this doesn't cause a cycle in the graph, and if the pixels are 'similar' to the existing regions' pixels. Detecting cycles is possible in near-constant time with the aid of a disjoint-set data structure. Pixel similarity is judged by a heuristic, which compares the weight to a per-segment threshold. The algorithm outputs multiple disjunct MSTs, i.e. a forest, and each tree corresponds to a segment. The complexity of the algorithm is quasi-linear because sorting edges is possible in linear time via counting sort.

   In the implementation, the algorithm has a single scale parameter that influences the segment size. The actual size and number of segments can vary greatly, depending on local contrast.

5. Quickshift method [65]

   Quickshift is a relatively recent 2D image segmentation algorithm, based on an approximation of kernelized mean-shift. Like medoid shift, quick shift operates in non-Euclidean spaces in a straightforward manner. Therefore it belongs to the family of local mode-seeking algorithms and is applied to the 5D space consisting of color information and image location, similar to the SLIC method. One of the bene-

fits of Quickshift is that it actually computes a hierarchical segmentation on multiple scales simultaneously.

In the implementation, Quickshift has two main parameters: σ controls the scale of the local density approximation, max_dist selects a level in the hierarchical segmentation that is produced. There is also a trade-off between distance in color-space and distance in image-space, given by ratio.

6. Compact watershed [98]

   The Compact Watershed is based on Seeded Watershed segmentation but creates uniformly shaped superpixels similar to SLIC. The watershed transform is commonly used as a starting point for many segmentation algorithms. However, without a judicious choice of seeds, it can produce very uneven fragment sizes, which can be difficult to deal with in downstream analyses. The *compact* watershed transform remedies this by favoring seeds that are close to the pixel being considered.

   It is a marker-based algorithm. Starting from user-defined markers, the watershed algorithm treats pixels values as a local topography (elevation). The algorithm floods basins from the markers until basins attributed to different markers meet on watershed lines. In many cases, markers are chosen as the local minima of the image, from which basins are flooded.

   In the implementation, the user will specify which valley points are to be merged and which are not, which makes it interactive but not automatic. The "marker-based" means labeling where the region is a foreground or a background and gives different labels for known objects. We label the region which is sure of being the foreground with one color or intensity, and label the apparent background with another color or intensity. Then, label the indeterminate region with 0. That is the so-called marker. After that, we apply the watershed algorithm. Then the markers will be updated with the labels we gave, and the boundaries of objects will have a value of -1.

Besides these typical image segmentation algorithms, there is a bunch of popular clustering methods that will not be elaborated on in this study. Their performance is shown in Figure 4.4. In this figure, every column corresponds to the clustering performance of a certain clustering method, and each color indicates a predicted cluster. From this figure, we can see that the performance of a clustering method is closely associated with the data structure/underlying shape. The data structure and density profile should be determining factors in deciding the clustering mechanism.

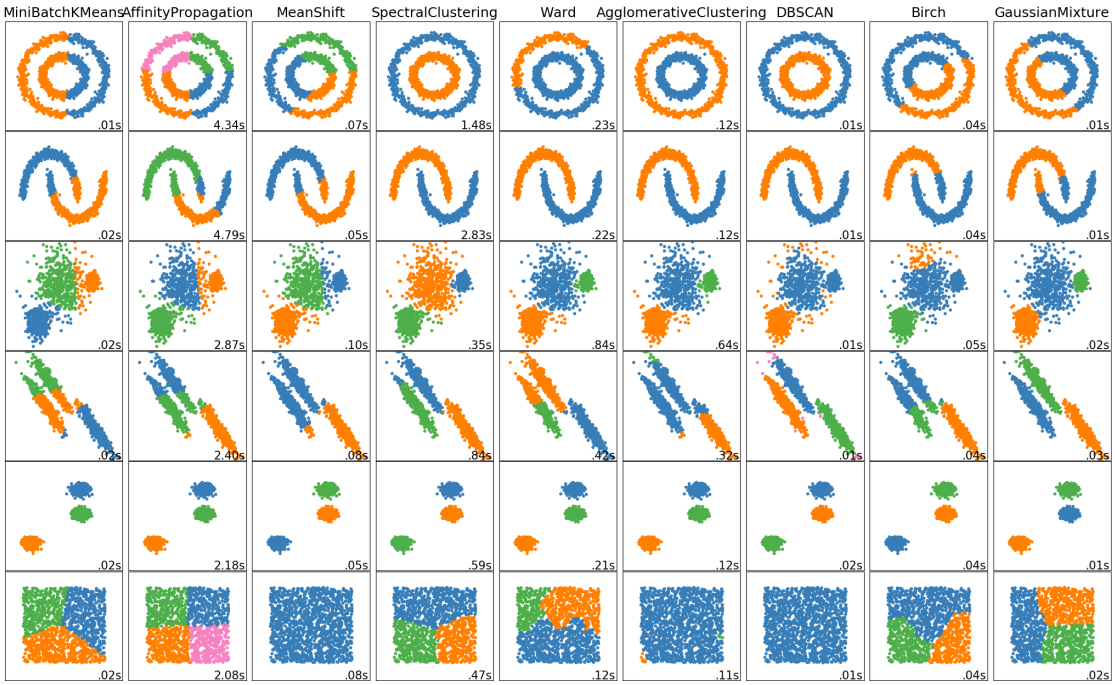

Figure 4.4: Performance comparison of several popular clustering algorithms on 5 datasets with different structure/shape [99]. Every column corresponds to a certain clustering method, and each color indicates a predicted cluster.

Methodology III: Image Segmentation by Deep Learning

Another fantastic way to do image segmentation is the deep convolutional network (CNN), which is often referred to as semantic segmentation or semantic image segmentation [100, 93]. Generally, a typical semantic segmentation architecture can be roughly thought of as the combination of an encoder network and a decoder network. The encoder is usually a

pre-trained classification network like VGG/ResNet followed by a decoder network. The task of the decoder is to semantically project the discriminative features (lower resolution) learned by the encoder onto the pixel space (higher resolution) to get a dense classification.

Although very attractive, deep learning methods usually require a huge amount of data for training, and most of the existing image segmentation methods with deep learning are supervised learning which requires the true label of the segmentation. Therefore, in this project, deep learning will not be implemented on our CFRP data.

4.2.3 Baseline Approach - Superpixels Clustering Methodology

In Section 4.2.2, it is was emphasized that the image segmentation result highly depends on the data structure, and people should choose the proper algorithm according to the properties of the actual data set. For our CFRP image data, the problem associated with these segmentation methods is the number of label types. Usually, the existing methods segment the image into a lot of different regions with different labels in the mask. In implementations, often the cases, the number of segmentation is equaled to the type or level of labels with a one-to-one relationship. Roughly speaking, the more the regions segmented, the finer the boundary identification. However, in our cases, we expect fine boundaries yet only two types of labels, pink adhesive film or black CFRP substrate.

With such specific requirements, we proposed to add another layer of clustering over the segmented superpixels to binarize the labels of superpixels into pink or black. The proposed superpixels clustering methodology is consists of the following two steps: (i) segment an image using the superpixel-based image segmentation techniques to form over-segmentations, and then (ii) group the superpixels via a clustering algorithm, such as the simplest k-means, into 2 groups according to the similarity of those superpixels.

Note that the second step is working on the *superpixels* rather than *single pixels*. To represent each superpixel, the intuitive choice is the average value of pixel members therein that superpixel, the weighted average can also be considered based on the distance from

each pixel member to the centroid.

In the implementation, the proposed baseline approach, superpixel clustering methodology, is very flexible: the choice of superpixels-based image segmentation algorithm in step 1 and the final clustering algorithm in step 2 can be any proper combinations. For experiments in Section 4.4, the superpixels with clear and rational boundaries are picked to continue step 2 and are clustered into two groups.

4.3 Proposed Method – RG-filter

In this section, based on the visual observation and during image data collection and exploratory data analysis, a novel yet simple image segmentation method is proposed coming out of the adaptive thresholding mechanism. It is called RG-filter which labels pixels according to the relative magnitude of different color components, red (R) component and green (G) component, in a thresholding style.

Recall that thresholding is used to create a binary image from a grayscale image. It is the simplest way to segment objects from a background. Thresholding algorithms implemented in $scikit\_image$ in Python can be separated into two categories:

1. Histogram-based. The histogram of the pixels' intensity is used and certain assumptions are made on the properties of this histogram.

2. Local. Only the neighboring pixels are used to process a pixel. These algorithms often require more computation time.

The key difference between those thresholding methods is the way of identifying the threshold value. However, as a dimension deduction process, the information in colorful images will lose a lot of information when transferred to the grayscale images.

To overcome the color information loss during image processing and maximize the available information, the RGB components are observed closely during image data collection. When taking photos on the CFRP panels, the camera can provide a real-time strength

profile of each light component in a given location specified by a probe. It is observed that when the probe is put on the apparent pink adhesive film region, the R component usually has a larger value than the G component. While on the obvious black CFRP substrate region, quite the opposite. The blue component has no clear tendency over different regions. Thus, the following pixel labeling rule is proposed based on the relative value between R and G components:

$$X^* = \begin{cases} pink(\text{“1”}) & \text{if } \alpha X[R] + \beta > X[G], \\ black(\text{“0”}) & \text{if } \alpha X[R] + \beta \leq X[G] \end{cases} \tag{4.1}$$

where X^* is the binary label of a pixel, either pink (“1”) or black (“0”), $X[R]$ and $X[G]$ are the R and G component at that pixel respectively. The tuning parameters, multiplicative coefficient α and offset β, are used to adjust the filter according to the environment, such as lighting conditions. For example, when $\alpha = 1$ and $\beta = 0$, the relationship will be simply comparing the raw values of R and G components.

In real applications, the tuning parameters, multiplicative coefficient α and offset β, can be adjusted according to visual observation or be optimized automatically if the true pixel label is available for training.

4.4 Case Study – Experiments on CFRP Images

In this section, to compare the performance of the existing image segmentation methods, baseline method, and proposed method, image segmentation experiments are conducted on the example raw image in Figure 4.5.

In this experiment, pixel labeling is done first via image segmentation such as existing algorithms, baseline method, or the proposed method, and then, binary pixel pairing is conducted to identify the failure mode according to the aforementioned rule in Table 4.1. In detail, the pixel on both faces of the specimen pair will be labeled as either pink adhesive film or black CFRP substrate. Recall that there are 3 failure modes for the adhesive bond-

ing on the composite material, adherent (substrate) failure, cohesive failure, and adhesive failure. The intuitive visual presentation of the 3 failure modes on the specimen pairs is black to black, pink to pink, and black to pink (or pink to black). After identifying the failure mode of each pixel pair location, the failure mode distribution and proportions will be identified accordingly.

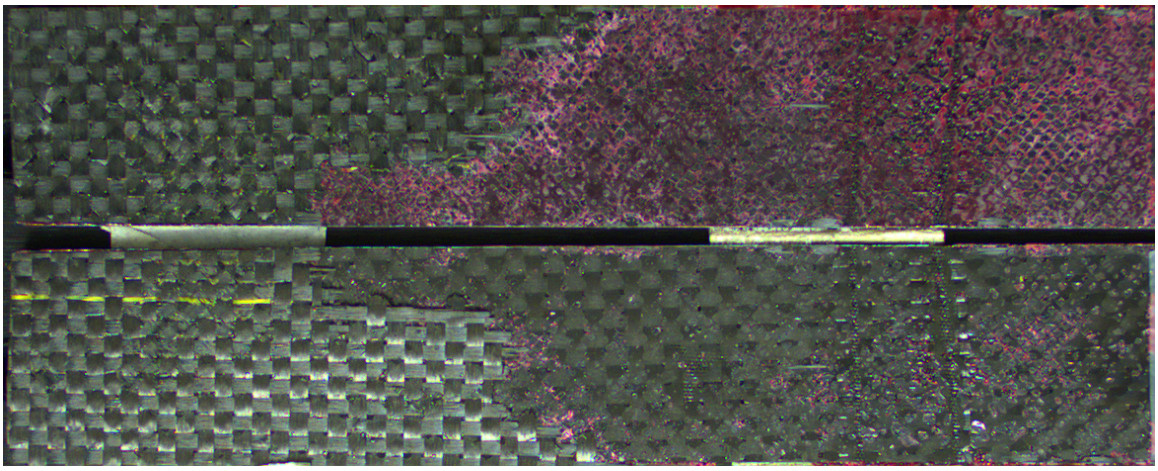

Figure 4.5: Raw image data used as an example for image segmentation experiments.

4.4.1 Image Segmentation Experiments on Existing Methods

Figure 4.6 shows the pixel-labeling results of several popular global thresholding methods, including the Isodata thresholding, Li thresholding, Mean thresholding, Minimum error thresholding, Otsu's thresholding, Triangle thresholding, and Yen thresholding. For this type of method, the key is identifying the threshold value. The local thresholding method is also conducted on our image data. Figure 4.7 shows the comparison of pixel-labeling results of Otsu's global thresholding and adaptive thresholding/local thresholding.

From Figure 4.6 and Figure 4.7, it can be seen that those popular thresholding methods cannot segment our image data properly, but the brightness dominates the segmentation, no matter global thresholds or local thresholds. The reason could be the information loss during the compression from RGB color images to grayscale images. Grayscale is a range of monochromatic shades from black to white, which represents the brightness of the pixel

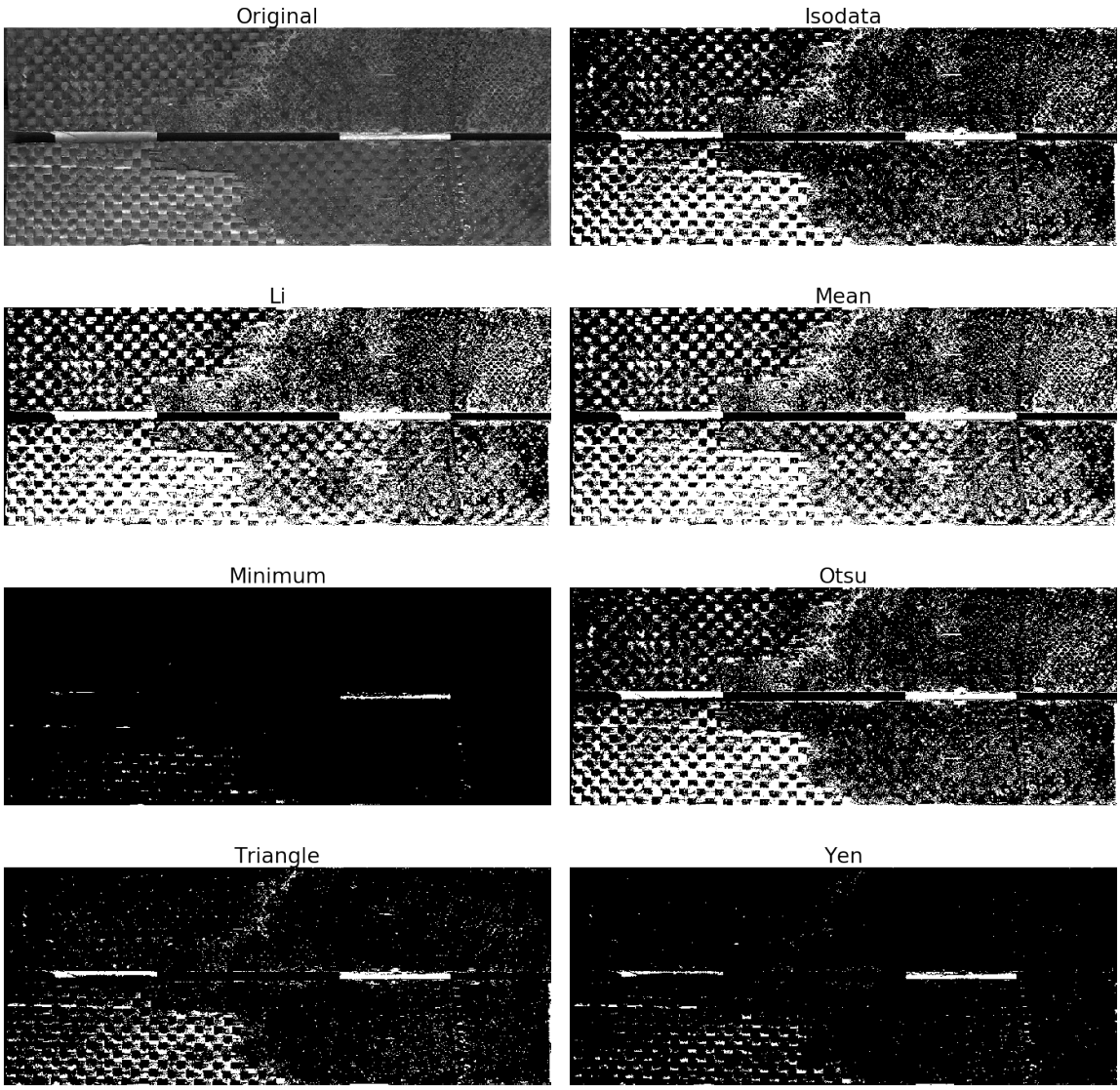

Figure 4.6: Comparison of pixel-labeling results of several global thresholding methods, Isodata, Li, Mean, Minimum error, Otsu, Triangle, and Yen.

by a single channel without color information. Since those thresholding methods usually work on 1D grayscale data, the loss of color information during compressions, such as the relative values of R, G, and B channels is a common issue. Due to the unsatisfactory performance on pixel labeling, these thresholding algorithms are not moved forward to the binary pixel-pairing step.

Figure 4.8 shows the pixel-labeling results of the simple K-means algorithm with $K = 2$. From the figure to the bottom, it can be seen that due to the strong reflection, the brighter

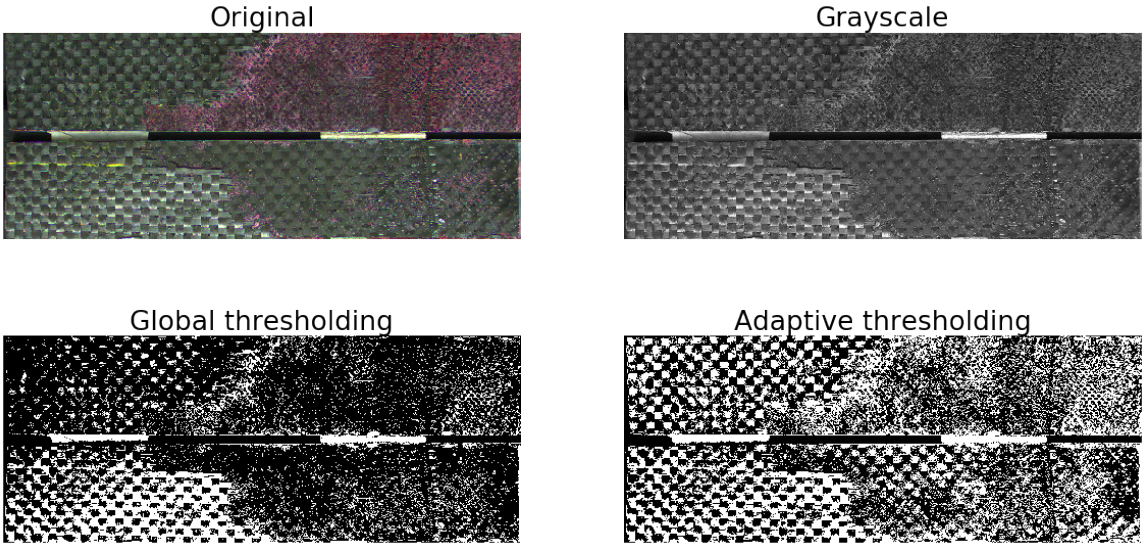

Figure 4.7: Pixel-labeling results of the Otsu's global thresholding and adaptive thresholding/local thresholding.

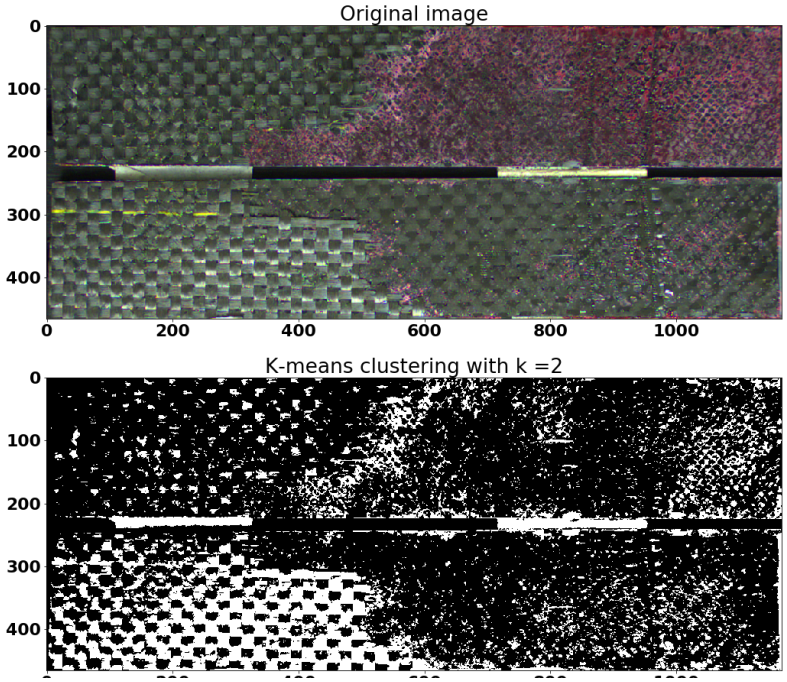

Figure 4.8: Pixel-labeling result of simple K-means algorithm with $K = 2$.

pixels in the bottom left region are classified into different groups dominated by the texture blocks of carbon fiber. With the naked eye, we can see that though the brightness in that region varies apparently with the texture, that region is actually homogeneous CFRP substrate with little adhesive film. Also, the K-means algorithm is implemented to 3D RGB

data without location information. Like the drawback of many image processing algorithms, the matrix-like image data will be expanded and tiled into a multiple-dimensional band in the preprocessing, where the location information is lost. In summary, the image segmentation results of K-means are not satisfying due to the domination of brightness caused by strong reflection and the loss of location information.

Figure 4.9 shows the pixel-labeling results of 4 popular algorithms: Felzenszwalb's, SLIC, Quickshift, and Compact Watershed. From the segmentation results, it can be seen that the Quickshift method and Compact Watershed fail to segment our image data rationally. While Felzenswalb's method and SLIC method seem to identify the region boundaries pretty well. Even so, as aforementioned, the problem associated with these segmentation methods is that they segment the image into many different regions with distinct labels. Roughly speaking, the more the segmentation, the finer the detected boundary. While in our cases, we must relabel those superpixels with binary labels, pink adhesive film, or black CFRP substrate.

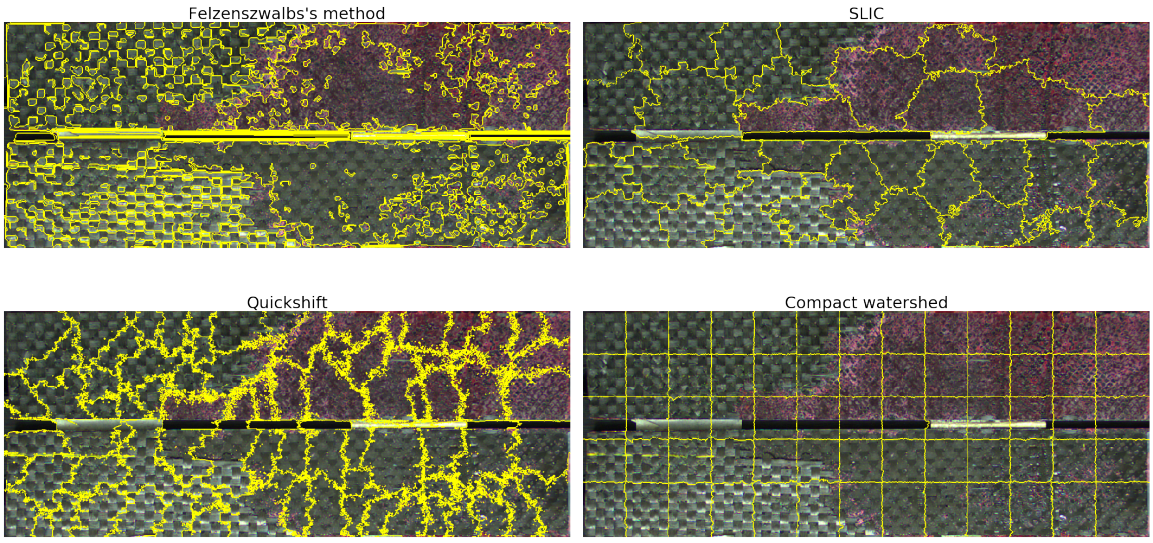

Figure 4.9: Pixel-labeling results of 4 popular algorithms: Felzenszwalb's method, SLIC, Quickshift, and Compact Watershed.

This is also the motivation for proposing the baseline method, the superpixel clustering method, where an extra step clustering is conducted to binarize superpixels. Based on the

pixel-labeling performance, the superpixels segmented by Felzenswalb's method and the SLIC method are moved forward to the step of superpixels binarization.

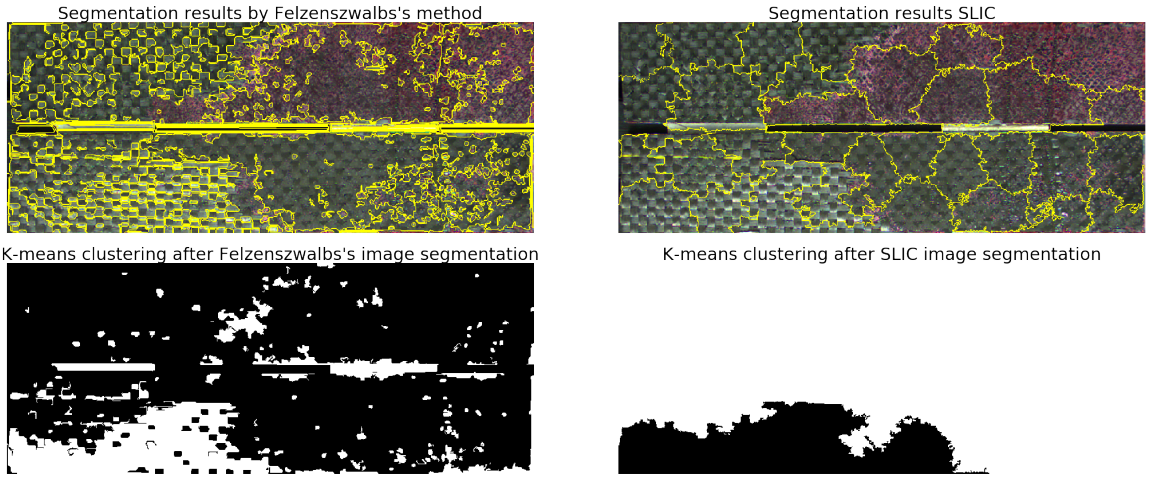

Figure 4.10: Pixel-labeling results of the baseline approach (figures to the bottom), where the superpixels are obtained from Felzenszwalbs's method and SLIC method (figures to the top), and the clustering algorithm in step is the k-means clustering with $K = 2$.

Figure 4.10 shows the performance of the proposed baseline approach, superpixel clustering methodology. The figures on the top row show superpixels obtained from Felzenszwalbs's method and the SLIC method. In the second step, the K-means algorithm with $K = 2$ is adopted to binarize these superpixels. The figures on the bottom row show the binarized superpixels, also the final pixel-labeling results. Unfortunately, in the second step, the binarized superpixels failed to represent the pink adhesive and black CFRP substrate satisfyingly, where the brightness rather than the color dominates the segmentation again.

The potential causes of the poor performance of the baseline approach can be multiple. First, the strong reflection in data collection, which is similar to the thresholding-based pixel labeling algorithms which deal with grayscale images. Second, though in the second step, the K-means algorithm works directly on the RGB color superpixels, each superpixel is represented by the average value of pixel members inside it. This compresses the information of pixels inside a superpixel. As a result, the brightness, a linear combination of R, G, and B components, also has the chance to dominates over the clustering.

4.4.2 Image Segmentation Experiments on Proposed method – GR-filter

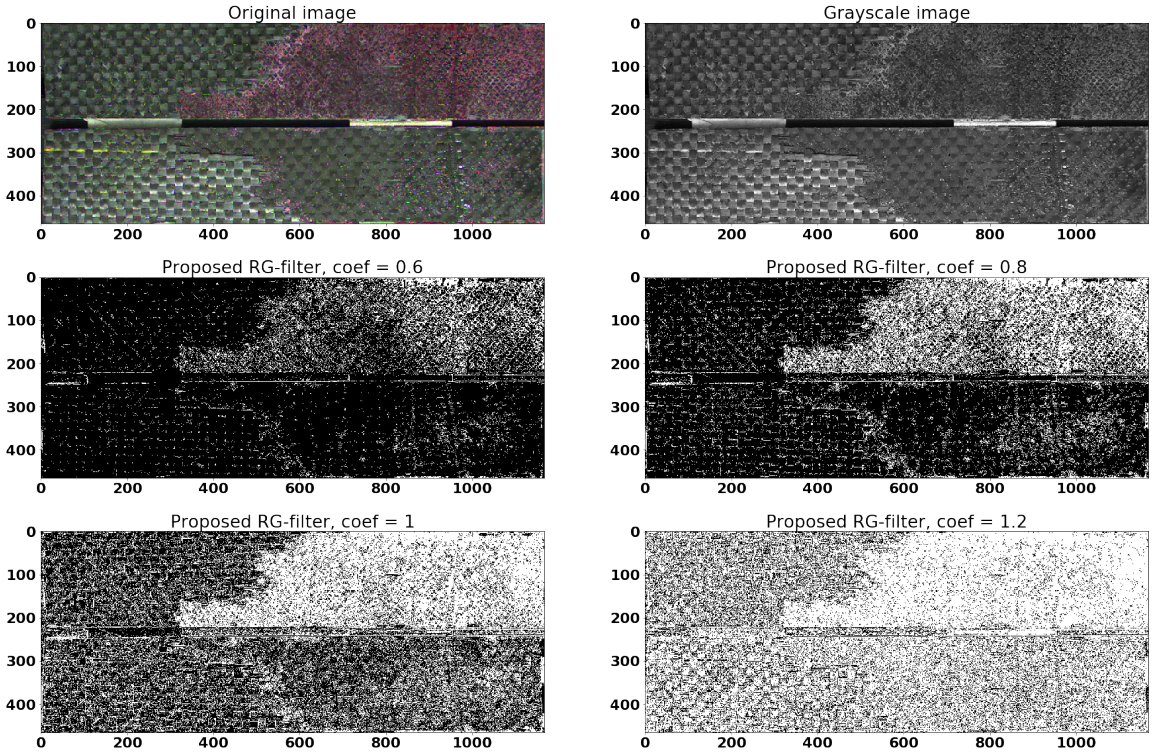

Figure 4.11: Pixel-labeling results of the proposed RG-filter with different coefficients: $\alpha = \{0.6, 0.8, 1.0, 1.2\}$.

Figure 4.11 shows the pixel-labeling results of the proposed RG-filter with a sequence of different coefficients: $\alpha = \{0.6, 0.8, 1.0, 1.2\}$. On the binarized images, the white pixels correspond to the pink adhesive film on the original image, and the black pixels correspond to the black CFRP substrate on the original image. It can be seen that with the coefficient increasing, the algorithm tends to label more pixels as white (pink adhesive film). Among them, when $\alpha = 0.8$, the pixel-labeling results coincide with the visual observation on the original raw image well. For the first time in this study, the segmentation results are not dominated by brightness but color information. The reason for the satisfying performance is straightforward: unlike working on compressed grayscale data, the proposed algorithm labels pixels directly based on the RGB information where the relative magnitude of different color channels is taken into consideration.

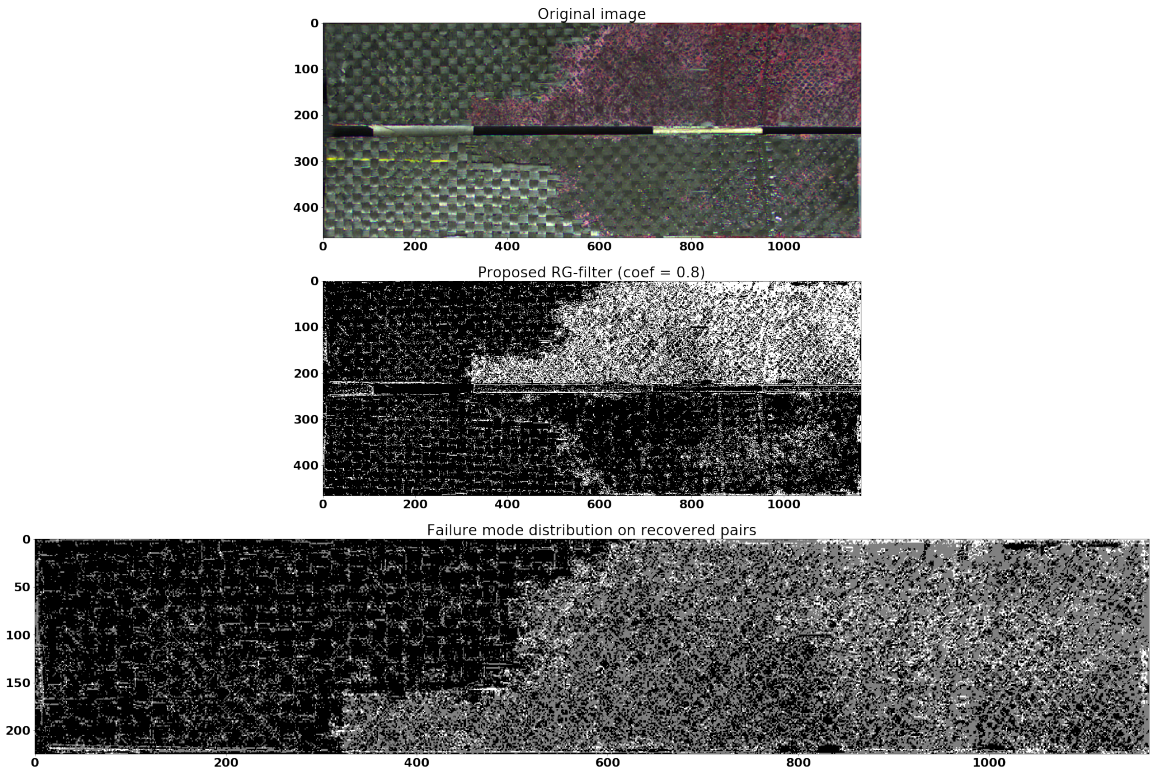

Figure 4.12: Final results of binary pixel-pairing: failure mode distribution on the recovered CFRP pairs (A face flip up). The three colors indicate 3 failure modes respectively.

Figure 4.12 shows the final results of the image segmentation when using the optimal coefficient value, $\alpha = 0.8$. Recall that after labeling each pixel on two faces from CFRP pairs originally bonded together, we have to pair these binary pixels by flipping one face to match the other face according to the rule aforementioned. Therefore, on the bottom figure in Figure 4.12, the black region corresponds to the black-to-black pixel pairs which represent the adherent (substrate) failure. The white region corresponds to the white-to-white pixel pairs which represent the cohesive failure. And the gray region corresponds to the whit-to-black pixel pairs which indicate the adhesive failure. Besides, the proportion of the 3 failure modes are $adherent : adhesive : cohesive = 0.535 : 0.410 : 0.054$. As aforementioned, the failure mode distribution and proportions are very crucial in composite material analysis. Different failure modes indicate different weak links during the bonding of composite material, which shed some light on improving the bonding quality of composite material.

4.5 Conclusion and Discussion

In this study, a simple yet very effective unsupervised image segmentation method, called RG-filter, is proposed to segment engineering images with no significant contrast between foreground and background for a material testing application. The project is to find the failure mode distribution and proportion over CFRP specimens after DCB testing by implementing unsupervised image segmentation. With the challenge of limited data size, imperfect data quality, unreachable binary true label, we first proposed a baseline method called the superpixels clustering algorithm where we add another layer of clustering over the segmented superpixels to binarize their labels. Then, we developed the RG-filter which thresholding the pixels according to the relative magnitude of the R channel and G channel of the RGB image. To test the performance of the existing image segmentation and proposed algorithm on our CFRP image data, we conducted a series of experiments over an example specimen. Comparing all the pixel labeling results, the proposed RG-filter outperforms the others to be the most recommended one. In addition, it is super intuitive and efficient in computation. The proposed RG-filter can help to analyze the failure mode distribution and proportion on the surface of composite material after destructive DCB testing. The result can help engineers better understand the weak link during the bonding of composite materials, which may provide guidance on how to improve the joining of structures during aircraft maintenance. Also, if we can predict it from other variables, the destructive DCB testing can be avoided, a lot of time and money can be saved.

The proposed RG-filter is suitable for segment images where the foreground and background have no significant contrast, and the type of segmentation labels is two. If there are more than 2 types of labels required, multiple filters can be developed according to the characteristic of the image data. However, with the number of label types increase, identifying the filter can be complicated, this is the limitation of the proposed RG-filter. In this case, other image segmentation techniques can be involved, see Table 4.2.

Another limitation of the proposed RG-filter is that the coefficient and offset need to be adjusted manually according to the specialist's visual observation currently since the true label is not available. In the future, the parameter tuning of the proposed RG-filter algorithm can be improved by formulating some optimization problems. Also, for the baseline approach, superpixel clustering algorithm, the second step can be modified to improve the clustering performance, such as involving the affinity propagation algorithm.

CHAPTER 5
SUMMARY AND FUTURE RESEARCH

5.1 Summary of Original Contributions

This dissertation contributes to the area of information extraction from messy data in real-words applications, especially when the data is functional data with multiple uncertainties, incomplete data, and unlabeled images. Systematic methodologies were developed for functional effect quantification on functional noisy data, active learning style sequential decision-making strategy for incomplete clinical data, and unsupervised image segmentation for surface characterization in composite materials. This is an interdisciplinary research area. We have developed novel methodologies by integrating advanced statistics, machine learning and engineering domain knowledge. The original contributions of this dissertation include the following aspects:

In Chapter 2, a general two-step procedure is proposed to quantify the effects of a certain treatment on the spectral signals subjecting to multiple uncertainties for an engineering application which involves materials treatment for aircraft maintenance. With this procedure, two types of uncertainties in the spectral signals, offset shift and multiplicative error, are carefully addressed. In the two-step procedure, a novel optimization problem is formulated to estimate the representative template spectrum first, and then another optimization problem is formulated to obtain the pattern of modification g that reveals how the treatment affects the shape of the spectral signal, as well as a vector $\boldsymbol{\delta}$ that describes the degree of change caused by different treatment magnitudes. The effectiveness of the proposed method is validated in a simulation study. Furtherly, in a real case study, the proposed method is used to investigate the effect of plasma exposure on the FTIR spectra. As a result, the proposed method effectively identifies the pattern of modification under

uncertainties in the manufacturing environment, which matches the knowledge of the affected chemical components by the plasma treatment. And the recovered magnitude of modification provides guidance in selecting the control parameter of the plasma treatment.

In Chapter 3, an active learning-based multistage sequential decision-making model is proposed to assist doctors and patients to make cost-effective treatment recommendations when some clinical data are more expensive or time-consuming to collect than other laboratory data. The main idea is to formulate the incomplete clinical data into a multistage decision-making model where the doctors can make diagnostics decisions sequentially in these stages, and actively collect only the necessary examination data from certain patients rather than all. There are two novelties in estimating parameters in the proposed model. First, unlike the existing ordinal logistic regression model which only models a single stage, a multistage model is built by maximizing the joint likelihood function for all samples in all stages. Second, considering that the data in different stages are nested in a cumulative way, it is assumed that the coefficients for common features in different stages are invariant. Compared with the baseline approach that models each stage individually and independently, the proposed multistage model with common coefficients assumption has significant advantages. It reduces the number of variables to estimate significantly, improves the computational efficiency, and makes the doctors feel intuitive by assuming that newly added features will not affect the weights of existing ones. In a simulation study, the relative efficiency of the proposed method with regards to the baseline approach is 162% to 1,938%, proving its efficiency and effectiveness soundly. Then, in a real case study, the proposed method estimates all parameters very efficiently and reasonably.

In Chapter 4, a simple yet very effective unsupervised image segmentation method, called RG-filter, is proposed to segment engineering images with no significant contrast between foreground and background for a material testing application. With the challenge of limited data size, imperfect data quality, unreachable binary true label, we developed the RG-filter which thresholding the pixels according to the relative magnitude of the R

channel and G channel of the RGB image. To test the performance of the existing image segmentation and proposed algorithm on our CFRP image data, we conducted a series of experiments over an example specimen. Comparing all the pixel labeling results, the proposed RG-filter outperforms the others to be the most recommended one. in addition, it is super intuitive and efficient in computation. The proposed RG-filter can help to analyze the failure mode distribution and proportion on the surface of composite material after destructive DCB testing. The result can help engineers better understand the weak link during the bonding of composite materials, which may provide guidance on how to improve the joining of structures during aircraft maintenance. Also, it can be crucial data when modeling together with some downstream data as a whole. And if we can predict it from other variables, the destructive DCB testing can be avoided, a lot of time and money can be saved.

The proposed two-step functional effect quantification technique is suitable and promising to quantify the effect of a large class of surface treatments apart from the plasma treatment. The pattern of modification $\mathbf{g}$ reveals the general effect pattern of a certain surface treatment in a range of treatment magnitude, providing a new way to understand the intrinsic reasons behind the improvement of surface quality. Recall that the surface treatment methods have been well-developed, including thermal treatment, wet chemical or electrochemical oxidation, plasma treatment, gas-phase oxidation, coating treatment, etc., applying and extending this method to solve more problems in the manufacturing industry is a direction for our further research. Also, the method is applicable to analyze the data obtained from a wide range of spectral measurements, including ultraviolet-visible spectroscopy (UV-Vis) [38], X-ray diffraction (XRD) [39], Raman spectroscopy [40, 41] etc., when the background noise leads to uncertain offset and the uncertain signal level results in the multiplicative error. Typically, these uncertainties are of greater magnitude in real manufacturing environments than in lab conditions, due to the inexperienced operators and the uncontrolled surroundings. Therefore, the analytic methodology proposed in this article

also helps to broaden the application scope of portable spectrometers, such as the handheld FTIR devices.

The proposed multistage decision-making model is also applicable to a broad range of decision-making scenarios beyond the diagnosis process in the healthcare area. The proposed algorithm adopts the active learning idea, which drives the decision-maker to sequentially collect the necessary information only rather all collect all possible information at once. This is definitely energy-saving, time-saving, and economically effective.

The proposed unsupervised image segmentation algorithm, RG-filter, is crucial to the downstream work. After figuring out the distribution and proportion of failure models on the CFRP specimen, people can better understand the weak link during the bonding of composite material, which may give some clue on improving the joining and maintenance on aircraft. More importantly, the segmentation results can be crucial data when modeling together with some downstream data as a whole. Once we can predict the failure mode proportion and distribution directly from some surface characterizing variables, the expensive, time-consuming, and destructive DCB test can be avoided, and naturally, a huge amount of time and money will be saved.

5.2 Future Research

Below is a list of important topics that are based on our research in this dissertation and worth further investigation:

- New methodologies are needed under the scenario when the pattern of modification g is different for distinct levels of surface treatment. Note that the proposed two-step procedure for quantifying the functional effect on noisy functional spectra study assumes that the pattern of modification g is identical under all levels of treatment.To saftisy the future goal, we can modify the represenation of treatment effect from $\delta_i \boldsymbol{g}$ to $\delta_i \boldsymbol{g}_i$ where $\boldsymbol{g}_i$ is the pattern of modification at treatment level i. The algorithms for parameter estimation should be developed accordingly.

- Extend the proposed multistage decision-making model to satisfy more real-world cases with special requirements. Note that the proposed model didn't involve the estimation of overall clinical relevance cost, didn't customize the penalty for different types of misclassification, and cannot enable variable selection. In the future, we can modify our proposed method in multiple ways to satisfy these special needs. For example, in some the cases, the clinical relevance cost, such as the examination-related financial cost and emotional cost caused by patients' unwillingness, are specified and of interest. In this case, the objective can be minimizing all the costs, including negative likelihood and clinical relevance cost. Also, in some cases, for the doctor's decision-making in the real world, the penalty for different types of mistakes can be case-by-case and vary a lot. For example, false-positive detection may lead to unnecessary invasive procedures or just excess care, false-negative detection may result in missing life-saving chances or just a longer diagnosing process. For such cases, we can modify the objective function by specifying the weights of penalties on different types of miss classification. Besides, we can add L_1 regularization term to the objective function to realize the variable selection.

- Automize the filter parameter optimization and enable multiple-level filtering. Note that the proposed RG-filter is specially designed for the CFRP images with binary labels and no significant contrast between foreground and background. And the coefficient and offset parameters for the filter are chosen based on visual observation. In the future, we can artificially label some figures as ground truth to train a supervised filter where the parameters can be solved over optimization problems. Also, multiple level filters can be explored in a proper image dataset.

From the point of view of data analytics methodologies, my future research involves the development of engineering-driven data analytics methodologies for information extraction. The high-dimensional, incomplete, heterogeneous, unstructured data and diversity of real-world specific requirements make this a rich topic with numerous potential avenues of

investigation. In particular, my research agenda is not limited to develop pure data-driven models or machine learning techniques but also encompasses raw data preprocessing and domain knowledge. I would like to continue my research to develop a broader range of information extraction methodologies to decode the information buried in noise, tackle the special needs of unstructured data, and let the data tell the story.

REFERENCES

[1] H. Kang, "The prevention and handling of the missing data," *Korean journal of anesthesiology*, vol. 64, no. 5, p. 402, 2013.

[2] J. Chen, S. Mak, V. R. Joseph, and C. Zhang, "Adaptive design for gaussian process regression under censoring," *arXiv preprint arXiv:1910.05452*, 2019.

[3] J. Chen, Z. Chen, C. Zhang, and C. Wu, "Apik: Active physics-informed kriging model with partial differential equations," *arXiv preprint arXiv:2012.11798*, 2020.

[4] X. Yue, K. Wang, H. Yan, J. G. Park, Z. Liang, C. Zhang, B. Wang, and J. Shi, "Generalized wavelet shrinkage of inline raman spectroscopy for quality monitoring of continuous manufacturing of carbon nanotube buckypaper," *IEEE Trans. Autom. Sci. Eng.*, vol. 14, no. 1, pp. 196–207, 2017.

[5] J. Cornel, C. Lindenberg, and M. Mazzotti, "Quantitative application of in situ ATR-FTIR and raman spectroscopy in crystallization processes," *Ind. Eng. Chem. Res.*, vol. 47, no. 14, pp. 4870–4882, 2008.

[6] E. Lazzari, T. Schena, M. C. A. Marcelo, C. T. Primaz, A. N. Silva, M. F. Ferrão, T. Bjerk, and E. B. Caramão, "Classification of biomass through their pyrolytic bio-oil composition using FTIR and PCA analysis," *Ind. Crops Prod.*, vol. 111, pp. 856–864, 2018.

[7] P. Barmpalexis, A. Karagianni, I. Nikolakakis, and K. Kachrimanis, "Artificial neural networks (ANNs) and partial least squares (PLS) regression in the quantitative analysis of cocrystal formulations by Raman and ATR-FTIR spectroscopy," *J. Pharm. Biomed. Anal.*, vol. 158, pp. 214–224, 2018.

[8] V. Tafintseva, V. Shapaval, M. Smirnova, and A. Kohler, "Extended multiplicative signal correction for FTIR spectral quality test and pre-processing of infrared imaging data," *J. Biophotonics*, 2019.

[9] Å. Rinnan, F. Van Den Berg, and S. B. Engelsen, "Review of the most common preprocessing techniques for near-infrared spectra," *Trac-Trend Anal. Chem.*, vol. 28, no. 10, pp. 1201–1222, 2009.

[10] N. K. Afseth and A. Kohler, "Extended multiplicative signal correction in vibrational spectroscopy, a tutorial," *Chemometrics Intell. Lab.*, vol. 117, pp. 92–99, 2012.

[11] H. Martens, J. P. Nielsen, and S. B. Engelsen, "Light scattering and light absorbance separated by extended multiplicative signal correction. Application to near-infrared

transmission analysis of powder mixtures," *Anal. Chem.*, vol. 75, no. 3, pp. 394–404, 2003.

[12] J. Schmitt, M. Beekes, A. Brauer, T. Udelhoven, P. Lasch, and D. Naumann, "Identification of scrapie infection from blood serum by Fourier transform infrared spectroscopy," *Anal. Chem.*, vol. 74, no. 15, pp. 3865–3868, 2002.

[13] A. Kohler, V. Høst, and R. Ofstad, "Image analysis of particle dispersions in microscopy images of cryo-sectioned sausages," *Scanning*, vol. 23, no. 3, pp. 165–174, 2001.

[14] J. Ramsay, "Functional data analysis (encyclopedia of statistics in behavioral science)," in. Wiley Online Library, 2005.

[15] G. Lahoti, J. Chen, X. Yue, H. Yan, C. Ranjan, Z. Qian, C. Zhang, and B. Wang, "Image decomposition-based sparse extreme pixel-level feature detection with application to medical images," *IISE Transactions on Healthcare Systems Engineering*, no. just-accepted, pp. 1–32, 2021.

[16] B. Lauren and L. Lee, "Perceptual information processing system. paravue inc," *US Patent Application*, vol. 10, no. 618,543, 2003.

[17] P. Bassan, "Light scattering during infrared spectroscopic measurements of biomedical samples," Ph.D. dissertation, The University of Manchester (United Kingdom), 2011.

[18] V. Ţucureanu, A. Matei, and A. M. Avram, "FTIR spectroscopy for carbon family study," *Crit. Rev. Anal. Chem.*, vol. 46, no. 6, pp. 502–520, 2016.

[19] S. H. Han, H. J. Oh, and S. S. Kim, "Evaluation of fiber surface treatment on the interfacial behavior of carbon fiber-reinforced polypropylene composites," *Compos. B. Eng.*, vol. 60, pp. 98–105, 2014.

[20] M. Sharma, S. Gao, E. Mäder, H. Sharma, L. Y. Wei, and J. Bijwe, "Carbon fiber surfaces and composite interphases," *Compos. Sci. Technol.*, vol. 102, pp. 35–50, 2014.

[21] R. M. Kakhki, "A review to recent developments in modification of carbon fiber electrodes," *Arab. J. Chem.*, vol. 12, pp. 1783–1794, 2014.

[22] C. Sun, J. Min, J. Lin, and H. Wan, "Effect of atmospheric pressure plasma treatment on adhesive bonding of carbon fiber reinforced polymer," *Polymers*, vol. 11, no. 1, p. 139, 2019.

[23] S. Tiwari and J. Bijwe, "Surface treatment of carbon fibers-a review," *Proc. Technol.*, vol. 14, pp. 505–512, 2014.

[24] L. J. Waters, C. V. Finch, A. M. H. Bhuiyan, K. Hemming, and J. C. Mitchell, "Effect of plasma surface treatment of poly (dimethylsiloxane) on the permeation of pharmaceutical compounds," *J. Pharm. Anal.*, vol. 7, no. 5, pp. 338–342, 2017.

[25] O. J. Kwon, S. Tang, S. W. Myung, N. Lu, and H. S. Choi, "Surface characteristics of polypropylene film treated by an atmospheric pressure plasma," *Surf. Coat. Tech.*, vol. 192, no. 1, pp. 1–10, 2005.

[26] S. M. Mukhopadhyay, P. Joshi, S. Datta, J. Zhao, and P. France, "Plasma assisted hydrophobic coatings on porous materials: Influence of plasma parameters," *J. Phys. D: Appl. Phys.*, vol. 35, no. 16, p. 1927, 2002.

[27] E. Liston, L. Martinu, and M. Wertheimer, "Plasma surface modification of polymers for improved adhesion: A critical review," *J. Adhes. Sci. Technol.*, vol. 7, no. 10, pp. 1091–1127, 1993.

[28] W. Haynes, E. Melvin, J. M. Locke, C. Glass, and F. Senti, "Certain factors affecting the infrared spectra of selected microorganisms," *Appl. Microbiol.*, vol. 6, no. 5, p. 298, 1958.

[29] J. Chen, S. Mak, V. R. Joseph, and C. Zhang, "Function-on-function kriging, with applications to 3D printing of aortic tissues," *arXiv preprint arXiv:1910.01754*, 2019.

[30] G. H. Golub, "Some modified matrix eigenvalue problems," *SIAM Rev.*, vol. 15, no. 2, pp. 318–334, 1973.

[31] G. H. Golub and C. F. Van Loan, "Matrix computations," in. JHU press, 2012, vol. 3, pp. 76–79.

[32] M. Dhanoa, S. Lister, R. Sanderson, and R. Barnes, "The link between multiplicative scatter correction (msc) and standard normal variate (snv) transformations of nir spectra," *J. Near Infrared Spec.*, vol. 2, no. 1, pp. 43–47, 1994.

[33] B. Van der Bruggen, "Chemical modification of polyethersulfone nanofiltration membranes: A review," *J. Appl. Polym. Sci.*, vol. 114, no. 1, pp. 630–642, 2009.

[34] B. Labs, "Contact angle measurements and surface analysis of atmospheric pressure plasma treated polypropylene," BTG Labs, Tech. Rep., 2013.

[35] D. Merck KGaA, Germany and/or its affiliates, *IR Spectrum Table & Chart*, https://www.sigmaaldrich.com/technical-documents/articles/biology/ir-spectrum-table.html, 2019.

[36] J. Comyn, L. Mascia, G. Xiao, and B. Parker, "Plasma-treatment of polyetheretherketone (peek) for adhesive bonding," *Int. J. Adhes. Adhes.*, vol. 16, no. 2, pp. 97–104, 1996.

[37] Thermo Fisher Scientific, Inc., *Spectra data online (FTIR/Ramen search)*, http://ftirsearch.com/, 2001.

[38] L. Sooväli, E. I. Rõõm, A. Kütt, I. Kaljurand, and I. Leito, "Uncertainty sources in UV-Vis spectrophotometric measurement," *Accred. Qual. Assur.*, vol. 11, no. 5, pp. 246–255, 2006.

[39] B. Sun, H. Yu, Y. Yang, H. Li, C. Zhai, D. Qian, and M. Chen, "New complete assignment of X-ray powder diffraction patterns in graphitic carbon nitride using discrete Fourier transform and direct experimental evidence," *Phys. Chem. Chem. Phys.*, vol. 19, no. 38, pp. 26 072–26 084, 2017.

[40] J. Liu, J. Sun, X. Huang, G. Li, and B. Liu, "Goldindec: A novel algorithm for Raman spectrum baseline correction," *Appl. Spectrosc.*, vol. 69, no. 7, pp. 834–842, 2015.

[41] K. H. Liland, A. Kohler, and N. K. Afseth, "Model-based pre-processing in Raman spectroscopy of biological samples," *J. Raman Spectrosc.*, vol. 47, no. 6, pp. 643–650, 2016.

[42] Dr. Piyush Ranjan, *Best CBD Stone Treatment in DelhI*, https://www.drpiyushranjan.com/cbd-stone-treatment-in-delhi/, 2020.

[43] J. Chen, Y. Xie, K. Wang, C. Zhang, M. A. Vannan, B. Wang, and Z. Qian, "Active image synthesis for efficient labeling," *IEEE transactions on pattern analysis and machine intelligence*, 2020.

[44] D. B. Rubin, "An overview of multiple imputation," in *Proceedings of the survey research methods section of the American statistical association*, Citeseer, 1988, pp. 79–84.

[45] A. P. Dempster, N. M. Laird, and D. B. Rubin, "Maximum likelihood from incomplete data via the em algorithm," *Journal of the Royal Statistical Society: Series B (Methodological)*, vol. 39, no. 1, pp. 1–22, 1977.

[46] B. Settles, "Active learning literature survey," 2009.

[47] P. McCullagh, "Regression models for ordinal data," *Journal of the Royal Statistical Society: Series B (Methodological)*, vol. 42, no. 2, pp. 109–127, 1980.

[48] H. S. Kim, "Topics in ordinal logistic regression and its applications," Ph.D. dissertation, Texas A&M University, 2004.

[49] G. Watson, "Generalized linear models (p. mccullagh and ja nelder)," *SIAM Review*, vol. 28, no. 1, pp. 128–130, 1986.

[50] F. Olsson, "A literature survey of active machine learning in the context of natural language processing," 2009.

[51] A. Agresti and C. Tarantola, "Simple ways to interpret effects in modeling ordinal categorical data," *Statistica Neerlandica*, vol. 72, no. 3, pp. 210–223, 2018.

[52] A. Agresti, *Categorical data analysis*. John Wiley & Sons, 2003, vol. 482.

[53] R. H. B. Christensen, "Cumulative link models for ordinal regression with the r package ordinal," *Submitted in J. Stat. Software*, 2018.

[54] B. Ripley, B. Venables, D. M. Bates, K. Hornik, A. Gebhardt, D. Firth, and M. B. Ripley, "Package 'mass'," *Cran r*, vol. 538, pp. 113–120, 2013.

[55] T. W. Yee *et al.*, "The vgam package for categorical data analysis," *Journal of Statistical Software*, vol. 32, no. 10, pp. 1–34, 2010.

[56] Harrell Jr FE, *rms: Regression Modeling Strategies*, https://CRAN.R-project.org/package=rms/, 2018.

[57] P.-C. Bürkner, "Advanced bayesian multilevel modeling with the r package brms," *arXiv preprint arXiv:1705.11123*, 2017.

[58] M. Avriel, *Nonlinear programming: analysis and methods*. Courier Corporation, 2003.

[59] C. G. Broyden, J. E. Dennis Jr, and J. J. Moré, "On the local and superlinear convergence of quasi-newton methods," *IMA Journal of Applied Mathematics*, vol. 12, no. 3, pp. 223–245, 1973.

[60] C. Solomon and T. Breckon, *Fundamentals of Digital Image Processing: A practical approach with examples in Matlab*. John Wiley & Sons, 2011.

[61] A. AC09036782, *Standard test method for mode I interlaminar fracture toughness of unidirectional fiber-reinforced polymer matrix composites*. ASTM Internat., 2007.

[62] S. Hashemi, A. Kinloch, and J. Williams, "Corrections needed in double-cantilever beam tests for assessing the interlaminar failure of fibre-composites," *Journal of Materials Science Letters*, vol. 8, no. 2, pp. 125–129, 1989.

[63] G. Belingardi, V. Brunella, B. Martorana, and R. Ciardiello, "Thermoplastic adhesive for automotive applications," *Adhesives-Applications and Properties*, pp. 341–359, 2016.

[64] D. Comaniciu and P. Meer, "Mean shift: A robust approach toward feature space analysis," *IEEE Transactions on pattern analysis and machine intelligence*, vol. 24, no. 5, pp. 603–619, 2002.

[65] A. Vedaldi and S. Soatto, "Quick shift and kernel methods for mode seeking," in *European conference on computer vision*, Springer, 2008, pp. 705–718.

[66] M. Ester, H.-P. Kriegel, J. Sander, X. Xu, *et al.*, "A density-based algorithm for discovering clusters in large spatial databases with noise.," in *Kdd*, vol. 96, 1996, pp. 226–231.

[67] S. Beucher and F. Meyer, "The morphological approach to segmentation: The watershed transformation," *Mathematical morphology in image processing*, vol. 34, pp. 433–481, 1993.

[68] P. Neubert and P. Protzel, "Compact watershed and preemptive slic: On improving trade-offs of superpixel segmentation algorithms," in *2014 22nd international conference on pattern recognition*, IEEE, 2014, pp. 996–1001.

[69] W. Benesova and M. Kottman, "Fast superpixel segmentation using morphological processing," in *Conference on Machine Vision and Machine Learning*, 2014, pp. 67–1.

[70] P. Arbelaez, M. Maire, C. Fowlkes, and J. Malik, "Contour detection and hierarchical image segmentation," *IEEE transactions on pattern analysis and machine intelligence*, vol. 33, no. 5, pp. 898–916, 2010.

[71] X. Ren and J. Malik, "Learning a classification model for segmentation," in *Computer Vision, IEEE International Conference on*, IEEE Computer Society, vol. 2, 2003, pp. 10–10.

[72] P. F. Felzenszwalb and D. P. Huttenlocher, "Efficient graph-based image segmentation," *International journal of computer vision*, vol. 59, no. 2, pp. 167–181, 2004.

[73] L. Grady, "Random walks for image segmentation," *IEEE transactions on pattern analysis and machine intelligence*, vol. 28, no. 11, pp. 1768–1783, 2006.

[74] O. Veksler, Y. Boykov, and P. Mehrani, "Superpixels and supervoxels in an energy optimization framework," in *European conference on Computer vision*, Springer, 2010, pp. 211–224.

[75] M.-Y. Liu, O. Tuzel, S. Ramalingam, and R. Chellappa, "Entropy rate superpixel segmentation," in *CVPR 2011*, IEEE, 2011, pp. 2097–2104.

[76] Y. Zhang, R. Hartley, J. Mashford, and S. Burn, "Superpixels via pseudo-boolean optimization," in *2011 International Conference on Computer Vision*, IEEE, 2011, pp. 1387–1394.

[77] A. Humayun, F. Li, and J. M. Rehg, "The middle child problem: Revisiting parametric min-cut and seeds for object proposals," in *Proceedings of the IEEE International Conference on Computer Vision*, 2015, pp. 1600–1608.

[78] A. Levinshtein, A. Stere, K. N. Kutulakos, D. J. Fleet, S. J. Dickinson, and K. Siddiqi, "Turbopixels: Fast superpixels using geometric flows," *IEEE transactions on pattern analysis and machine intelligence*, vol. 31, no. 12, pp. 2290–2297, 2009.

[79] P. Buyssens, I. Gardin, and S. Ruan, "Eikonal based region growing for superpixels generation: Application to semi-supervised real time organ segmentation in ct images," *Irbm*, vol. 35, no. 1, pp. 20–26, 2014.

[80] F. Drucker and J. MacCormick, "Fast superpixels for video analysis," in *2009 Workshop on Motion and Video Computing (WMVC)*, IEEE, 2009, pp. 1–8.

[81] D. Tang, H. Fu, and X. Cao, "Topology preserved regular superpixel," in *2012 IEEE International Conference on Multimedia and Expo*, IEEE, 2012, pp. 765–768.

[82] R. Achanta, A. Shaji, K. Smith, A. Lucchi, P. Fua, and S. Süsstrunk, "Slic superpixels," Tech. Rep., 2010.

[83] F. Pedregosa, G. Varoquaux, A. Gramfort, V. Michel, B. Thirion, O. Grisel, M. Blondel, P. Prettenhofer, R. Weiss, V. Dubourg, *et al.*, "Scikit-learn: Machine learning in python," *Journal of machine learning research*, vol. 12, no. Oct, pp. 2825–2830, 2011.

[84] D. Weikersdorfer, D. Gossow, and M. Beetz, "Depth-adaptive superpixels,"

[85] J. Wang and X. Wang, "Vcells: Simple and efficient superpixels using edge-weighted centroidal voronoi tessellations," *IEEE Transactions on pattern analysis and machine intelligence*, vol. 34, no. 6, pp. 1241–1247, 2012.

[86] J. Papon, A. Abramov, M. Schoeler, and F. Worgotter, "Voxel cloud connectivity segmentation-supervoxels for point clouds," in *Proceedings of the IEEE conference on computer vision and pattern recognition*, 2013, pp. 2027–2034.

[87] Z. Li and J. Chen, "Superpixel segmentation using linear spectral clustering," in *Proceedings of the IEEE Conference on Computer Vision and Pattern Recognition*, 2015, pp. 1356–1363.

[88] C. Conrad, M. Mertz, and R. Mester, "Contour-relaxed superpixels," in *International Workshop on Energy Minimization Methods in Computer Vision and Pattern Recognition*, Springer, 2013, pp. 280–293.

[89] M. Van den Bergh, X. Boix, G. Roig, B. de Capitani, and L. Van Gool, "Seeds: Superpixels extracted via energy-driven sampling," in *European conference on computer vision*, Springer, 2012, pp. 13–26.

[90] H. E. Tasli, C. Cigla, T. Gevers, and A. A. Alatan, "Super pixel extraction via convexity induced boundary adaptation," in *2013 IEEE International Conference on Multimedia and Expo (ICME)*, IEEE, 2013, pp. 1–6.

[91] J. Yao, M. Boben, S. Fidler, and R. Urtasun, "Real-time coarse-to-fine topologically preserving segmentation," in *Proceedings of the IEEE conference on computer vision and pattern recognition*, 2015, pp. 2947–2955.

[92] J. Strassburg, R. Grzeszick, L. Rothacker, and G. A. Fink, "On the influence of superpixel methods for image parsing.," in *VISAPP (2)*, 2015, pp. 518–527.

[93] J. Long, E. Shelhamer, and T. Darrell, "Fully convolutional networks for semantic segmentation," in *Proceedings of the IEEE conference on computer vision and pattern recognition*, 2015, pp. 3431–3440.

[94] N. Otsu, "A threshold selection method from gray-level histograms," *IEEE transactions on systems, man, and cybernetics*, vol. 9, no. 1, pp. 62–66, 1979.

[95] D. Liu and J. Yu, "Otsu method and k-means," in *2009 Ninth International Conference on Hybrid Intelligent Systems*, IEEE, vol. 1, 2009, pp. 344–349.

[96] D.-Y. Huang and C.-H. Wang, "Optimal multi-level thresholding using a two-stage otsu optimization approach," *Pattern Recognition Letters*, vol. 30, no. 3, pp. 275–284, 2009.

[97] D. Stutz, A. Hermans, and B. Leibe, "Superpixels: An evaluation of the state-of-the-art," *Computer Vision and Image Understanding*, vol. 166, pp. 1–27, 2018.

[98] T. Chidley and I. Goodwill, "A compact watershed model system," *Journal of Hydrology*, vol. 24, no. 1-2, pp. 155–169, 1975.

[99] G. Seif, "The 5 clustering algorithms data scientists need to know," *Last accessed*, vol. 30, 2019.

[100] F. Sultana, A. Sufian, and P. Dutta, "Evolution of image segmentation using deep convolutional neural network: A survey," *Knowledge-Based Systems*, vol. 201, p. 106 062, 2020.